Title

Giant birefringence silicon nanophotonic multi-slot waveguides for optical delay line applications

Author

Yang, Shun-Hui

Publication Date

2008

Peer reviewed|Thesis/dissertation

UNIVERSITY OF CALIFORNIA, SAN DIEGO

Giant birefringence silicon nanophotonic multi-slot waveguides for optical delay line applications

A dissertation submitted in partial satisfaction of the requirements for the degree of

Doctor of Philosophy

in

Engineering Science (Mechanical Engineering)

by

Shun-Hui Yang

Committee in Charge:

Professor Prabhakar R. Bandaru, Chair
Professor Shayan Mookherjea, Co-Chair
Professor Sungho Jin
Professor Yu-Hwa Lo
Professor Vlado Lubarda

2008

The Dissertation of Shun-Hui Yang is approved, and it is acceptable in quality and form for publication on microfilm:

____

____

____

____

Co-Chair

____

Chair

University of California, San Diego

2008

To my family

Table of contents

List of Figures

List of tables

Acknowledgement

I wish to acknowledge and deeply thank my advisors, Professor Prabhakar R. Bandaru and Professor Shayan Mookherjea for their supervision, advices, and guidance for my research and providing me unflinching encouragement and support in various ways. Their truly scientist intuitions have made them as a constant oasis of ideas and passions in science, which exceptionally inspire and enrich my growth as a student. I wish to express my gratitude toward my committee members Professor Sungho Jin, Professor Vlado Lubarda and Professor Yu-Hwa Lo for their time and precious advices to my research.

I gratefully thank the following individuals: Dr. Leon Chen, Dr. I-Chen Chen, Chi-Nung Ni, Max Aubain, Jung S. Park, Michael L. Cooper, Kazuhiro Ikeda and Matthew Zhang for their advices and willingness to share their bright thoughts with me, which was very fruitful for shaping up my ideas and research.

I would like to acknowledge all Nano3 staff, Professor Shaya Fainman and his research group, and all MAE staff for their assistance in various aspects to help me finish my thesis.

My deepest appreciation goes to my parents, Jheng-Ling Yang and Jing-Yi Wu, my brother, His-Chieh Yang, and my whole family. Without their endless love and supports, this work would never be done.

Finally, I would like to thank everybody who was important to the successful realization of thesis, as well as expressing my apology that I could not mention personally one by one.

Chapter 2 and chapter 4, in part, have been published as "Giant birefringence in multi-slotted silicon nanophotonic waveguides" by S. H. Yang, M. L. Cooper, P. R. Bandaru and S. Mookherjea, Optics Express, Vol. 16, 8306 (2008). Appendix B, in full, has been published as “An experimental study of the reactive ion etching (RIE) of GaP using BCl3 plasma processing” by S. H. Yang, P. R. Bandaru, Materials Science and Engineering B, Vol. 143, 27 (2007)

Shun-Hui Yang

La Jolla, October 2008

Vita

1980	Born in Taipei, Taiwan

Education

2002	Bachelor of Science in Engineering
	National Taiwan University, Taipei, Taiwan
2004	Master of Science in Engineering
	University of California, San Diego, La Jolla
2008	Doctor of Philosophy, Mechanical Engineering
	University of California, San Diego, La Jolla

Journal Publications

S. H. Yang, M. L. Cooper, P. R. Bandaru and S. Mookherjea, "Giant birefringence in multi-slotted silicon nanophotonic waveguides", Optics Express, Vol. 16, 8306-8316 (2008).

S. Mookherjea, J. S. Park, **S. H. Yang** and P. R. Bandaru, "Localization in silicon nanophotonic slow-light waveguides", Nature Photonics, Vol. 2, No. 2, pp. 90-93 (2008)

S. H. Yang, P. R. Bandaru, "Effect of surface texture and geometry on spoof surface plasmon dispersion", Optical Engineering, Vol. 47, 029001-4 (2008)

S. H. Yang, P. R. Bandaru, "An experimental study of the reactive ion etching (RIE) of GaP using BCl_3 plasma processing", Materials Science and Engineering B, Vol. 143, 27-30 (2007)

Conference Papers

Shun-Hui Yang, Prabhakar R. Bandaru, Michael L. Cooper, Jung S. Park, and Shayan Mookherjea, “Multi-Slot Silicon Optical Waveguides”, Conference on Lasers and Electro-Optics (CLEO), San Jose (2008)

Jung S. Park, **Shun-Hui Yang**, Prabhakar R. Bandaru and Shayan Mookherjea, “Light localization in silicon nanophotonic waveguides”, Conference on Lasers and Electro-Optics (CLEO), San Jose (2008)

Shun-Hui Yang, and Prabhakar R. Bandaru, “The Effect of Surface Texture and Geometry on Spoof Surface Plasmon Dispersion”, MRS Spring Meeting, San Francisco (2008)

Prabhakar R. Bandaru, **Shun-Hui Yang**, Jung S. Park and Shayan Mookherjea, “Nanostructured Silicon Optical Waveguides”, Conference on American Physical Society (APS), New Orleans (2008)

Shayan Mookherjea, Michael L. Cooper, Jung S. Park, **Shun-Hui Yang** and Prabhakar R. Bandaru, "Design, fabrication, and measurement of giant birefringence at telecommunications avelengths in multi-slotted silicon nanophotonic optical waveguides", **XXIX URSI General Assembly**, Chicago (2008).

ABSTRACT OF THE DISSERTATION

Giant birefringent silicon nanophotonic multi-slot waveguides for optical delay line applications

by

Shun-Hui Yang

Doctor of Philosophy in Engineering Science (Mechanical Engineering)

University of California, San Diego, 2008

Professor Prabhakar R. Bandaru, Chair

Professor Shayan Mookherjea, Co-Chair

With the vast increase in the amount of data transfer around the world each day, there has been a necessity for rapid development in optical communication and signal processing technologies. Using an all optical scheme to replace the current electronic format shows promise in the next generation of signal processing. In an optical processing system, the optical delay line buffer is a critical component. While significant research has been done on novel delay line schemes, it will be necessary to develop a CMOS compatible technology capable of integration onto a micro-chip.

In this thesis, a multi-slotted waveguide has been studied as a novel element for

optical delay line applications. Detailed simulations show large birefringence between the polarization modes in a multi-slot waveguide which enables the creation of a time delay. The birefringence was optimized by the use of fabricated structures with high refractive index contrast to create a compact single-mode waveguide, through the etching of deep sub-wavelength channels within the waveguide. The channels (comprising Si ribs and air gaps) are strongly coupled in the near field.

The multi-slot waveguides were successfully fabricated and giant birefringence property was demonstrated. The obtained value of Δn_g was ~1.6 at 1.55μm. When used as a polarization-selective delay line element, the delay-bandwidth product was computed to be 40/*mm* which is comparable to existing delay line schemes. A mode shaping tool was also designed to shape the near field mode and achieve almost identical coupling to external optics. This reduces the polarization dependent loss. This work shows the potential of multi-slot waveguides for future optical communication applications.

Chapter 1: Introduction

Since the 1990s, there has been a necessity for rapid development in optical communication technology for high volume information processing and transfer. The use of optics for information communication is believed to significantly enhance the performance of future computing systems[1]. Due to the intrinsically faster velocities and non-interfering nature of photons, advances in optical amplifiers and passive optical components such as add-drop filters could enable the elimination many of photon-electron conversion steps, which limit system performance. However, critical steps such as switching and routing are still handled electronically. In order to avoid the bottleneck of slow optical-electronic-optical (OEO) conversion, any all-optical processing system then must include optical delay lines[2] (optical buffers). Optical delay provides a critical component in all-optical computing and is considered a key technology for the next generation of network communications.

1.1. Optical Delay line

The purpose of an optical delay line is the temporary storage of data, in optical format, when the processor is in use to avoid information congestion[3]. Figure 1-1 shows a schematic layout of a delay line system. Incoming optical signals enter the delay line from the left and then are released after a pre-determined time at the right. The signal delay is managed by a control input.

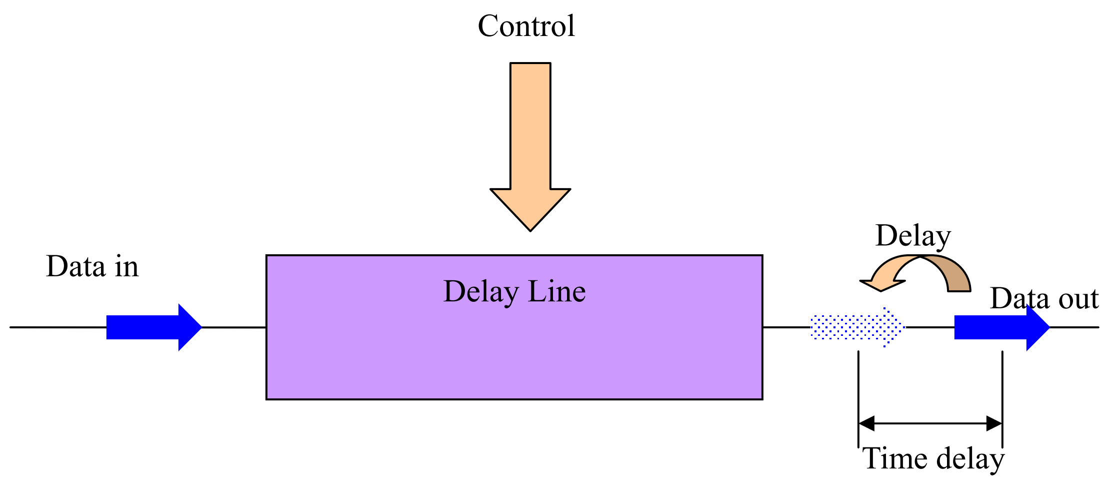

Figure 1-1. Schematic of an optical delay line, indicating the functionality and implementation.

“Slow light” with a greatly reduced signal group velocity is currently being intensively studied for optical delay lines[2]. The group velocity and group refractive index of the signal is given by

$$v_g = \frac{c}{n_g} = \frac{d\omega}{dk} \qquad (1\text{-}1)$$

$$n_g = c\frac{dk}{d\omega} = \frac{d(n_{eff}\omega)}{d\omega} = n_{eff} + \omega\frac{dn_{eff}}{d\omega} = n_{eff} + f\frac{dn_{eff}}{df} \qquad (1\text{-}2)$$

where c is the velocity of light in vacuum, n_g is the group index, n_{eff} is the effective refractive index of a material or of a guided mode in waveguide, k is the wave number, ω is the angular frequency and f is frequency. From equation (1-2), it is observed that the group velocity depends not only on the n_{eff}, but also on the frequency dispersion (dn_{eff}/df). In general, slow light can be achieved through a large dispersion, most commonly through material dispersion or structure resonant photonic systems[4-15].

1.2. Delay-bandwidth product

Delay lines need to utilize a wide bandwidth to be useful[2]. In this context, the Delay Bandwidth Product (DBP) is a critical parameter which indicates buffering performance[2, 16]. The DBP is given by[17]

$$DBP = \Delta t \Delta f = \frac{\Delta n_g L}{c} \Delta f \qquad (1\text{-}3)$$

where Δt is the light delay time over a propagation length L, Δn_g is the change of group index and Δf is the frequency bandwidth. DBP is therefore the channel's end-to-end delay multiplied by the data channel capacity, and is equivalent to the amount of data "stored" at any given time in the buffer. Therefore, it is a good metric to compare various optical delay line schemes.

In order to increase the DBP, for a given length L, one can increase the time delay by either increasing Δn_g or the bandwidth (Δf), as they are mutually exclusive. By taking n_g to be much larger than n_{eff}, in equation (1-2), n_g can be approximated by:

$$n_g \cong f \frac{\Delta n_{eff}}{\Delta f}. \qquad (1\text{-}4)$$

If Δn_{eff} is a fixed value, the bandwidth (Δf) must be very narrow for a large value of n_g, for reduced group velocity, and larger delay which is consequently achieved at the expense of decreased bandwidth[17]. Figure 1-2 illustrates the variation of the effective refractive index versus the frequency. Steep dispersion ($dn_{eff}/df >> 0$), which occurs at the resonant frequency can be used for obtaining a large group index.

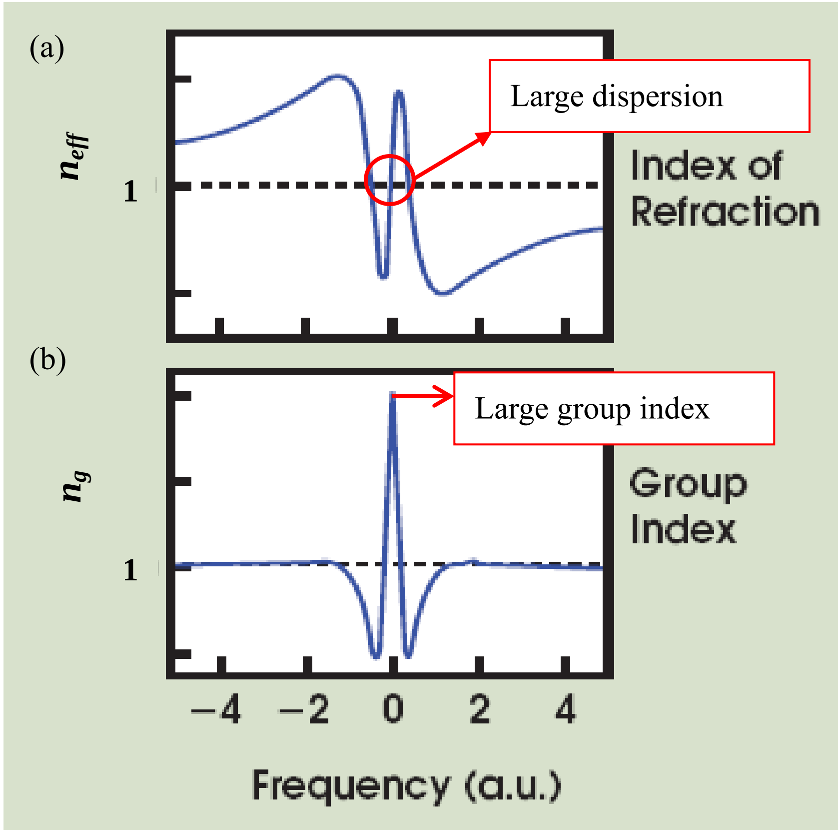

Figure 1-2. (a) The effective refractive index versus frequency near resonance, where a large dispersion (dn_{eff}/df) can be obtained. (b) Large group index is observed due to large dispersion. (Figure courtesy: Gauthier *et al*. Photonics Spectra, Vol. 42, p.44, 2006)

Delay lines using different schemes have been demonstrated, e.g. based on fiber optics [18-20], semiconductor optical amplifiers (SOA)[21-24], resonant photonic systems[13, 25-29] and atomic vapors[30, 31]. Figure 1-3[32] provides a summary of current schemes. The DBP is less than 10 for most cases and the largest values have been achieved using fiber optics with fiber lengths ranging from hundreds to thousands of meters[18-20]. However, such schemes are unsuitable for on-chip integration. Generally, a DBP (with L=1m) greater than 64,000 has been suggested to demonstrate the possibility of constructing a functional optical buffer[17]. Consequently, current optical delay line research is still at an early age and a significant improvement on DBP is necessary.

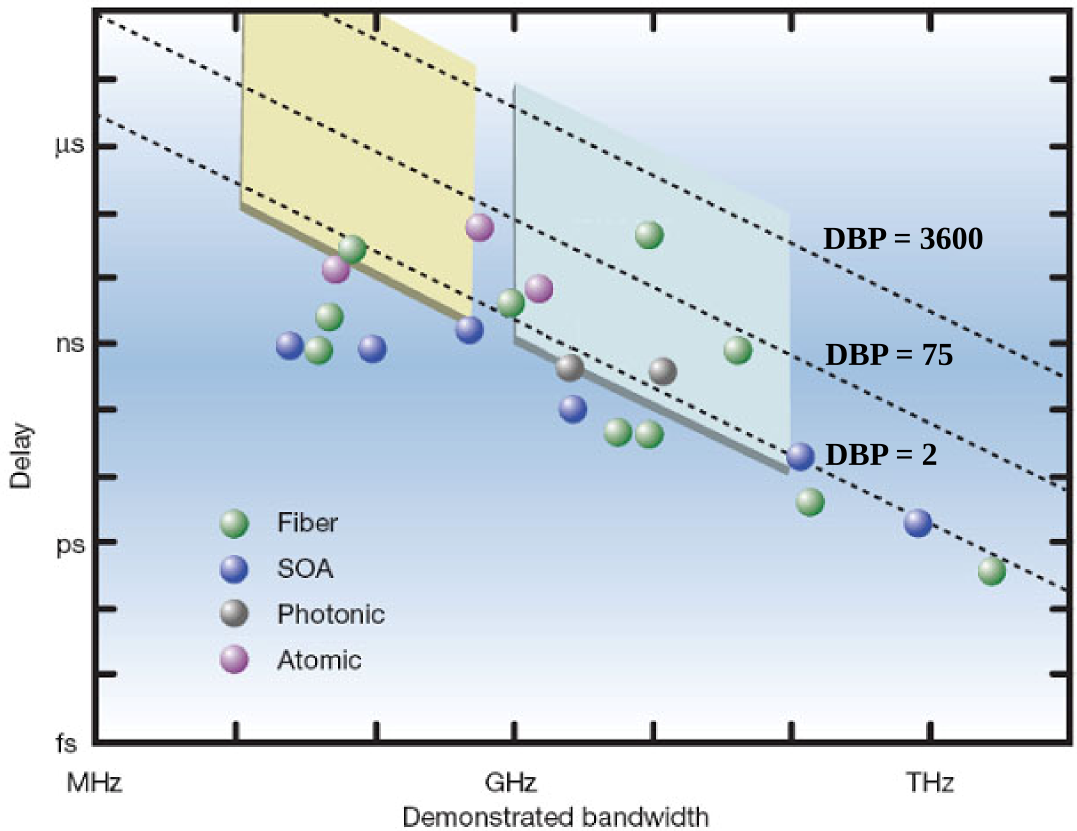

Figure 1-3. Comparison of various proposed schemes for optical delay line application. Achieved delay time versus bandwidth is presented. (Figure courtesy: Parra *et al*, Optics and Photonics News, 18, 40, 2007)

In this thesis, an approach to fabricate and optimize an optical delay line which utilizes the birefringence property of silicon waveguides is proposed, where the group indices are polarization sensitive. Hence, the Δn_g depends on the polarization of the propagating electromagnetic (EM) waves. It will also be shown that it is possible using silicon based fabrication technology to develop integrated devices, incorporating optical delay elements.

1.3. Birefringent waveguide delay lines

A waveguide is said to be birefringent if different polarizations of the light travel in it with different group velocities (or different group indices). Two orthogonal polarizations are defined: (1) Transverse Magnetic (TM) mode where electric field is linearly polarized perpendicular to the substrate, and (2) Transverse Electric (TE) mode where the electrical field is linearly polarized parallel to the substrate, as shown in Figure 1-4.

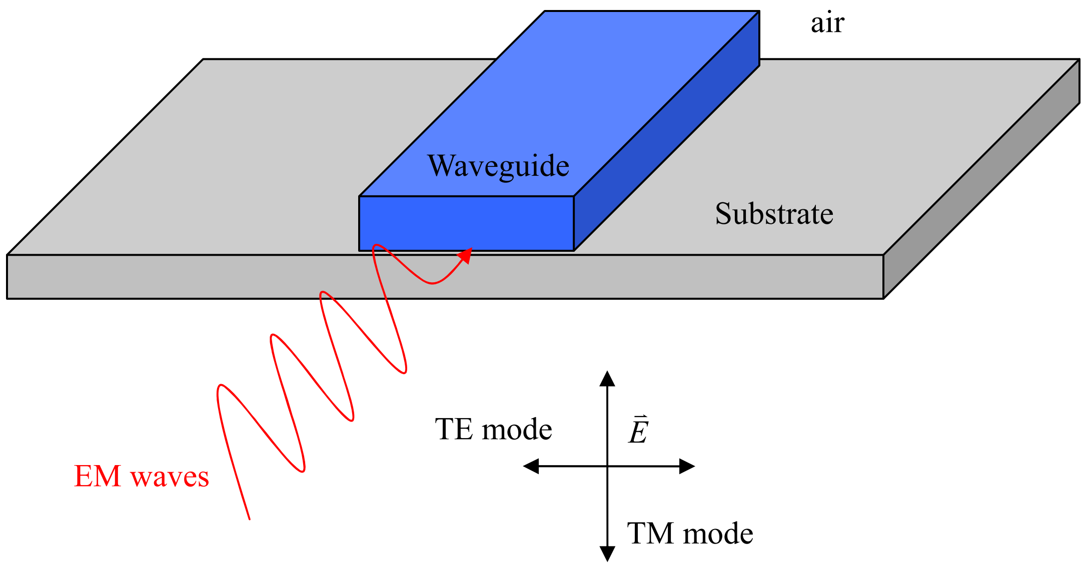

Figure 1-4. Orientation of coordinate axes of EM mode with respect to the substrate. When the electric field is parallel to the substrate, a TE mode is defined while if the electrical field is perpendicular to the substrate, a TM mode is defined.

Then the time delay between the TE and TM mode is:

$$\Delta t = \frac{L}{v_g^{TM}} - \frac{L}{v_g^{TE}} = \frac{Ln_g^{TM}}{c} - \frac{Ln_g^{TE}}{c} = \frac{L}{c}(n_g^{TM} - n_g^{TE}) = \frac{L}{c}\Delta n_g \,. \quad (1\text{-}5)$$

From equation (1-5), it is shown that larger birefringence (Δn_g) in the waveguide induces greater time delay. Therefore, optimizing/maximizing waveguide birefringence is necessary for improving delay line performance.

1.3.1. Birefringence in single slot-waveguides

In photonic strip waveguides (see Figure 1-5), a birefringence of about Δn_g~0.3 (an order of magnitude greater than normal single mode ridge waveguide[33]) was demonstrated by Dulkeith *et al* [34]. Larger birefringence (Δn_g=0.7) was found recently in single-slot waveguide[35, 36] made by Xu *et al*[35]. A single slot waveguide is a strip waveguide with a sub-micron slot (see Figure 1-5) filled with a low refractive index material, such as air.

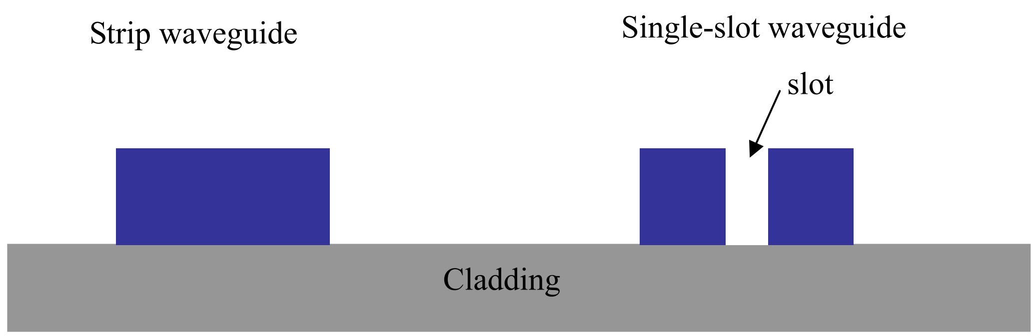

Figure 1-5. Comparison between strip waveguide and single-slot waveguide.

In the single-slot waveguide, a large birefringence is caused by the difference in the propagating characteristics of the TE and TM modes. For the TE mode, the electric field is enhanced in the air slot and confined due to the requirement of continuity of the normal component of the electrical displacement (*D*) across the silicon-air boundary, as illustrated by the following equation,

$$D_s = n_s^2 E_s = D_H = n_H^2 E_H \tag{1-6}$$

where D_s/D_H is electrical displacement in slot/high index region, n_s/n_H is effective refractive index of slot/high refractive index and E is the electrical field. Hence, assuming n_H=3.48 (silicon) and n_s=1 (air), the electrical field in the air will be enhanced by (n_H^2 / n_s^2) ~12.1.

As a result of the enhancement of the electrical field in the air slot, the optical power is much higher in the slot then in the high index silicon. On the contrary, for the TM mode, most of the electric field is concentrated in the high index silicon region. The difference in the electric field concentration and consequent difference in refractive indices creates large birefringence. Figure 1-6(a) illustrates the electrical field profile of the TE mode in a single-slot waveguide. The bright region at the center illustrates a strong electric field in the slot. Additionally, the direction of the electric field lines indicates that the electrical field is mostly normal to the interface between silicon (high refractive index region) and slot (low refractive index region), giving rise to a large refractive index discontinuity. This confirms that the requirement of continuity of the D enhances the electrical field concentration in the slot. Figure 1-6(b) shows the three dimensional electric field amplitude profiles.

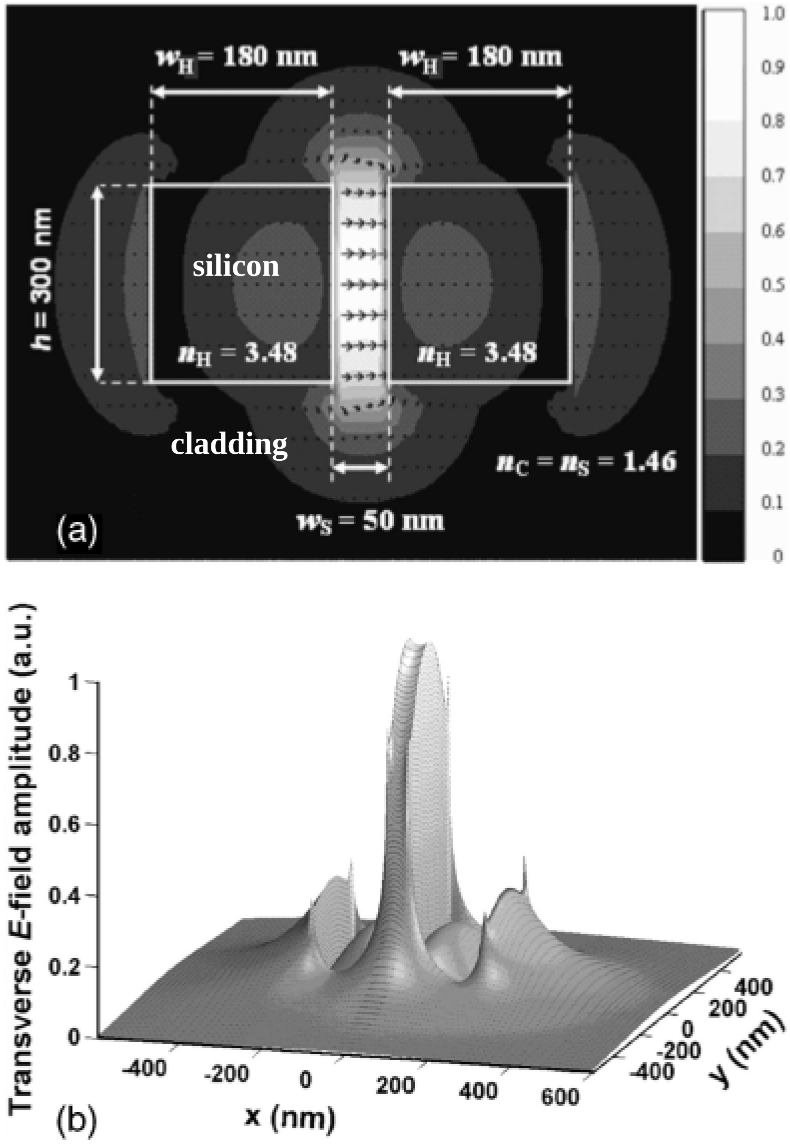

Figure 1-6. (a) Contour of the electrical field amplitude for TE mode. Due to the continuity condition of the electric displacement, most of the electrical field is concentrated in the low index region. n_H is effective refractive index of high index region (silicon); n_s and n_c are effective refractive indices of substrate and cladding. w_H is the width of the high index region. (b) Three dimensional plot of the electrical field amplitude. (Figure courtesy: Almeida *et al*, Optics Letters, Vol. 29, p1209, 2004, Fig. 3)

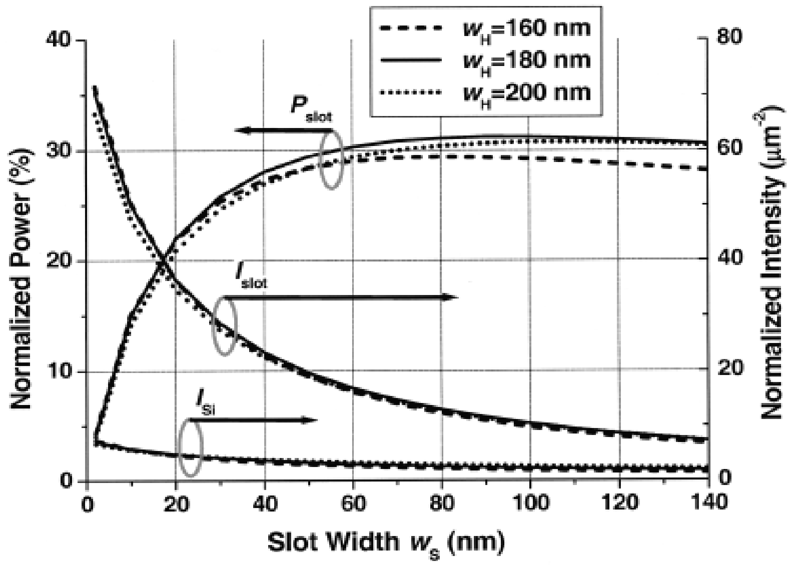

Figure 1-7. Normalized optical power (P_{slot}) and average intensity in the slot of the single-slot waveguide for the TE mode. w_H is the silicon width in Figure 1-6. P_{slot} indicates the power percentage in the slot. I_{slot} is the average intensity inside the slot and I_{Si} is the average intensity in the silicon. (Figure courtesy: Almeida *et al*, Optics Letters, 29, p1209, Fig. 4)

Figure 1-7 shows the normalized optical power (P_{slot}) and average intensity (I_{slot}) inside the slot as a function of slot width (w_s). It is seen that w_H does not affect the power concentration in the slot significantly. On the other hand, with increasing the slot width, the power in the low index region increases and saturates at slot width of ~60*nm*. In order to further enhance the power concentration in the low index region, a horizontal multi-layer structure was proposed[37, 38] as illustrated in Figure 1-8(a). Three horizontal, low refractive index nano-layers were sandwiched by high refractive index silicon. In this case, silicon dioxide (n_{eff}=1.46) was used as low-index layer, to simulate a practical device. The electrical field of TE mode was shown to be enhanced in the structure. Figure 1-8(b) illustrates the percentage of total power confined in the low index regions. Different numbers of layers are compared and it is observed that waveguides with multiple low index layers further increase the power confinement in the low index region. The number of optimal slots for horizontal multilayer was suggested to be between 3 and 5 by Feng *et al*[37].

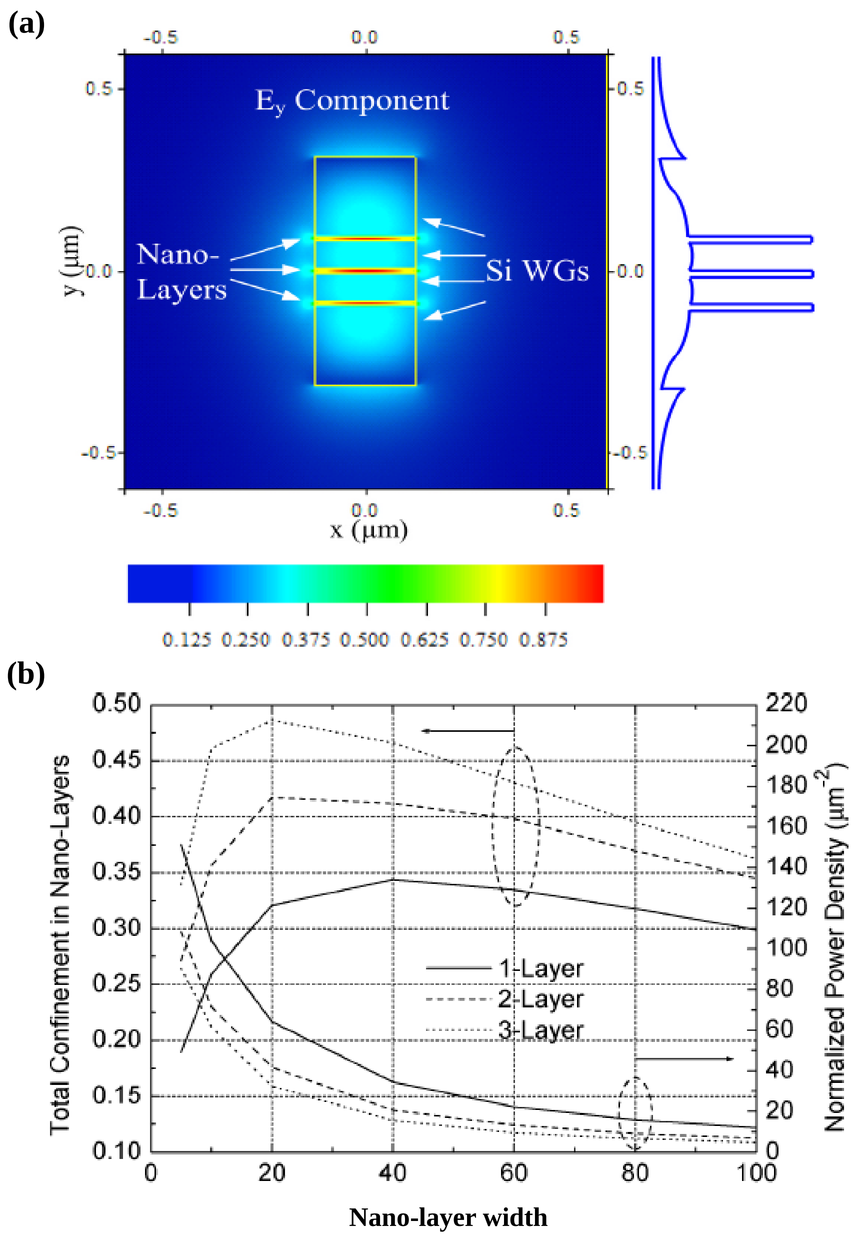

Figure 1-8. (a) TM mode in a 3-horizontal low index layers structure. (b) Comparison of percentage of power confined in the low index region using different numbers of low index layers. Normalized power intensity is also compared. (Figure courtesy: Feng *et al*, Journal of Quantum Electronics, Vol. 42, p885, 2006, Fig. 2 and 6)

Although multilayer structures show enhanced power concentration in the low index region, the birefringence properties were not shown to be optimal. Hence, a waveguide with multiple vertical slot structures was proposed in this work to maximize waveguide birefringence. Using vertical slots, a larger enhancement can be obtained, using air in the low index slot (instead of silicon dioxide as in the horizontal case).

1.4. Scope and outline of the thesis

In this thesis, vertical multi-slot waveguides are proposed for novel polarization sensitive devices to be used in optical delay line applications. The birefringence for obtaining large optical delay was optimized by the use of materials with high refractive index contrast to create a compact single-mode waveguide, through the etching of deep sub-wavelength channels within the waveguide. The length scales were determined through Effective Medium Theory (EMT) and numerical simulations.

Chapter 2 discusses the design and mathematical modeling of multi-slot waveguides. Length scales of the waveguides were chosen thorough detailed simulations using a mode-solving software package that utilizes the vectorial Finite-Difference-Frequency-Domain (FDFD) algorithms. Comparison between FDFD results and supermode theory is presented.

Chapter 3 illustrates the waveguide fabrication process. Through detailed semiconductor processing, the fabrication was optimized for the multi-slot waveguide configuration.

Chapter 4 demonstrates giant birefringence (approximately $\Delta n_g \sim 1.6$) of multi-slot waveguides through Free Spectral Range (FSR) measurements using Fabry-Perot resonator schemes. The birefringence (Δn_g~1.6) is nearly **twice** as large as was previously achieved. Based on this birefringence value, a DBP was calculated and compared to existing delay line schemes. A mode shaping tool was designed to shape the near field mode and achieve almost identical coupling to external optics, greatly reducing polarization dependent loss. The propagation loss in multi-slot waveguides for different polarizations was also investigated.

Chapter 5 summarizes this dissertation and discusses future work.

Appendix 1 explores work in silicon absorption through Fabry-Perot transmission characteristics. The absorption coefficient of silicon as a function of temperature and doping level were investigated.

Appendix 2 gives a detailed study on etching processes, using BCl_3 gas, with a focus on GaP.

Chapter 2: Multi-slot waveguide design: Principles and Simulations

A vertical multi-slot waveguide was proposed for large birefringence. An enhanced power concentration in the low index region is shown to be responsible for the birefringence. In this chapter, optimal waveguide design was done using Effective Medium Theory (EMT) and MATLAB simulations. These results will be discussed and compared with supermode theory. Finally, a comparison of multi-slot waveguide with single-slot waveguide will be presented.

2.1. Birefringence multi-slot waveguide: design and optimization

In order to obtain maximized birefringence in silicon based waveguide systems, a multi-slot waveguide was proposed. Such a waveguide consists of alternate vertical layers of low index (air) and high index (silicon) material with cross-sectional features smaller than the operative wavelength of light (see Figure 2-1). The obtained birefringence due to such a periodic (period = P) layered structure could also be termed "form-birefringence"[39-44]. The slot width (d), occupied by low-index (air) region, is defined in terms of the period, through the filling fraction q ($=d/P$).

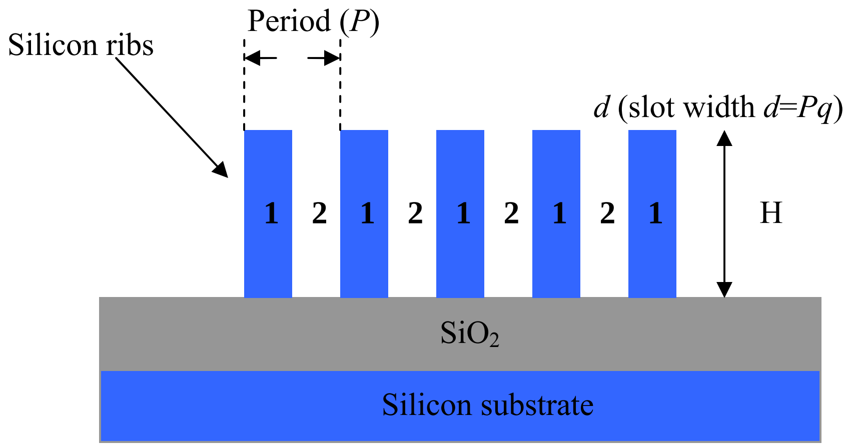

Figure 2-1. Schematic of vertical multi-slot waveguide on SiO_2 cladding. Each silicon rib is separated by an air slot. Slot width and period of the waveguide were chosen through simulations as detailed later in this chapter.

2.1.1. Effective-Medium-Theory

Effective Medium Theory (EMT)[42-51] was used to analyze periodic multi-layered media with sub-micron grating-like features (as shown in Figure 2-1). When the grating period (P) is much less than the wavelength of the incident radiation ($P<<\lambda$ or $P/\lambda \rightarrow 0$), the EM wave can be insensitive to the structural details of the material. The composite, structured material then acts as an effective medium composed of two materials.

According to EMT, the refractive index of the effective medium for the TM mode and TE mode can be represented through the following equations[48]

$$n_{eff}^{TM} = \left\{ \left[(1-q)n_1^2 + qn_2^2 \right] + \frac{1}{3}\left[\frac{d}{\lambda}\pi(1-q)q \right]^2 \left(n_2^2 - n_1^2\right)^2 \right\}^{1/2} \tag{2-1}$$

$$n_{eff}^{TE} = \left\{ \left[\frac{1}{n_1^2}(1-q) + \frac{1}{n_2^2}q \right]^{-1} + \frac{1}{3}\left[\frac{d}{\lambda}\pi(1-q)q \right]^2 \left(\frac{1}{n_2^2} - \frac{1}{n_1^2} \right)^2 \left[\frac{1}{n_1^2}(1-q) + \frac{1}{n_2^2}q \right]^{-3} \left[(1-q)n_1^2 + qn_2^2 \right] \right\}^{1/2} \tag{2-2}$$

where n_1 and n_2 are effective refractive indices of ribs and slots respectively. When $P/\lambda < 0.2$, the higher order (>2) terms can be neglected and equation (2-1) and (2-2) can be reduced to[42]

$$n_{eff}^{TM} = \left[(1-q)n_1^2 + qn_2^2\right]^{1/2} \tag{2-3}$$

$$n_{eff}^{TE} = \left[\frac{1}{n_1^2}(1-q) + \frac{1}{n_2^2}q\right]^{-1/2} \tag{2-4}$$

Consequently, the effective refractive index difference between the TM and TE modes is

$$\Delta n_{eff} = n_{eff}^{TM} - n_{eff}^{TE} = \frac{\left[n_1^2(1-q)+n_2^2q\right]^{1/2}\left[n_2^2(1-q)+n_1^2q\right]^{1/2} - n_1n_2}{\left[qn_1^2 + (1-q)n_2^2\right]^{1/2}}\,. \tag{2-5}$$

It can be seen that this effective index difference is now wavelength independent. Figure 2-2 plots the effective refractive index difference (Δn_{eff}) versus filling fraction q, as a function of n_2. n_1 is chosen to be 3.48 (silicon) while n_2 varies. From the figure, it is observed that Δn_{eff} increase with increasing refractive index differences between the alternating layers. However, where the maximum Δn_{eff} occurs is dependent on n_2. For example, when n_2 increases from 1 to 2.5, the maximum of q shifts from q = 0.33 to q = 0.46.

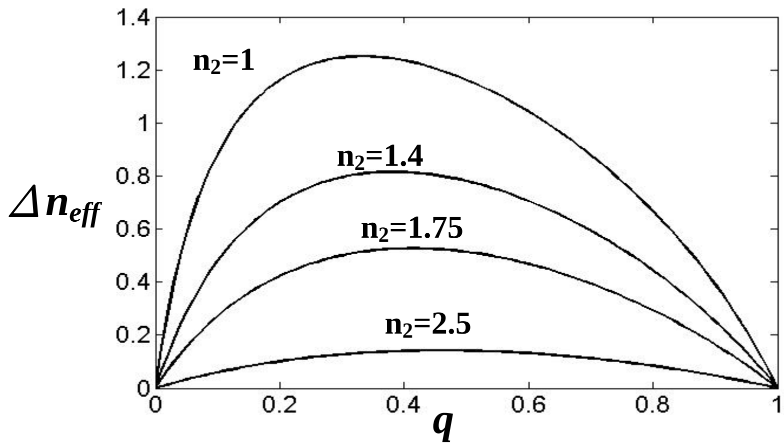

Figure 2-2. Δn_{eff} versus q with n_1=3.48 and n_2 = 1, 1.4, 1.75 and 2.5. The maximum Δn_{eff} occurs at q=0.33, 0.38, 0.41 and 0.46 respectively. The larger the index difference between the two materials, the larger the Δn_{eff} .

In order to achieve the largest birefringence, Δn_{eff} has to be maximized. With silicon as the high index layer (n_1=3.48), air (n_2=1) is seen to be an ideal candidate for the low index layer, yielding Δn_{eff} of ~1.25 at q =0.33. Figure 2-3 plots the effective index of the TE and TM modes individually. It is important to note that both n_{TE} and n_{TM} decrease when q increases. This occurs because the low index (air) volume fraction increases with slot width. Additionally, due to the requirement of continuity of the normal electrical displacement at the silicon-air interface, the power in the air is enhanced for TE mode, and will, therefore, be more affected than TM mode. Consequently, lower effective refractive index than TM mode is observed. Beyond q=0.43, the refractive index of TE mode becomes lower than the refractive index of the cladding (silicon dioxide). Consequently, the TE mode would not be supported in waveguide propagation through total internal reflection. The fabricated waveguide must have a q smaller than 0.43.

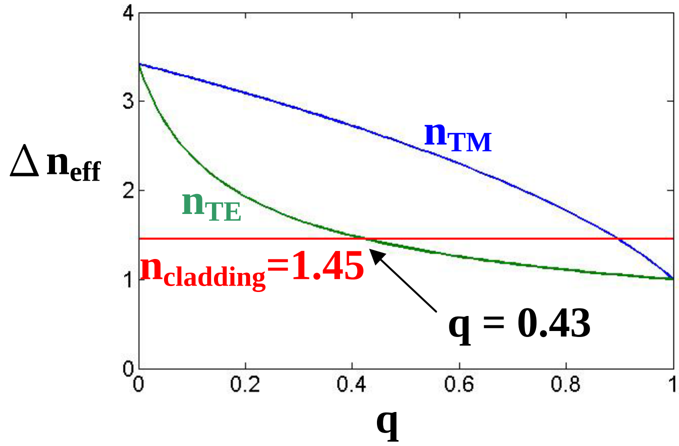

Figure 2-3. The effective index of the TE mode (green curve) and the TM mode (blue curve). When q is greater than 0.43, TE mode has an effective refractive index lower than the cladding. Hence, the TE mode will not be supported.

Due to the possible limitations in e-beam lithography, the minimum device feature size was set to be ~80nm. The birefringence is optimized with q=0.33 and P=250nm. Therefore the period will be 80/0.33~250nm and, at $\lambda = 1550nm$,

$$\frac{P}{\lambda} = \frac{250nm}{1550nm} = 0.16 < 0.2\,.$$

Consequently, EMT would still be valid with the 250nm period, and the approximations used for equation (2-5) are still valid. Using equation (1-2), an expression for Δn_g is obtained:

$$\Delta n_g = n_g^{TM} - n_g^{TE} = \left(n_{eff}^{TM} - n_{eff}^{TE}\right) + \left(\omega\frac{dn_{eff}^{TM}}{d\omega} - \omega\frac{dn_{eff}^{TE}}{d\omega}\right) = \Delta n_{eff} + \omega\frac{d\Delta n_{eff}}{d\omega} = \Delta n_{eff} - \lambda\frac{d\Delta n_{eff}}{d\lambda} \qquad (2\text{-}6)$$

In equation (2-5), it was seen that Δn_{eff} is independent of wavelength and, hence $d\Delta n_{eff}/d\lambda=0$, $\Delta n_g = \Delta n_{eff}$. Hence, Δn_g can be maximized through optimization of Δn_{eff}.

2.1.2. Numerical simulations

Using the EMT, an optimum value of the filling fraction was chosen to maximize the waveguide birefringence. However, the effective medium model is only applicable to plane waves incident on an *infinitely-wide* periodically stratified grating. On-chip silicon-on-insulator (SOI) photonics require waveguides with finite cross-sectional length scales. Hence, using methods relevant to finite gratings can help accurately determine q.

A mode solving software package using the vectorial Finite-Difference-Frequency-Domain (FDFD) algorithm was used to solve Maxwell's equations and determine the optimum width and number of slots. First, the optimized period was chosen to be 250 nm. The number of optimal slots for horizontal multilayer was suggested to be between 3 and 5 by Feng *et al*[37].

The effective refractive index (n_{eff}) for the TE and TM modes versus the number of silicon ribs (N) was simulated. It is seen in Figure 2-4 that the indices seem to saturate at $N > 8$. The effective refractive index of the TM mode is always greater than the TE mode for all N as the energy of the TM mode is predominantly concentrated in the silicon ribs and the TE mode is mainly in the air. In Figure 2-5, it is seen that the Δn_{eff} saturates at N=5. Consequently, the total width of the waveguide was chosen to be 1.15μm to allow for the juxtaposition of 5 high-index and 4 low-index regions.

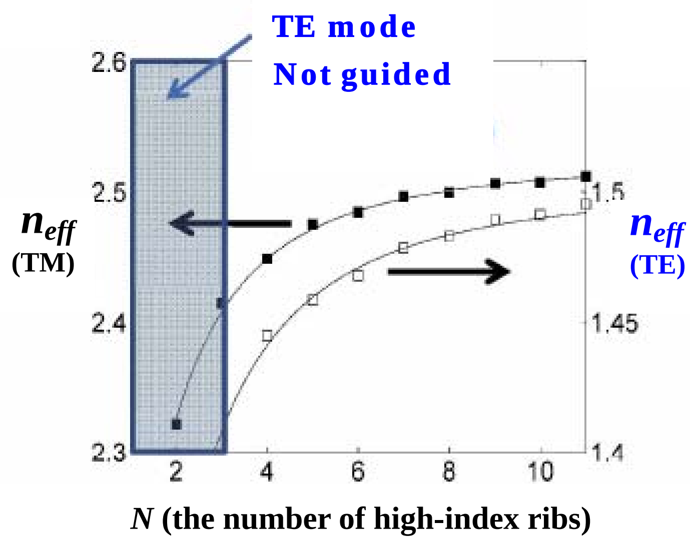

Figure 2-4. Effective refractive index versus number of silicon ribs. The index tends to saturate with large *N* for both TE and TM modes. (Figure Courtesy: S.-H. Yang *et al*, Optics Express, Vol. 16, p.8306, 2008)

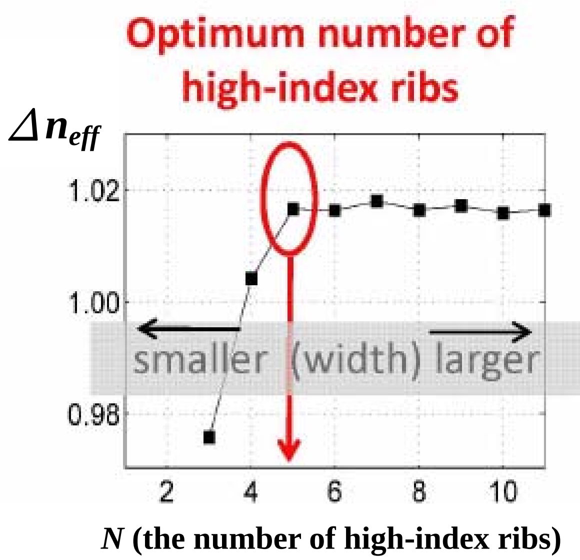

Figure 2-5. The effective refractive index difference between the two modes versus the number of high-index ribs (silicon). The maximum index difference is achieved when there are 5 ribs or more. (Figure Courtesy: S.-H. Yang *et al*, Optics Express, Vol. 16, p.8306, 2008)

The effective refractive index difference between the TE and TM modes versus q with fixed period (P) was also simulated, and the results are shown in Figure 2-6. The largest birefringence corresponds to q=0.38. The shape of this curve is similar to that of the plane-wave case estimated by EMT[42] in Figure 2-2. Also, the maximum value of q that supports the TE mode was predicted by FDFD to be 0.43, which is similar to the predictions using EMT theory as in Figure 2-3. Figure 2-7 illustrates the final optimized optimal design of the multi-slot waveguide, used in this thesis.

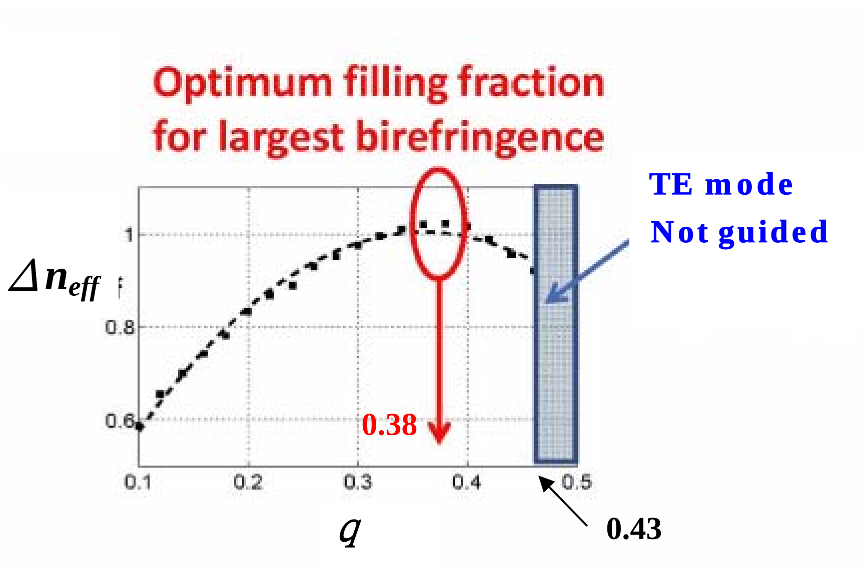

Figure 2-6. Refractive effective index difference between the TE and the TM mode. Optimum q was determined to be 0.38 for maximum birefringence. When q is beyond 0.43, the effective index of TE mode will be lower than the oxide index and the mode will not be supported. (Figure Courtesy: S.-H. Yang *et al*, Optics Express, Vol. 16, p.8306, 2008)

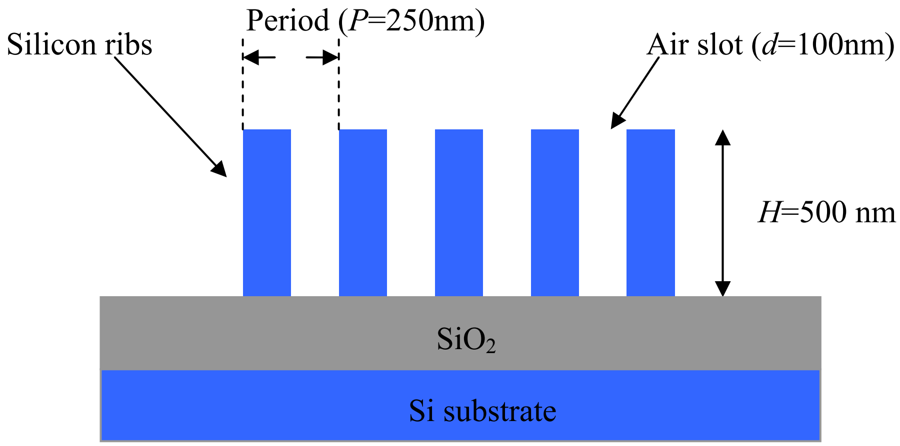

Figure 2-7. Length scales in the multi-slot waveguide.

Figures 2-8 and 2-9 show the intensity and amplitude of fundamental TE_0 and TM_0 modes. It is seen that for the TE_0 mode, the electrical field is localized in the low index region (air), while for the TM_0 mode, the field is localized in high index region (silicon). For the TE_0 mode, the electrical field immediately inside the slot is ~12 times greater than that immediately inside the silicon ribs.

(a)

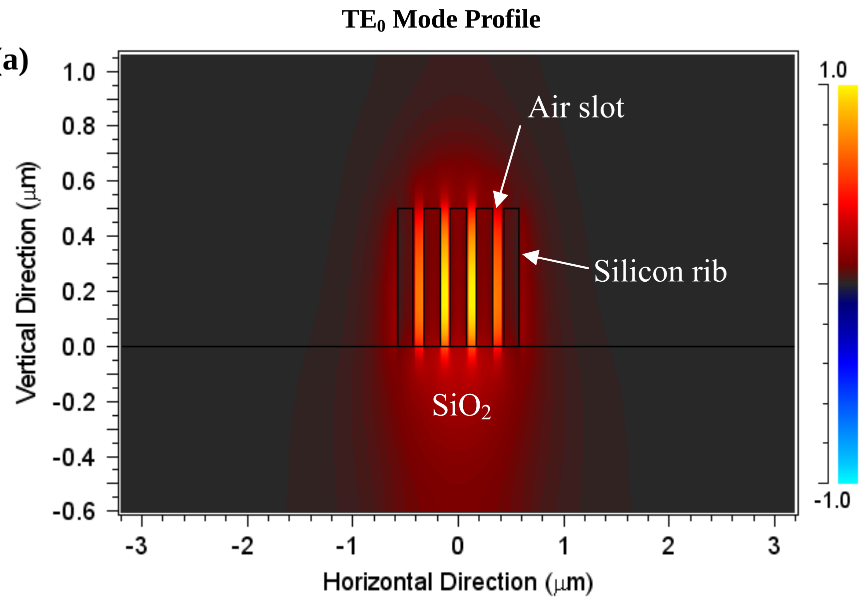

(b)

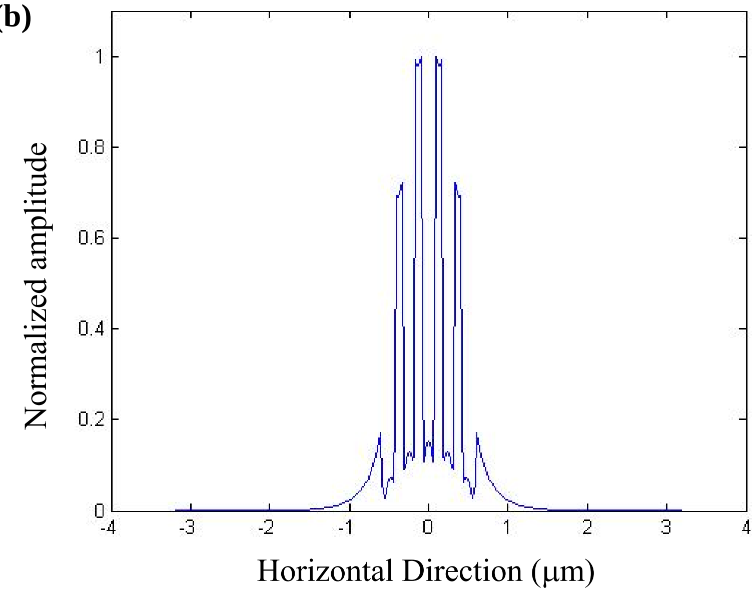

Figure 2-8. (a) The intensity profile of the TE_0 mode is illustrated. A brighter color indicates greater intensity electrical fields. Most of the electric field is concentrated in the air slots. (b) The mode amplitude in the air slot is significantly larger than the amplitude in the silicon ribs. The field intensity in the air is seen to be about 12 times larger than the field in the silicon ribs.

TM_0 Mode Profile

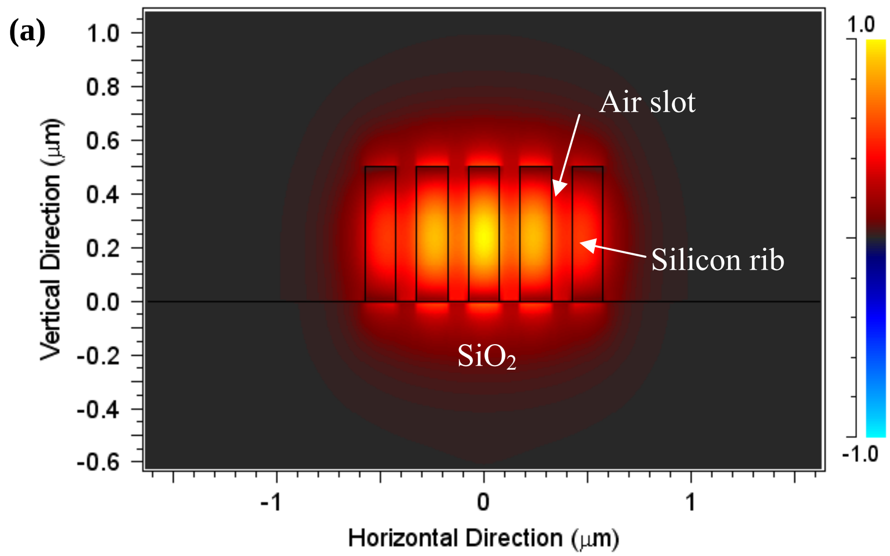

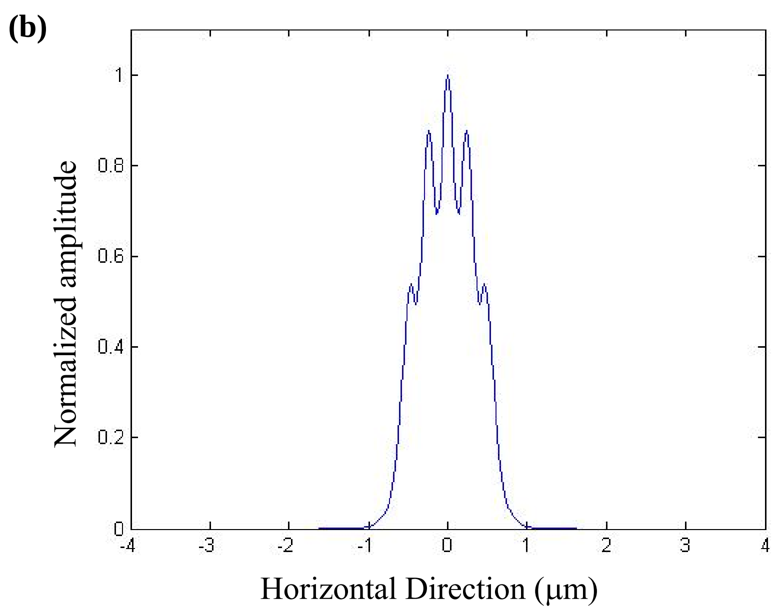

Figure 2-9. The TM_0 mode. (a) Most of the electrical field is concentrated in the silicon ribs. (b) The near field profile in the waveguide. The five peaks correspond to the five silicon ribs.

(a) TM_1 Mode

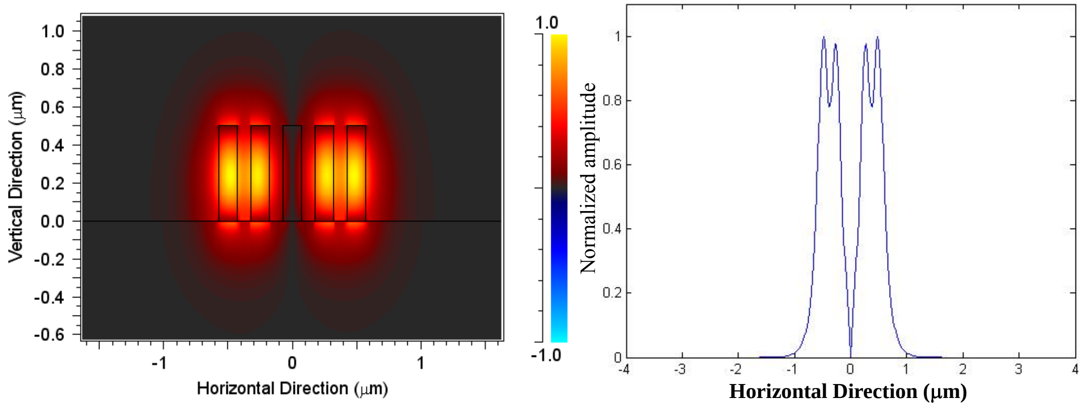

(b) TM_2 Mode

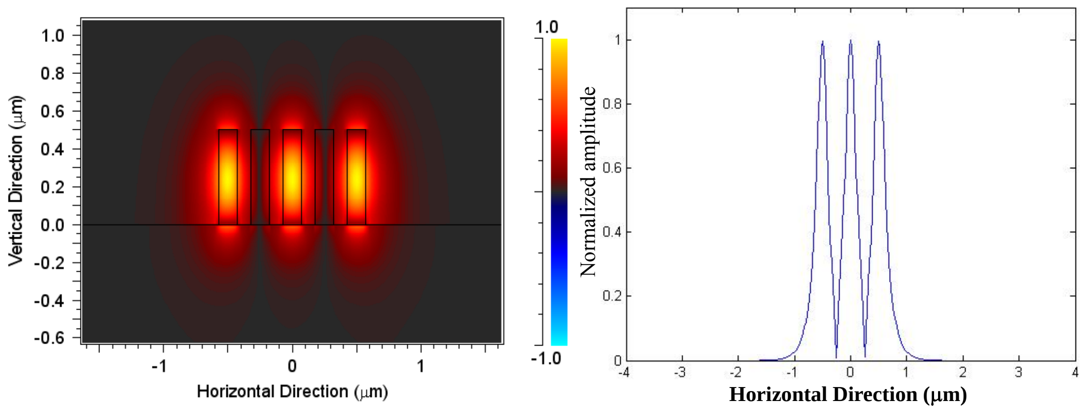

(c) TM_3 Mode

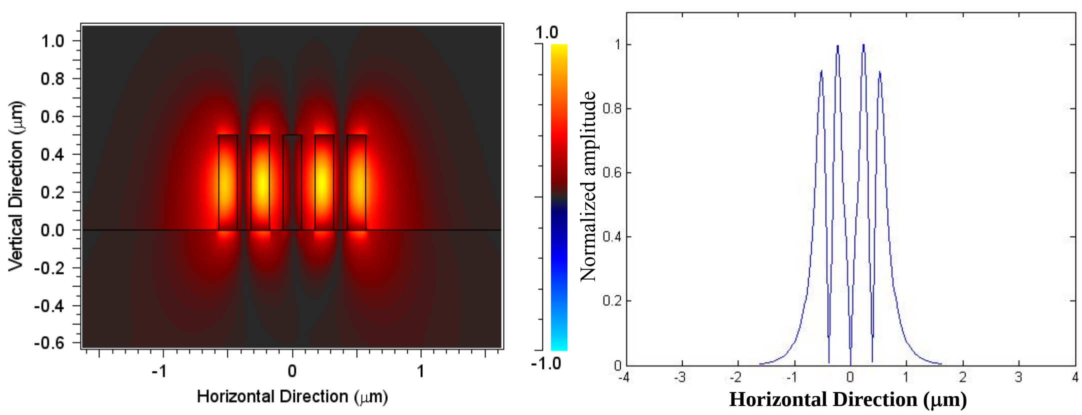

Figure 2-10. Higher order (a) TM_1 (b) TM_2 (c) TM_3 mode profile and electrical field amplitude.

Although the optimized waveguide dimensions of $1\mu m$ x $0.5\mu m$ allows higher-order modes to exist, it was seen that the TM_1 mode has a null exactly on-axis, i.e., in the center of the transverse cross-section, which is a high index region. Hence, this TM_1 mode is unlikely to be excited by the input waveguide, where the mode reaches its maximum value on-axis. However, further expanding the width would enable the unwanted TM_2 (Figure 2-10(b)) mode, which, like the lowest-order TM_0 mode, is peaked at the center, and could possibly be excited.

So far, the Δn_{eff} has been optimized by choosing *P*=250nm, *N*=5 and *q*=0.38. From equation (2-6), the group index has been optimized as well. But while EMT is applicable for plane waves, it might not be the case for waveguides. The group index variation versus filling fraction, *q*, was also simulated using FDFD (finite difference frequency domain) methods, shown in Figure 2-11(a). When q is greater the 0.4, the group index for the TE mode drops due to electrical field leakage into the buried oxide (Figure 2-12). When *q* is greater than 0.43, the TE mode is not supported, as discussed earlier. Figure 2-11(b) illustrates the Δn_g versus filling fraction *q*.

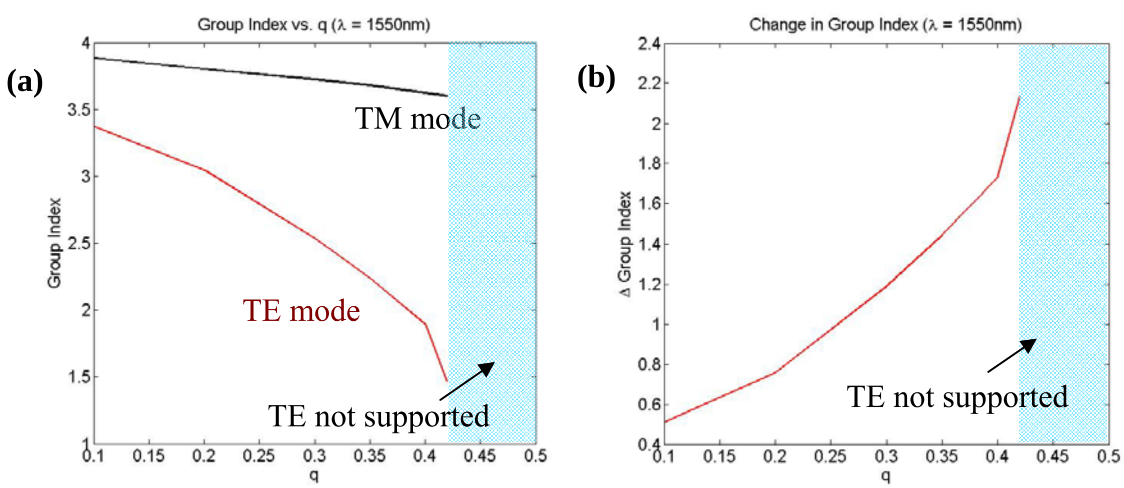

Figure 2-11. (a) Group index (n_g) for TE and TM modes versus filling fraction *q*. Both group indices decrease when *q* increases. (b) The group index difference (Δn_g) versus *q*. FDFD simulations were used to generate these plots. (Figure Courtesy: Michael Cooper)

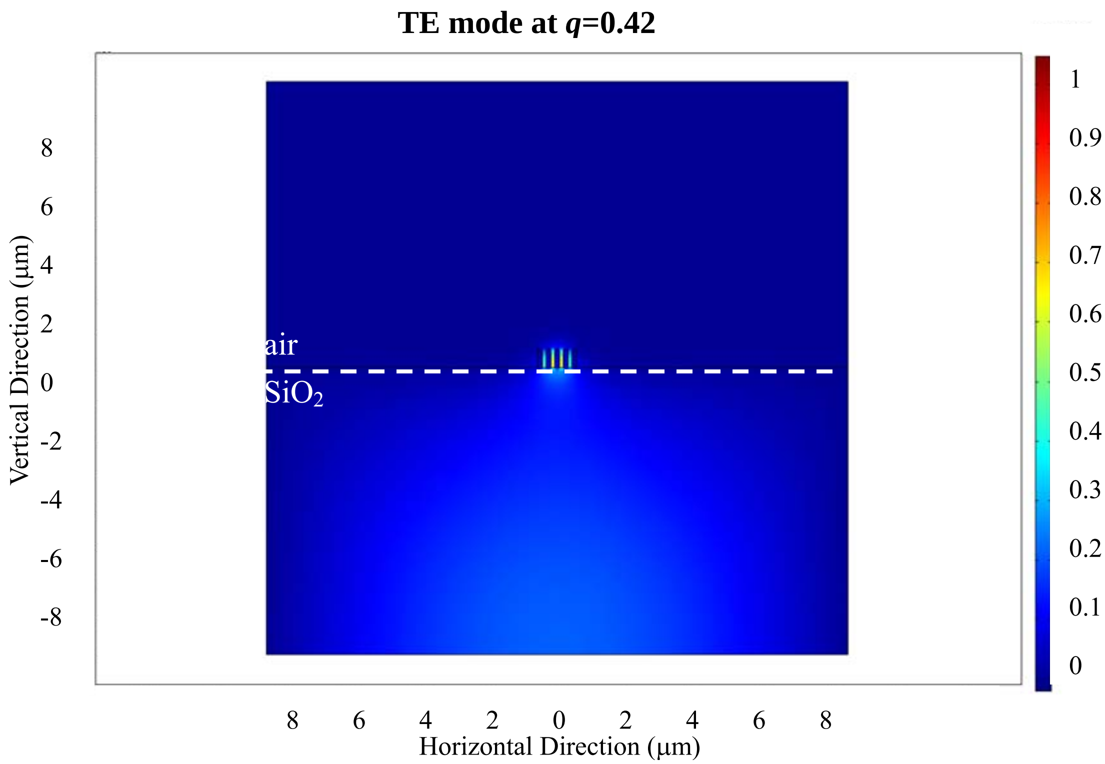

Figure 2-12. The electrical field contour plot of the TE mode in the waveguide and the cladding layer. The electrical field of the mode leaks into substrate leading to a low group index at q=0.42. (Figure Courtesy: Michael Cooper)

Hence, a q of around 0.4 was chosen in order to have a large group index difference, and prevent electric field leakage into the silicon dioxide substrate.

Finally, simulations were done on the group index (n_g) versus wavelength for examining its frequency/wavelength sensitivity. Figure 2-13 illustrates the group indices for the TE and TM modes. The group index difference (Δn_g) is ~1.6 from 1500nm to 1600nm. The bandwidth can be calculated using the well known equation $\Delta f = \frac{c}{\lambda^2}|\Delta\lambda|$ and it found to be 12.5THz. Additionally, using equation (1-3) and setting L = 1cm, the

DBP was calculated to be 6.67x10^2. Compared to the suggested value (14,000) for a delay line (for a storage of 235kb) application given by Tucker *et al*[2], the proposed design shows potential for enhanced optical delay line applications.

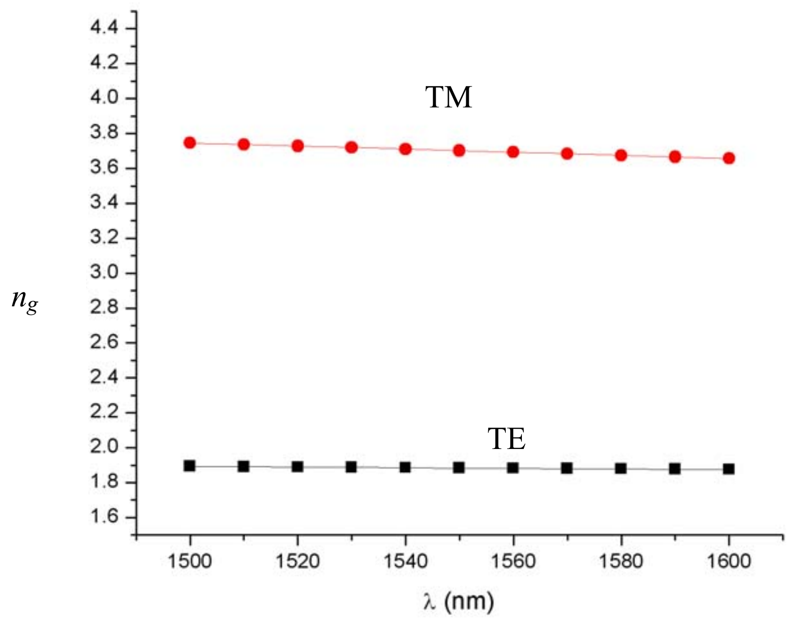

Figure 2-13. n_g versus wavelength. Δn_g is about 1.6 over a bandwidth of 100*nm* (1500 to 1600 *nm*).

2.2. Comparison of the characteristics of multi-slot and single-slot waveguides

In multi-slot waveguides, Δn_g is greatly enhanced in the TE mode as the electric field is concentrated in the low-index cladding regions. Whereas a significant fraction of the TE modal power (84%) resides in the air region for a single-slot waveguide[36], an even greater fraction (97%) is carried in the low index region in the optimized multi-slot waveguide. For the single-slot waveguide, it was found that the power fraction in the slot saturates[36] (see Figure 1-7). For the TM polarization, 42% of the modal power is carried in the silicon for the single-slot waveguide, while 64% is carried for the four slot waveguide structure. Consequently, the birefringence of the four slot waveguide is greater than that of the single-slot waveguide. Additionally, the degree of birefringence can also be controlled by altering the widths of the air slots and the silicon ribs. The birefringence does not increase if the number of silicon ribs is greater than 5.

Table 2-1. The multi-slot waveguide confines more TM-polarized light in the high-index regions, and more TE-polarized light in the low-index regions, than the single slot-waveguide. This is the physical reason for the enhanced birefringence of the multi-slot waveguide. Also, in the TM-polarized case, there is less light in the substrate than in the multi-slot case.

Comparison of single-slot and multi-slot waveguides		
Mode intensity	Single-slot[(a)]	Multiple-slots[(b)]
(TM) Fraction in silicon	42%	64%
(TM) Fraction in the substrate	51%	5%
(TE) Fraction in low-index region	84%	97%
(TE) Fraction in the slots (excl. substrate)	46%	77%

(a) s180 *nm* Si rib, 50 *nm* oxide slot, 300 *nm* height, oxide substrate[36]

(b) 150 *nm* Si rib, 100 *nm* oxide slot, 500 *nm* height, oxide substrate (our device)

Note: The TM polarization is defined as the one in which the electric field vector is transverse to the slab, and therefore, parallel to the slots. In each case, only the lowest-order mode was considered.

2.3. Comparison with Coupled Mode Theory

The modal theory of multi-slotted waveguides was described by Kapon *et al*[52]. In simulations it was observed that, in accordance with the general theory of supermodes[44, 53, 54], the peak field amplitudes *in the high index regions* for the m^{th} order mode obey the scaling inter-relationship[44]

$$C_n^{(m)} = \sin\left[\pi n(m+1)/(N+1)\right] \qquad \text{where } n = 1,2,\ldots,N. \tag{2-5}$$

N is the number of identical waveguides and $C_n^{(m)}$ indicates the coefficients of the individual eigenfunctions constituting a supermode. As discussed earlier (see Figure 2-7), the optimized multi-slot structure consists of five identical (N = 5) high-index (n_H = 3.48) sections separated by low-index gaps. For the fundamental (m = 0) modes, the supermode theory predicts: $C_n^0 = \left(\frac{1}{2}, \frac{\sqrt{3}}{2}, 1, \frac{\sqrt{3}}{2}, \frac{1}{2}\right)$.

Using a vectorial mode-solver program that utilizes FDFD algorithms to calculate the mode profiles, it is shown in Figure 2-14 that the peaks closely approximate the expected ratios. Furthermore, supermode theory predicts that the effective indices of the waveguides are shifted from the effective index of a single high-index rib waveguide, $n_{single\ w.g}$, according to the formula[52]

$$n_{eff}^{TE/TM} = n_{supermode}^{(m)} = n_{single.w.g.} + \frac{2\kappa}{2\pi/\lambda}\cos\left(\frac{\pi(m+1)}{N+1}\right) \tag{2-6}$$

where κ is the coupling coefficient. From Figure 2-4, $\kappa^{(TM)}$ = $0.81\mu m^{-1}$ and $\kappa^{(TE)}$ = $0.66\mu m^{-1}$ was calculated. These are very high values of coupling, achievable only in deeply sub-wavelength structures; in the optimized structure, the separation between the silicon ribs was ~100nm.

Waveguide couplers using multi-slotted waveguides can be designed either by laterally coupling two such waveguides formed on the same substrate, in which case the coupling is dominated by the overlap of the tails of the outer-most regions only (a straightforward extension of the single-slot waveguide coupler[35, 55, 56]), or by vertically coupling multi-slot waveguides which are formed on two separate layers. The coupling coefficient can be much larger in the vertical coupling case, since the entire lateral extent of the mode is involved in defining the coupling integral, but the coupling coefficient can be quite sensitive to lateral misalignment of the two layers. In either case, the coupling coefficients will be substantially different for the TE and TM polarizations, which may be exploited to make very compact polarization splitters.

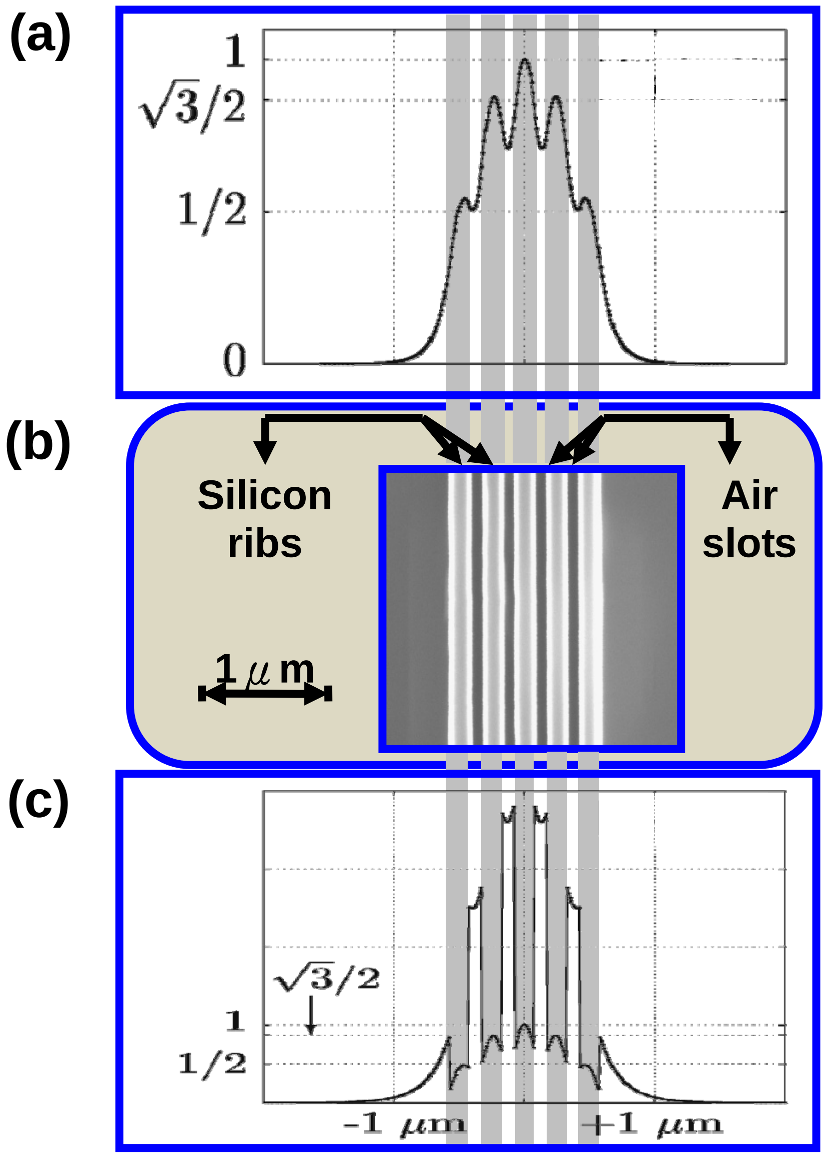

Figure 2-14. (a) The relative amplitude of the TM mode in the 5 silicon rib multi-slot waveguide. The peak intensity in the silicon ribs is close to supermode theory predictions. (b) Magnified scanning electron microscope (SEM) image of multi-slot waveguide. (c) The amplitude of electrical field for TE mode. The relative peaks in the silicon ribs still follow supermode theory predictions. (Figure courtesy: S.-H. Yang *et al*, Optics Express, Vol. 16, p.8306, 2008)

2.4. Summary of chapter

In this part of thesis, the multi-slot waveguide design was optimized (table (2-2)) through EMT and simulations using FDFD methods. It is shown that five 150 *nm* wide silicon ribs with four 100*nm* air gaps in between provide guided TE and TM modes and largest achievable birefringence. Based on the simulation results, the DBP of ~$6.67X10^4$ was calculated and exhibits potential for future optical delay line applications.

In the next few chapters, details in fabricating the waveguides and verifying of the predictions of this chapter will be discussed.

Table 2-2. Optimized design of features in multi-slot waveguides

Parameter	Values	Reason
Grating period (*nm*)	250	Due to the fabrication limitation
Filling fraction (*q*)	0.4	Achieve maximum group index difference
Number of silicon ribs (*N*)	5	Gives maximum group index difference (Figure 2-5)

This chapter, in part, have been published as "Giant birefringence in multi-slotted silicon nanophotonic waveguides" by S. H. Yang, M. L. Cooper, P. R. Bandaru and S. Mookherjea, Optics Express, Vol. 16, 8306 (2008).

Chapter 3: Multi-slot waveguide fabrication

Standard semiconductor processes were used to fabricate the vertical multi-slot waveguides. Figure 3-1 illustrates common fabrication methods for semiconductor processing. The fabrication process was compatible with silicon based CMOS technology and allows easy on-chip integration. Optimal parameters for multi-slot waveguides are presented.

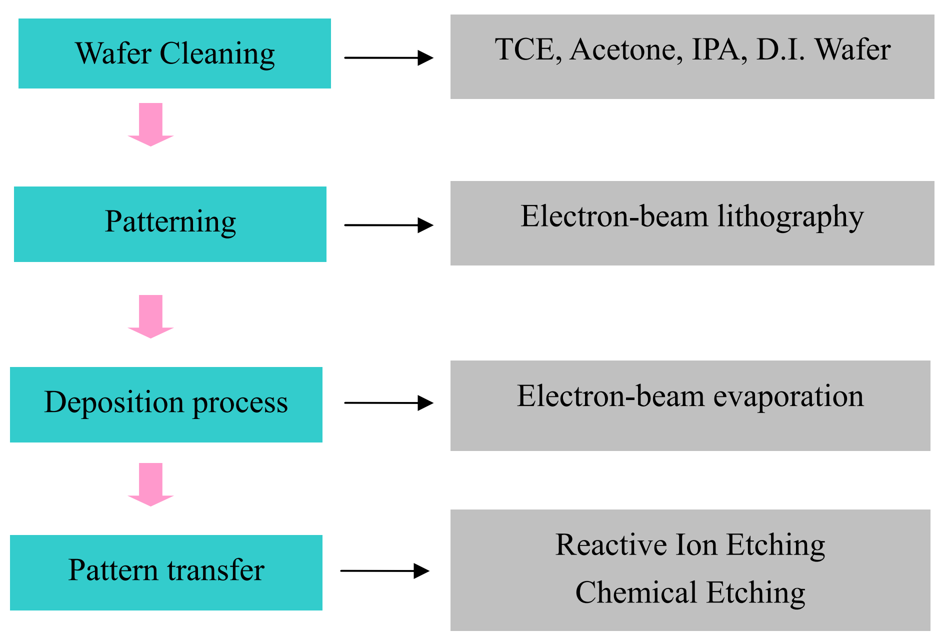

Figure 3-1. Semiconductor fabrication flow chart.

3.1. Fabrication

A silicon-on-insulator (SOI) wafer with a layer of 500*nm* silicon (*p*-doped, 10*Ω-cm* resistance) on top of 1μm silicon dioxide was used to fabricate the multi-slot waveguides. The device design is shown in Figure 3-2. The multi-slot waveguide is indicated in red.

The strip waveguide used to feed the laser into the multi-slot waveguide and collect the same is also shown. An "L" shape bend was created to avoid the direct input to output fiber coupling. A large bending radius (~60μm) was used to minimize the bending loss[57]. The device was separated by a short gap (400*nm*) so that a precise known length was created for Fabry-Perot measurements.

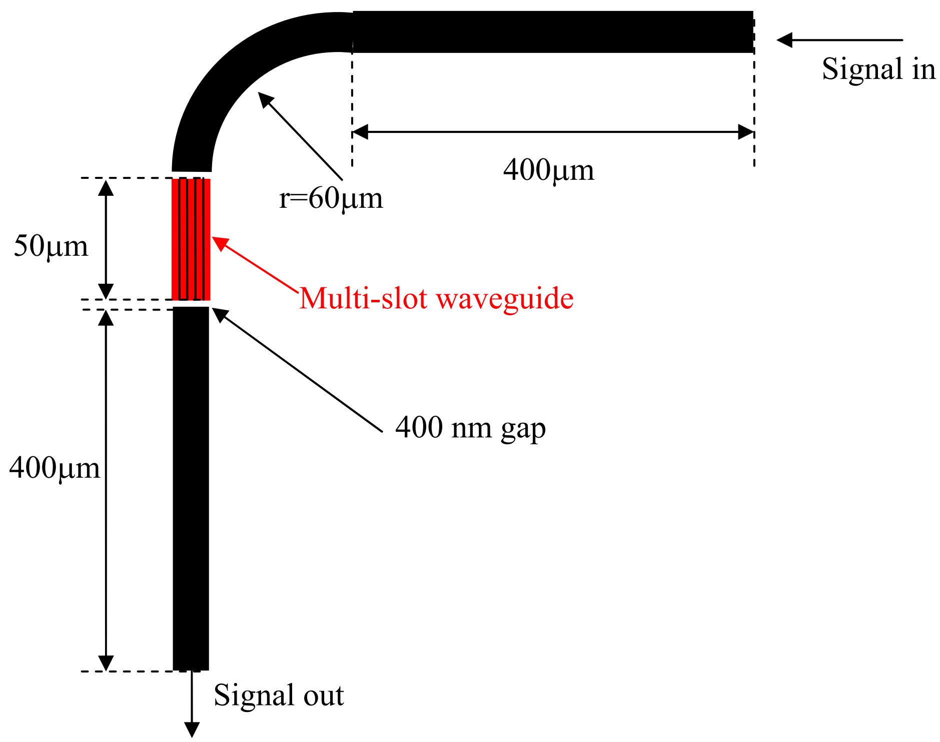

Figure 3-2. The overall waveguide structure. The multi-slot waveguide is 50μm long. A 90^o bend was created to avoid direct fiber to fiber coupling. The device was separated by a short gap (400*nm*) so that a precise known length was created for Fabry-Perot measurements.

SOI chips used for fabrication of multi-slot waveguides were successfully cleaned ultrasonically in Trichloroethylene (TCE), Acetone, Isopropanol (IPA) and deionized (D.I.) water regent for 15 minutes each. The sample was blow-dried with nitrogen gas between each cleaning step.

3.2. E-beam lithography

Following wafer cleaning, poly(methyl methacrylate) (PMMA) was spin-coated onto the silicon chip (3000*rpm*, 60 seconds) and subsequently baked on a hot plate at 180 °C for 5 minutes. The PMMA thickness was about 300*nm* as measured by the Filmetric F20 system. 495K 4% PMMA in chlorobenzene solution was used as positive e-beam resist. A higher molecular weight (MW) resist (e.g., PMMA 950K C) could have higher resolution for electron beams. However, it has been reported that such resists have significant swelling issues[58] while sub-5*nm* lines with low MW resists have been successfully achieved[59].

The designed pattern (Figure 3-2) was exposed using a JEOL JSM-IC 845 scanning electron microscope (SEM), optimized for e-beam lithography[60]. A Nanometer Pattern Generation System (NPGS, J.C. Nabity Lithography Systems, Bozeman, MIT) software was used for controlling e-beam parameters. The exposure time was calculated by using the equation

$$t = \frac{D \times A}{I_b} \tag{3-1}$$

where D is dose per unit area (C/cm^2), A the exposed area (cm^2), I_b the probe beam current (A) and t is the exposure time (s). Although larger beam currents can reduce exposure time, the resolution is compromised due to large beam size. 50*pA* was found to be the largest current to allow for 100*nm* resolution. The dosage was optimized to be ~300$\mu C/cm^2$. Using equation (3-1), the total exposure time was calculated to be ~60 seconds.

After exposure, the sample was developed in Methyl isobutyl ketone (MIBK) : IPA (1:3)[61, 62] solution for 1 minute. The sample was then rinsed in IPA for 30 seconds to wash off the developer. Figure 3-3 schematically illustrates the e-beam writing process.

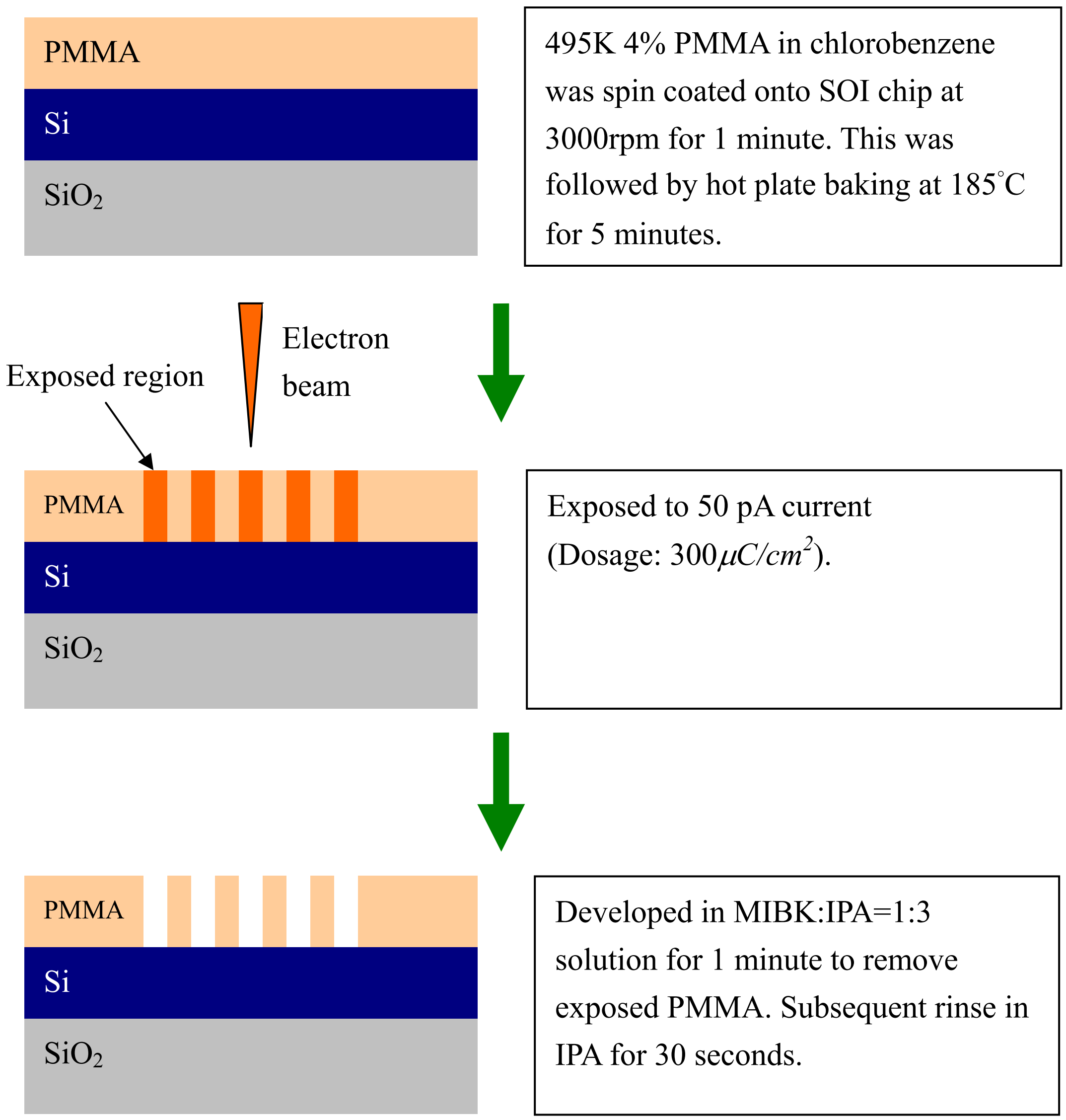

Figure 3-3. Flow chart of E-beam lithography process.

3.3. Hard mask fabrication (E-beam evaporation)

A hard metal mask template, Ni, was used for pattern transfer. Nickel (~35*nm*) was e-beam evaporated onto the developed PMMA pattern. The deposition rate was controlled at 0.1*nm/s* in a Temescal BJD 1800 e-beam evaporator. Boiling acetone (in a water bath) was used for the following lift-off process. Ultrasonic agitation in acetone for 30*s* helped remove the residual PMMA and nickel. Figure 3-4 schematically illustrates the fabrication process.

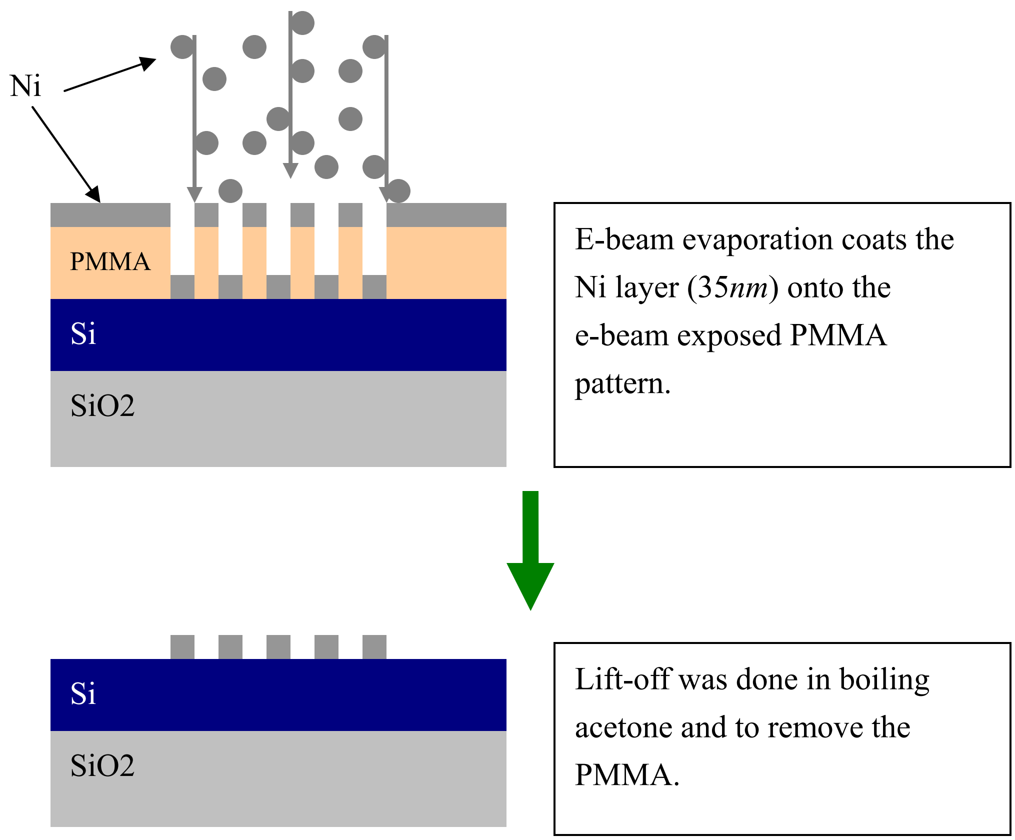

Figure 3-4. Ni hard mask deposition flow chart.

3.4. Reactive ion etching

Reactive ion etching (RIE), a dry-etching process, was performed for pattern transfer.

RIE relies on physical bombardment of reactive ions onto the substrate and is an anisotropic etching process. During the RIE, an oxygen plasma descum step was first performed (200W RF power, 50 *mTorr* pressure, 15 minutes), followed by an RIE etch using a mixture of BCl_3 (10 *sccm*) and Ar (10 *sccm*) at 100W RF power and 30 *mTorr* pressure at room temperature for 7 minutes. The etching parameters were optimized to give an aspect ratio of 5:1 (slot height : slot width), according to the design of Figure 2-7. [During the etching process, ion bombardment had to be stopped every 40 seconds in order to cool the sample. This was to prevent the sample temperature from rising and melting the Ni pattern, as shown in Figure 3-5.]

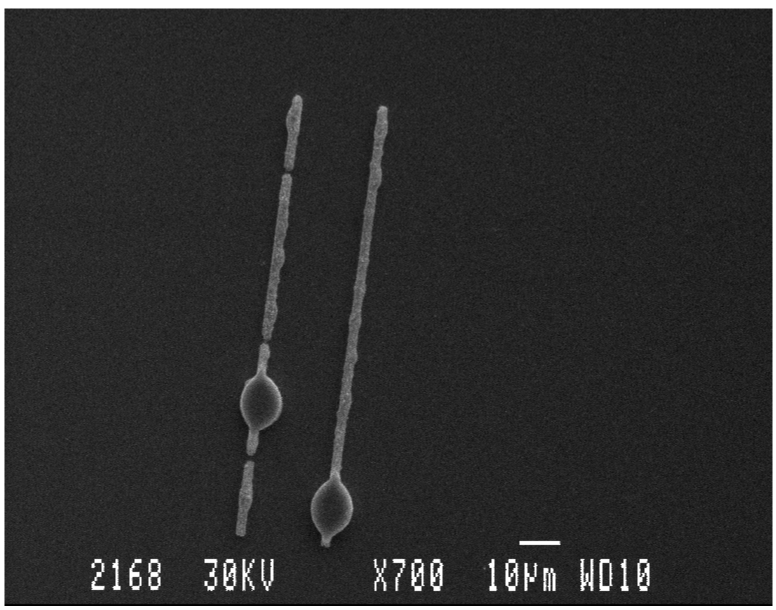

Figure 3-5. Scanning electron microscope (SEM) image of a melted Ni pattern.

After etching, the sample was immersed in Nickel Etchant (Transene, Type TFB) for 1 minute and subsequently rinsed in water for 5 minutes to remove the Ni mask. Figure 3-6 schematically illustrates these steps.

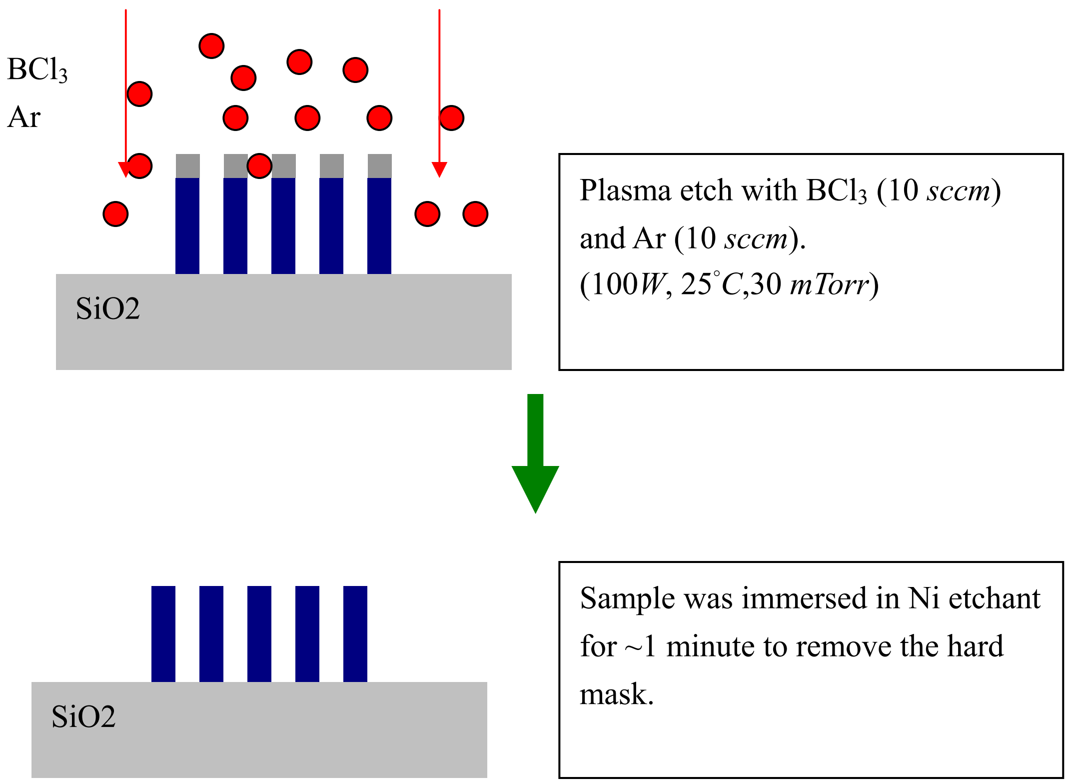

Figure 3-6. The etching and Ni removal process

Figure 3-7 shows the SEM image of the multi-slot waveguide, after the etching and Ni removal. Six devices, separated about 15μm from each other, were fabricated on a SOI chip.

(a)

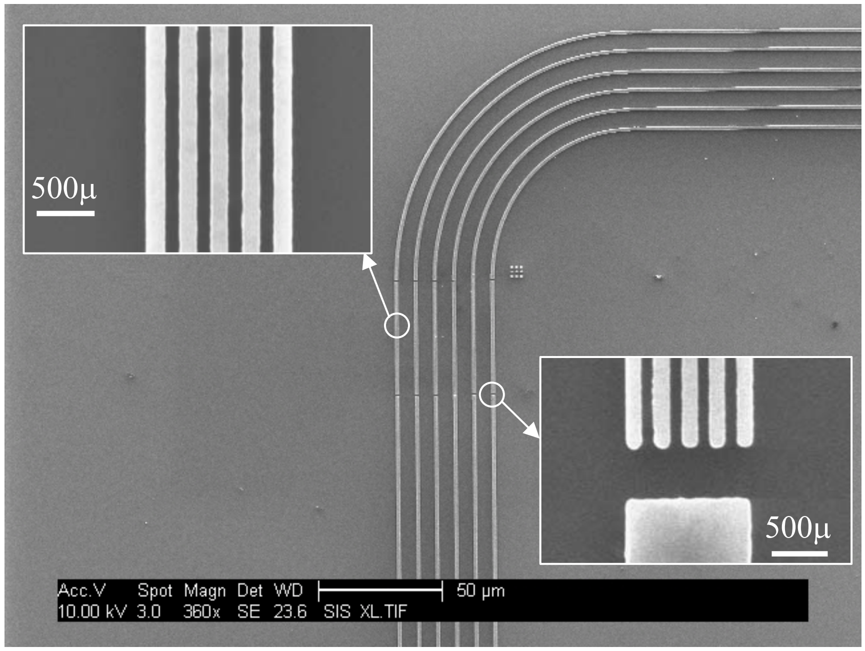

(b)

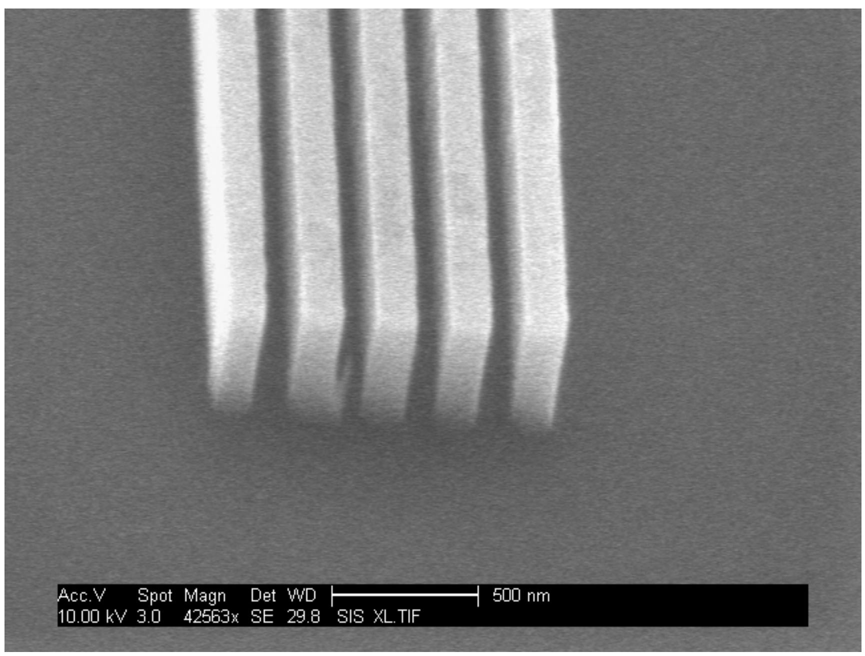

Figure 3-7. Scanning electron microscope (SEM) image of the fabricated waveguides. (a) A total of six devices were fabricated. A 400*nm* gap was introduced to separate the multi-slot waveguide from the strip waveguide (b) 45° view of the multi-slot waveguide cross-section.

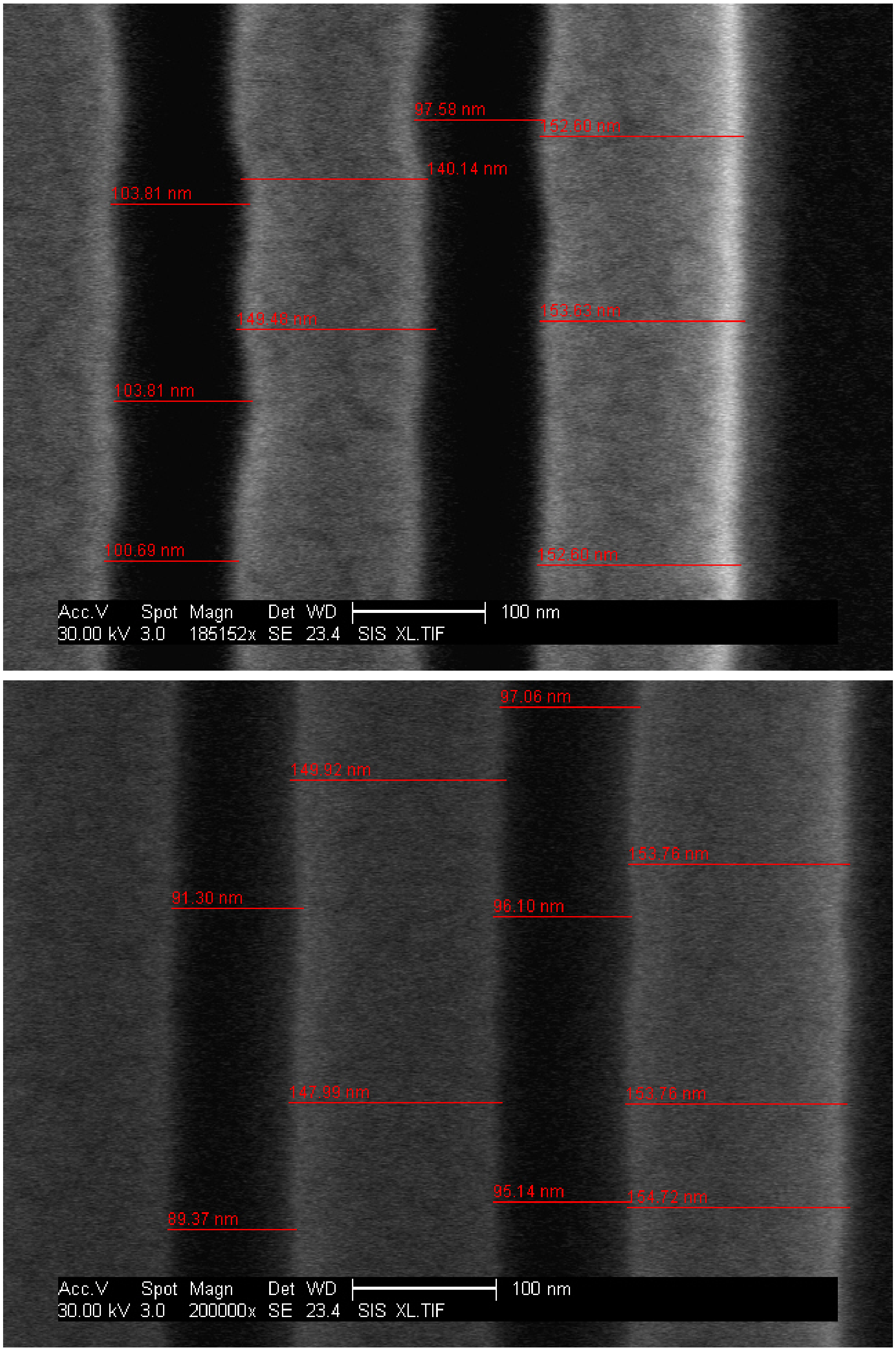

Figure 3-8. The length scales of the multi-slot waveguide were measured in the SEM. The slot width was 100 (±5) *nm* and the slot-to-slot spacing was 150 (±5) *nm*, yielding an optimal air filling fraction $q = 0.40$ (± 0.02).

Multi-slot waveguides consisting of four air slots in a silicon core were fabricated. The dimension of the fabricated device was measured by a Philips XL30 FEG ESEM, with the image capture and analysis using AnalySIS XL DOCU software (Soft Imaging System, Lakewood, CO) as shown in Figure 3-8. (The sample was coated with $3nm$ of Au in order to enhance contrast.). The error in the SEM length measurement, for the multi-slot waveguide length scales was estimated to be $\pm 5\ nm$.

The final step was to cleave the chip for facilitating coupling of the laser into the waveguide. The chip was lapped down to ~$150\mu m$, from ~$650\mu m$ and then cleaved and mounted onto a sample holder for measurements, which will be reported in the next chapter.

Chapter 4: Multi-slot waveguide characterization and mode shaping

Group indices of multi-slot waveguides for both the TE and TM modes were measured through the characterization of the free spectral range (FSR) of Fabry-Perot resonators. The results were in good agreement with the theoretical and simulated values confirming the predicted large birefringence of vertical multi-slot waveguides. The DBP was then derived and compared with extant optical delay line schemes. Loss measurement was performed on multi-slot waveguides with different lengths. In order to reduce the polarization-dependent coupling loss between multi-slot waveguides and external optics, a mode shaping tool was designed.

4.1. Group refractive index measurements

The group refractive indices of the TE and TM modes were measured through the transmission spectra of Fabry-Perot resonators. A Fabry-Perot resonator is a resonant cavity formed by two parallel reflecting interfaces, as illustrated in Figure 4-1. The light in the cavity will experience multiple reflections and transmissions such that the total transmitted light intensity (I_T) can be expressed by,

$$I_T = I_0 \frac{(1-R)^2}{1-2R\cos\left(\frac{4\pi n_g d}{\lambda}\right)+R^2} \tag{4-1}$$

where I_0 is incident power, R is the reflectance at the interface, d the device length and n_g the group refractive index. As seen through equation (4-1), the transmission is a function of wavelength and exhibits peaks of large transmission corresponding to the resonance wavelength of the resonator (Figure 4-1). The wavelength separation between adjacent transmission peaks is defined as Free Spectral Range (FSR) and is given by

$$FSR \cong \frac{\lambda_0^2}{2n_g d} \tag{4-2}$$

where λ_o is the central wavelength of the two adjacent transmission peaks. The group index is then calculated by:

$$(n_g)_{\text{TE/TM}} \cong \frac{\lambda_0^2}{2(FSR)d} \tag{4-3}$$

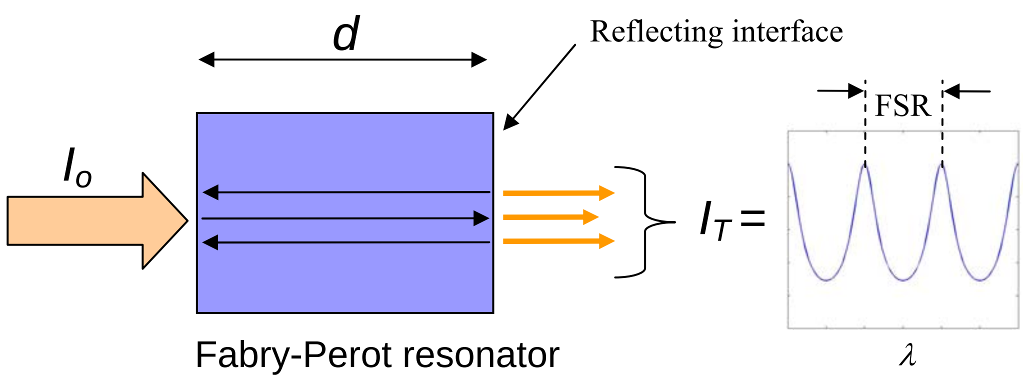

Figure 4-1. The principle of Fabry-Perot resonator. Incident light (I_o) will experience multiple transmission and reflection events, giving rise to transmitted intensity (I_T) variations with wavelength (λ) as shown on the right hand side.

In the multi-slot waveguide, a precisely known Fabry-Perot resonator length (*d*) was created by a short separation between the multi-slot waveguide and the strip waveguide.

4.1.1. Transmission spectra measurement setup

The schematic setup for transmission spectra measurement is shown in Figure 4-2. A C+L band (1510nm-1640nm) tunable laser source (Agilent 81640A, wavelength accuracy ±0.015 *nm*) was used as the input. The laser was first connected to a single mode fiber with an in-line polarizer and then connected to a polarization maintaining (PM) fiber (Oz-Optics). The tapered fiber is aligned to the chip using a six-axis micrometer stage (Newport Ultralign) equipped with differential micrometers. The transmission spectrum was recorded by sweeping the laser wavelength (1520-1620*nm*) and monitoring the output using an InGaAs photodiode (working range: 0.9 μm-2.1μm).

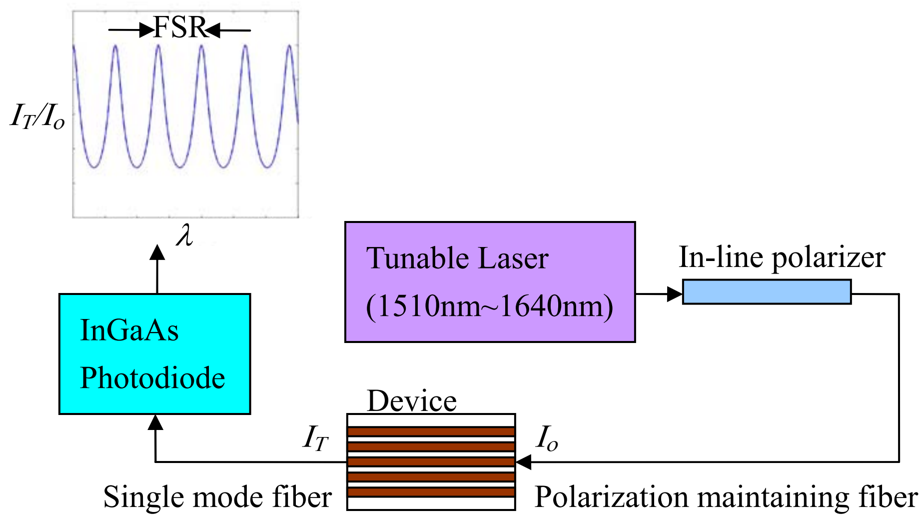

Figure 4-2. Schematic of the transmission spectra measurement setup. The output signal from the device was detected by InGaAs photo detector.

4.1.2. Results

In order to measure the group indices of the slotted waveguide sections, the multi-slot section was separated from the normal input/output waveguides by short (~0.4 μm) air gaps so that a Fabry-Perot resonator of precisely-known length was created. As shown in Figure 4-3, typically six waveguides were fabricated on each chip. The device lengths were measured using a SEM, shown in Figure 4-4.

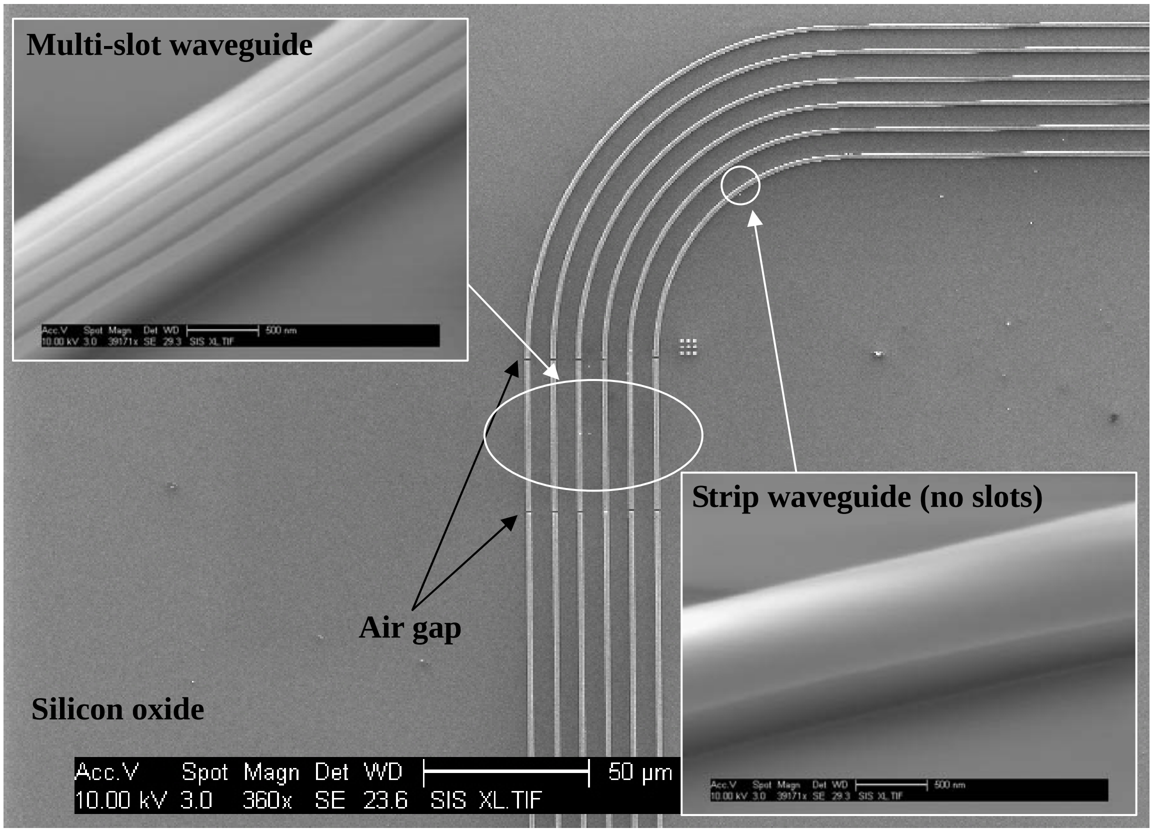

Figure 4-3. Scanning electron microscope (SEM) image of a multi-slot waveguide. Six multi-slot waveguides were typically fabricated on one chip. A short air gap was created to separate the multi-slot waveguide from the strip waveguides, to create a Fabry-Perot resonator in the multi-slot waveguide.

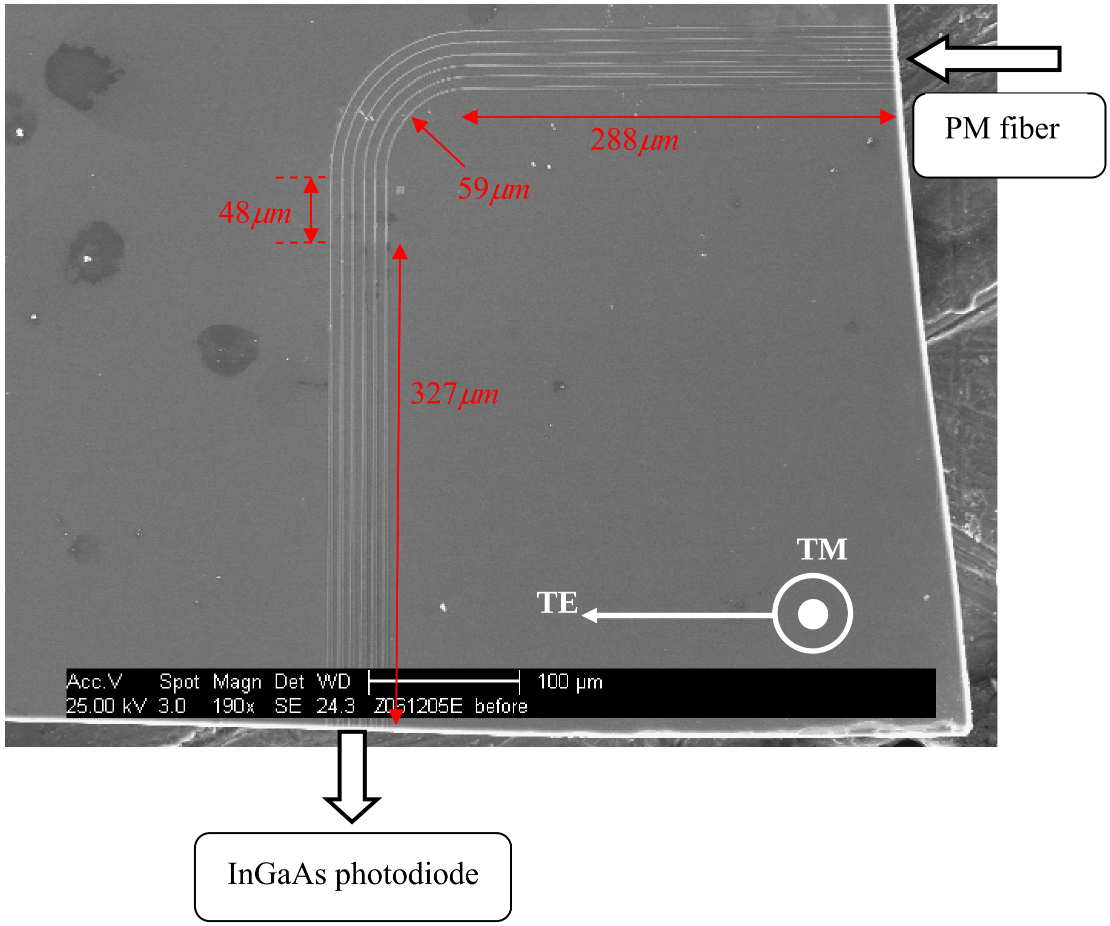

Figure 4-4. Scanning electron microscope (SEM) image of a cleaved chip. The multi-slot waveguides were ~48μm long. The laser was input into the multi-slot waveguide after a 90° bend. The transmitted power was collected at the bottom using a InGaAs photodiode.

The measured transmission spectrum is shown in Figure 4-5. The FSR is more clearly defined for the TE mode (where the electrical field is parallel to the substrate) since the effective index contrast between the air and multi-slot waveguide is greater for the TE mode. However, most of the resonances were not well defined due to significant high frequency noise (Fabry-Perot resonance of strip waveguide, imperfection in the waveguide, etc.) making precise FSR determination difficult.

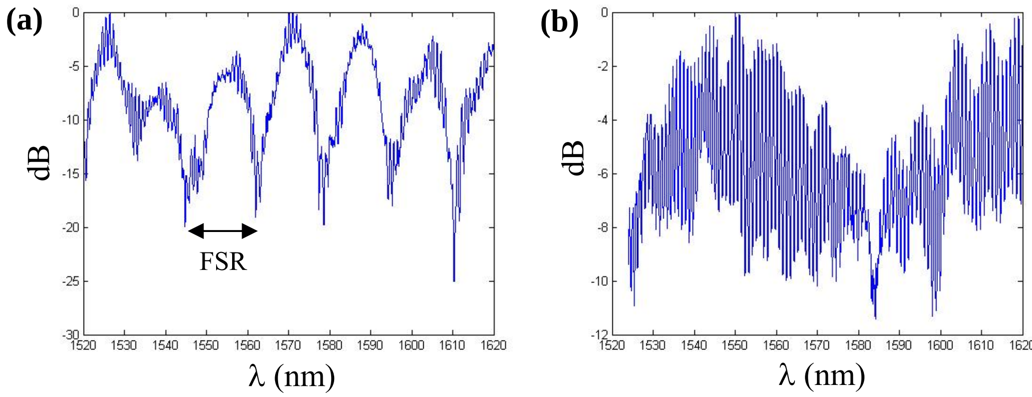

Figure 4-5. Experimental transmission spectra of multi-slot waveguide with (a) TE and (b) TM modes. The FSR is better defined in the TE mode, due to the greater refractive index contrast for this mode.

The measured transmission spectrum was filtered using a Gaussian filter in the frequency domain to extract particular frequency components which correspond to the Fabry-Perot resonances of the multi-slot waveguide. This frequency component can also be estimated from simulated group indices. According to the simulation (see Figure 2.11), the group indices for TE and TM modes were estimated to be 1.8951 and 3.6238 respectively. As the length of the fabricated multi-slot waveguide was measured to be 48 μm (Figure 4-4), the FSR of the multi-slot waveguide (at $\lambda = 1.55\mu m$) was calculated to be 13.2 *nm* (TE) and 6.9 *nm* (TM), using equation (4-2). Consequently, in the frequency domain, a peak is expected approximately at 0.075 nm^{-1} (1/13.2 nm) and 0.145 nm^{-1} (1/6.9).

Figure 4-6 plots the Fourier transform of the experimental transmission spectra (Figure 4-5) superposed with results generated from simulations showing good agreement. Higher frequency components arise from the resonances of the longer strip waveguide.

The measured data ranges from 1520*nm* to 1620*nm*, thus, the resolution in frequency domain is computed as $\frac{1}{1620-1520}=\frac{1}{100}=0.01(nm^{-1})$. In order to increase resolution, the measurement bandwidth must be increased.

In Figure 4-6, the first peak corresponds to the FSR of the multi-slot waveguide section while the second peak is related to the resonance of the strip waveguide. As the lengths of the two strip waveguides (before and after the multi-slot waveguide) are about the same, only one broad peak is observed ~1nm^{-1}.

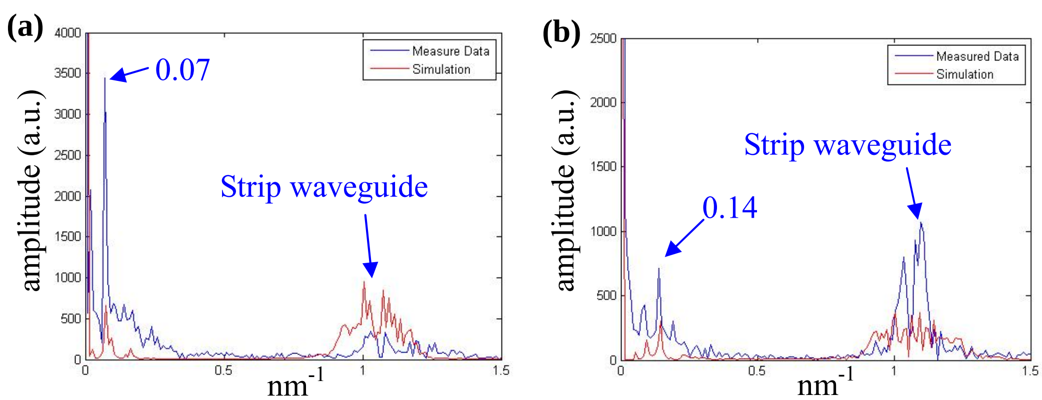

Figure 4-6. Fourier transform of transmission spectra. In is seen that the distinct peak located at (a) 0.07 nm^{-1} for the TE mode and (b) 0.141 nm^{-1} for the TM mode. The second peak at ~1 nm^{-1} is due to the strip waveguide.

Figure 4-7 shows a Gaussian Pass Filter (GPF) centered at the multi-slot waveguide resonance peak. (A GPF is used instead of band pass filter is because of the exponentially decaying weight from the frequency of interest). Consequently, high frequency components resulting from the strip waveguide resonances were filtered completely. Figure 4-8 plots a frequency filtered Fourier transform.

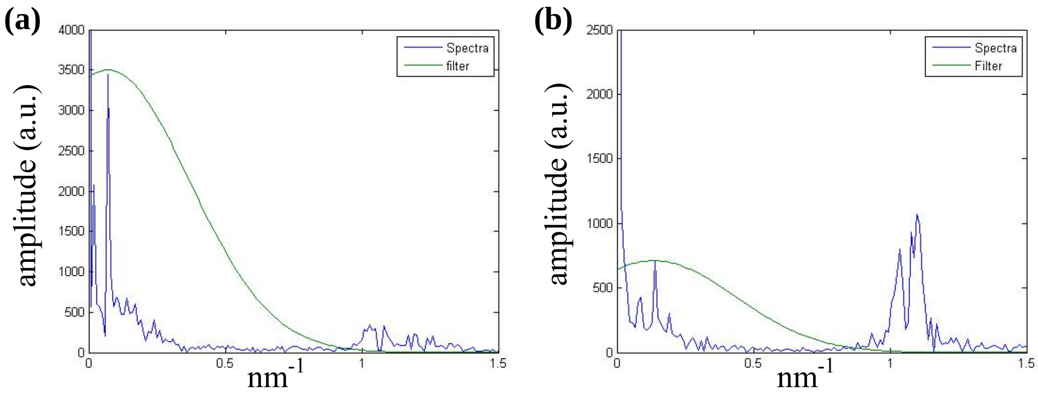

Figure 4-7. The green curve is the Gaussian filter centered at (a) 0.07 nm^{-1} for the TE mode and (b) 0.14 nm^{-1} for the TM mode.

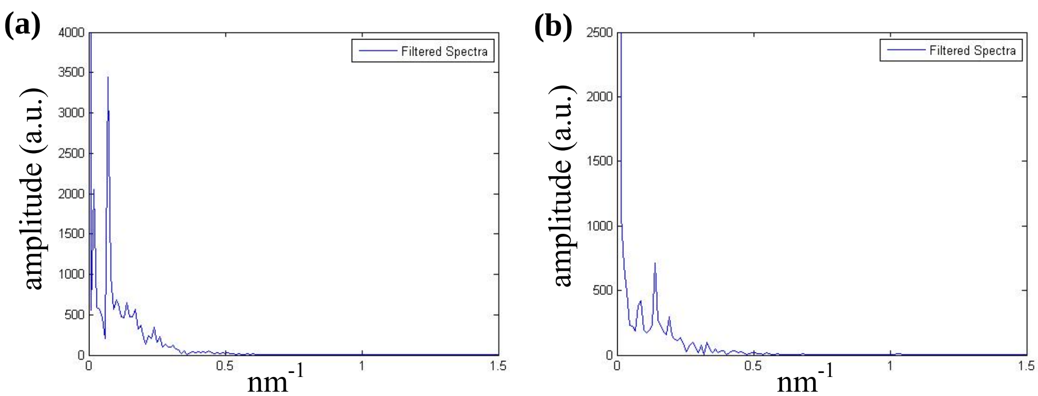

Figure 4-8. Filtered frequency spectra for (a) the TE mode and (b) the TM mode. High frequencies due to the strip waveguide were filtered.

The inverse Fourier transform of the filtered data is shown in Figure 4-9, from which the FSR was extracted at each wavelength and used to calculate the group index (n_g) through equation (4-3).

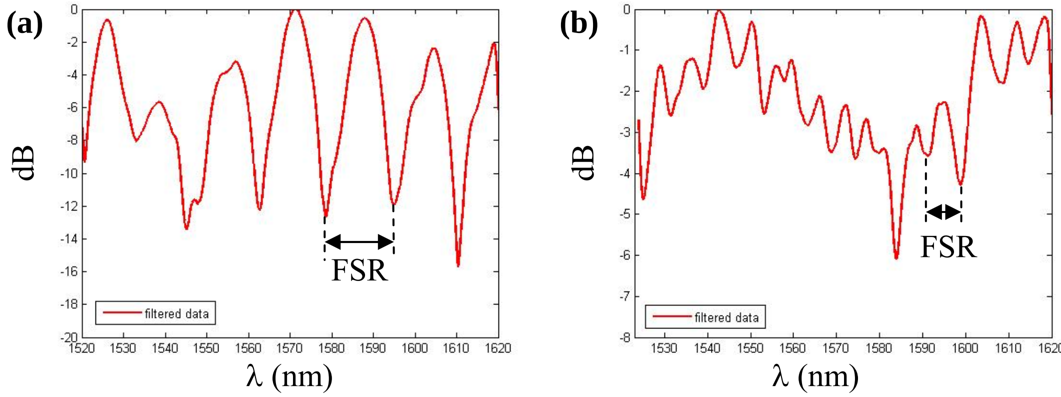

Figure 4-9. Inverse Fourier transform of Gaussian filtered data of the (a) TE and (b) TM modes. The FSR is clearly shown. From the filtered data, FSR can be determined and used to calculated group indices.

Calculated group indices (n_g) at different wavelength were plotted in Figure 4-10. The experimental values agree very well with the simulated results. Large birefringence was successfully observed from the group index difference (Δn_g) which is about 1.6 and is nearly twice as large as has previously been achieved. This confirmed that large birefringence can be achieved in multi-slot waveguide. Additionally, the group index (Δn_g) difference is relatively constant over a bandwidth of 60*nm* (1530-1590*nm*). The error bars on the data are not uniform as the Fabry-Perot oscillations from the cleaved facets of the input and output waveguides impose strong wavelength-dependent fluctuations which cannot be completely filtered out.

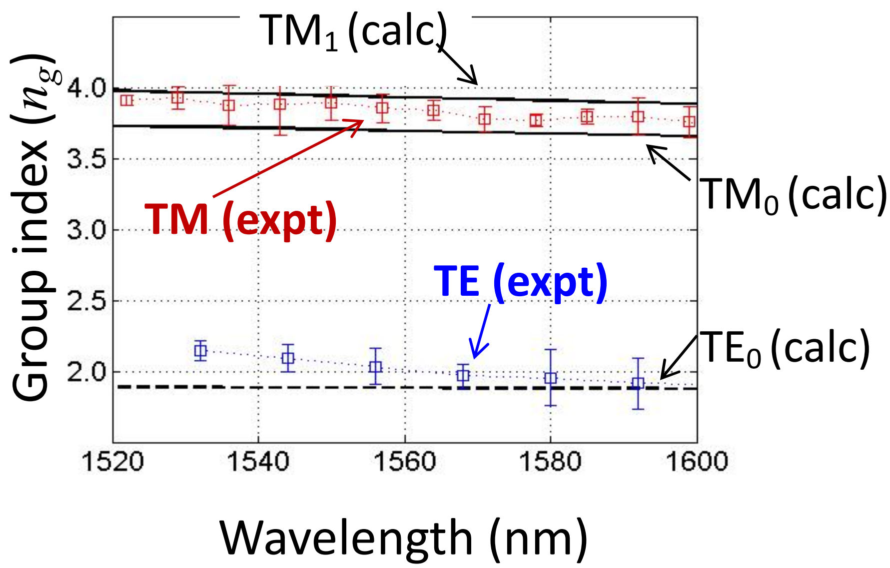

Figure 4-10. Measurement (labeled ‘expt’) of the group index versus wavelength for the TE and TM polarizations. The simulations are labeled ‘calc’. Although the latter shows that the higher-order mode TE_1 may exist, it is unlikely to be excited by the input coupling due to symmetry considerations, and is not observed at the output. The colored broken dotted line connecting the measurements, which are indicated by squares with error bars, is only a guide to the eye. (Figure courtesy: S.-H. Yang *et al*, Optics Express, Vol. 16, p.8306, 2008)

4.1.3. Dispersion of Multi-slot waveguides

When a waveguide has a frequency dependent group index, it is said to be dispersive. The group velocity dispersion (GVD) is used to describe this dispersion and is given by,[34]

$$D = -\frac{1}{c}\frac{dn_g}{d\lambda}. \qquad (4\text{-}4)$$

From a linear best-fit of this data (Figure 4-10), it was estimated that the group velocity dispersion of TE-polarized light is 2.7 times larger than that of TM-polarized light [$D^{(TM)} = -8.0\times10^3$ *ps/nm-km*, $D^{(TE)} = -2.1\times10^4$ *ps/nm-km*]. There values are of the same order of magnitude as the single-slot waveguide[35], but an order-of-magnitude less than photonic crystal waveguide delay lines[7, 8, 12, 26, 63]. The group index is basically determined by the waveguide geometry rather than its material properties. It is interesting to note that the group index $n_g^{(TM)}$ exceeds the refractive index of bulk silicon and is due to the high index contrast between silicon and air which leads to strong optical confinement and larger $n_g^{(TM)}$.

4.1.4. Group index versus filling fraction *q*

In order to demonstrate that the birefringence of multi-slot waveguide was maximized at q~0.4, several multi-slot waveguides with differing q values were fabricated and investigated. The measured group indices were overlaid on simulated values as shown in Figure 4-11. The measured group index for the TE mode at different q values agrees well with simulations. For the TM mode, measured values are higher than simulated values. Error bars of q values were calculated by measuring the variation of slot and silicon ribs width using SEM and error bars of group indices are were calculate by measuring three devices at each q value and calculate the standard deviation.

The disagreement of group indices between experimental and simulated values of the TM mode could possibly be due to the higher order TM modes being excited. When the filling fraction (q) is decreased, the aspect ratio (slot height : slot width) of the slot in multi-slot waveguides is increased. However, due to experimental (etching) limitations, the aspect ratio could not be greater than ~5. Therefore, the slot was not etched through the silicon all the way to the silicon dioxide. Hence, the electrical field of the TM mode could leak into the neighboring ribs through the un-etched silicon to excite higher order TM modes.

Figure 4-11(b) compares group index difference of the measured and simulated values. The disagreement arises from the group indices of the TM mode were mentioned earlier. However, the birefringence seemed to saturate at ~q=0.4 which confirms that the Δn_g was optimized in our multi-slot waveguides.

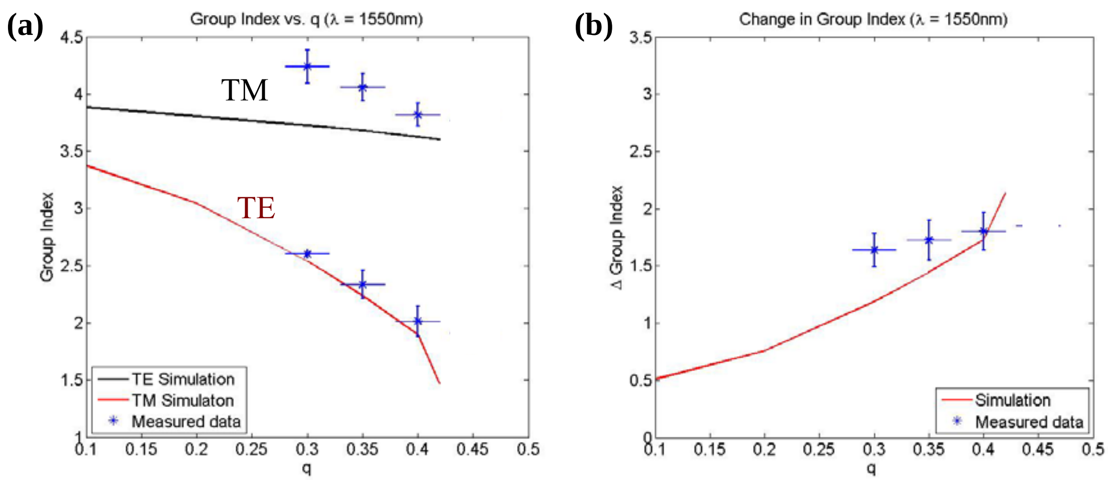

Figure 4-11. (a) The group index of multi-slot waveguide versus different q. The group indices of the TM mode are higher than simulated value could due to the excitation of higher order TM mode. (b)The group index difference between the TE and TM modes. (Figure Courtesy: Michael Cooper)

4.1.5. DBP of multi-slot waveguides

The multi-slotted waveguide can be used as a polarization-selective delay line. Measured bandwidth of the multi-slot waveguide is (1530nm - 1590nm) ~7.4THz. Therefore, the DBP can be calculated as

$$DBP = \Delta t \Delta f = \frac{\Delta n_g L}{c} \Delta f \cong 40/mm.$$

Achieving delay-bandwidth product of 3000, 2 orders of magnitude larger that current slow light schemes as shown in Figure 4-12, would require a multi-slot waveguide of approximately 7.5cm long. Although vertical multi-slot waveguides of this length have not yet been fabricated, horizontal triple-slot waveguides up to 1.5 cm length have been demonstrated[64].

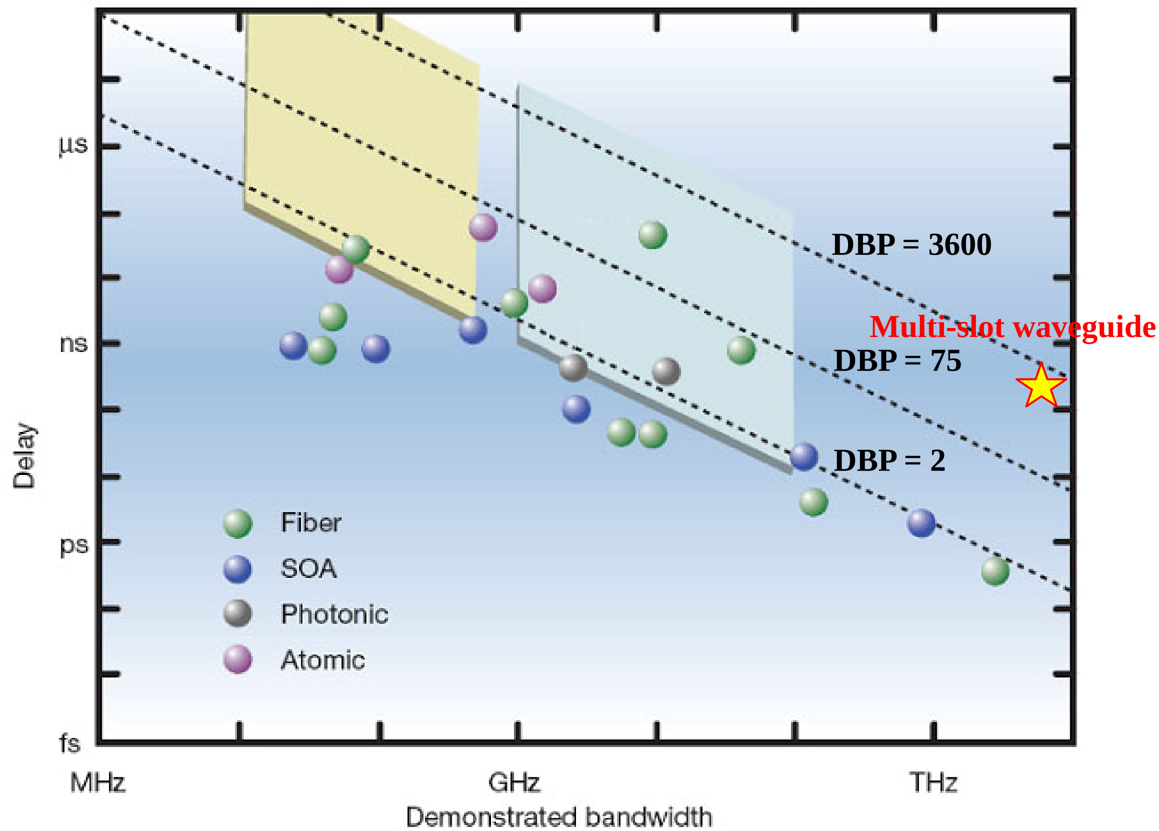

Figure 4-12. Comparison of DBP of multi-slot waveguide with different schemes. (Figure courtesy: Parra *et al*, Optics and Photonics News, 18, 40, 2007)

4.2. Mode Profile shaping

As shown in the simulations (Figures 2-8 and 2-9), the TE and TM modes have very different profiles in the near field. Direct butt-coupling to other optical elements with small numerical apertures (typical for on-chip components as well as off-chip detectors and couplers) would create a large polarization-dependent loss. However, since in both polarizations the peak field amplitudes in the high-index regions follow the supermode progression, as described earlier (i.e., $C_n^0 = \left(\frac{1}{2}, \frac{\sqrt{3}}{2}, 1, \frac{\sqrt{3}}{2}, \frac{1}{2}\right)$), it should be possible to create an imaging system to shape the modes as to achieve near-identical coupling to an external detector, fiber coupler, or optical element.

The main function of a beam-shaping optic is to cut-off high spatial frequencies (the number of periodic spacing per unit interval), and it may be designed for either on-chip or off-chip integration. Provided that the cut-off frequency is sufficiently high, the measurement can also be used to verify that the higher-order TE_1 mode was not excited in the waveguide as was suggested by Figure 4-10 where the theoretically-predicted indices are similar for the TM_0 and TM_1 modes. For convenience, the off-chip design was used, which allowed for the accurate measurement of the resulting profiles using a scanning knife-edge method.

4.2.1. Knife-edge measurement

To demonstrate the high-frequency filtering of the near-field by a diffraction limited optical transfer function, a knife-edge method[65] was used to record the spatial distribution of the field. The output facet of the chip was imaged using a Mitutoyo ULWD SL100 objective (focal length f =2 mm, N.A. = 0.55) and a Navitar UltraPreciseEye 2x tube (total magnification = 181x) onto a highly-sensitive InGaAs photoreceiver (New Focus Femtowatt 2153). Alternatively, the cleaved facet of the chip could be imaged using an NIR camera (Xenics XEVA-1.7- 320TE). The magnification was chosen so that the field of view at the detector images a single waveguide, but not its neighbors. The exit aperture after the objective and tube lens is 0.5*mm* and the distance between the exit aperture and image plane is 2.5cm, thus creating an optical transfer function (OTF: represents the ratio of image contrast to specimen contrast when plotted as a function of spatial frequency) at the image plane which filters out spatial frequencies greater than 65cm^{-1}. Input power levels from the laser were made less than 50μW so as not to saturate the detector. Since the knife-edge is scanned while keeping the laser at a fixed wavelength (1550nm), there was no effect of chromatic abberations in our mode-profile measurement scheme. The laser source was modulated at 641Hz (less than the bandwidth of the photoreceiver), and the photoreceiver output was measured by a lock-in amplifier (Stanford Research Systems SR830). As the knife edge was scanned across the field-of-view at a constant speed (using a Newport ILS200 translation stage and ESP300 motion controller), the resultant trace was recorded. The knife-edge scan achieves 1μm resolution, compared to the 200μm width of the magnified image of the end-facet. Figure 4-13 schematically illustrates the experimental setup and Figure 4-14 shows the image of the waveguide mode taken by NIR camera.

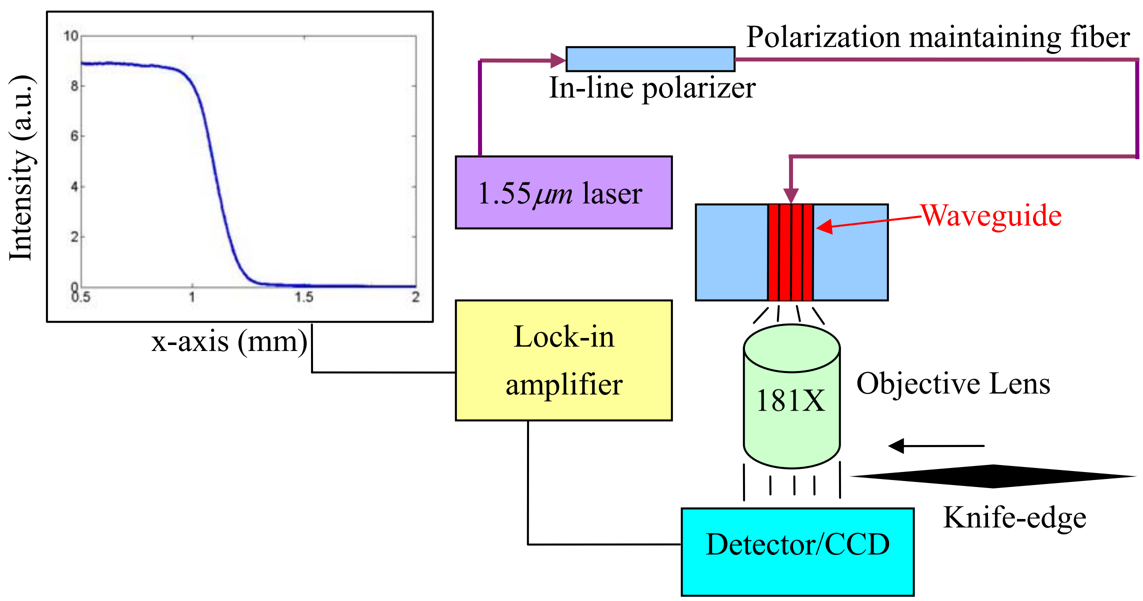

Figure 4-13. Schematic illustration of the knife-edge measurement setup.

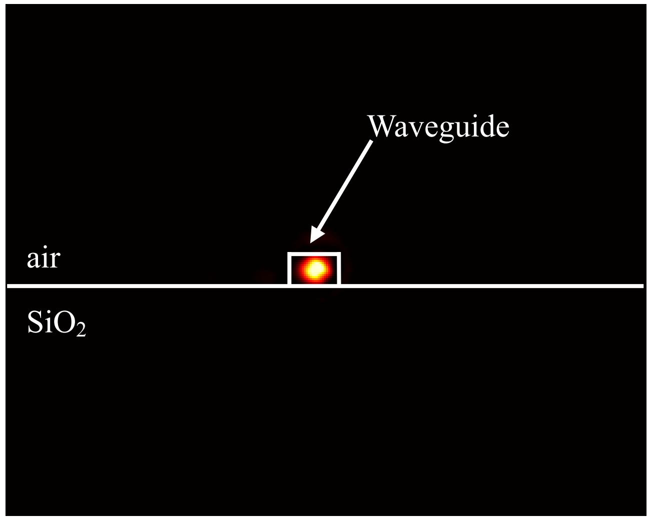

Figure 4-14. The CCD image of the waveguide mode with the waveguide and substrate superposed onto the image. A 1.55μm laser was coupled into the multi-slot waveguide.

4.2.2. Results

The recorded data were averages of eight traces for each polarization (see Figure 4-15), at the wavelength λ= 1550*nm*. Field profiles were obtained from the scanning traces by differentiation and filtering out the high-frequency components which had spatial frequencies greater than 200 cm^{-1}(more than 3 times the cut-off frequency of the OTF), attributing these high-frequency components to random deviations from linearity in the mechanical movement of the translation stage. Simulation of mode profiles after shaping were also implemented by taking near field mode profiles calculated using the FDFD method and filtering out the high-frequency components which had spatial frequencies greater than 65cm^{-1} at the image plane. When superposing the measured mode profiles (red dots) onto simulated mode profiles (black solid line), there is very good agreement between simulations and experiments (see Figure 4-16).

Comparison between the measured TE and TM mode profiles is shown in Figure

4-17. It was seen that there is not much difference between the two modes in terms of external coupling.

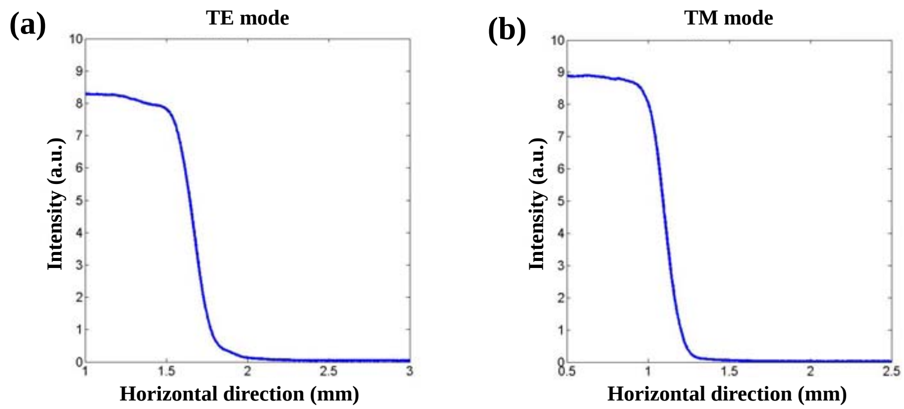

Figure 4-15. Knife-edge scanning traces for the TE and TM modes.

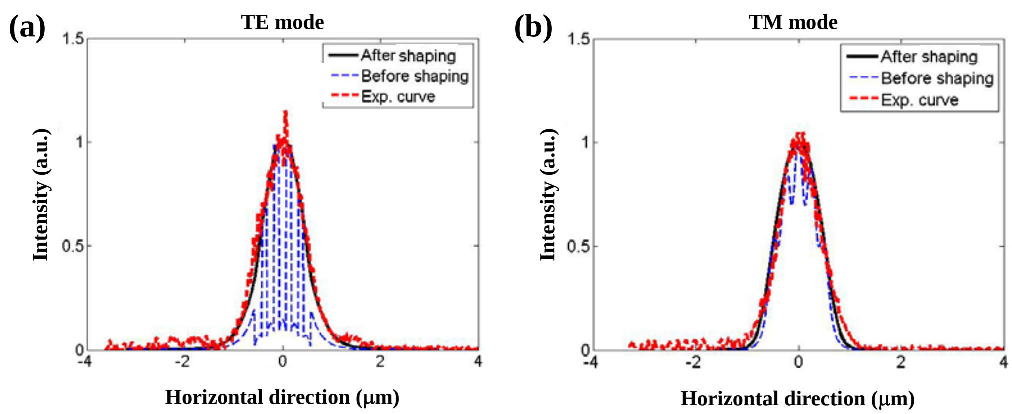

Figure 4-16. Comparisons between measured and simulated mode profiles. Near field mode profiles are also shown in dotted blue line. Good agreement between experiment (red dots) and simulation (black solid line) was observed.

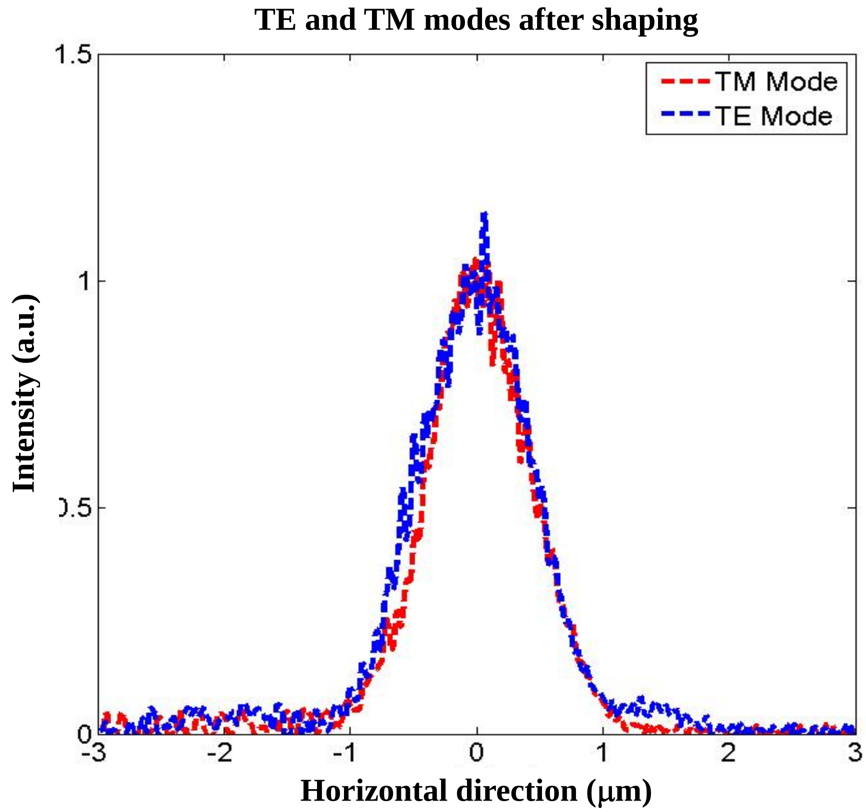

Figure 4-17. Comparison of measured mode profiles between the TE and TM modes. It is seen that the two modes are almost identical. Hence, the high frequency components were successfully filtered out.

4.2.3. Absence of the higher-order TM_1 modes

The center-to-center distance between the two intensity peaks of the TM_1 mode is about 0.65 μm in simulations, which is less than the Abbe resolution limit (=λ/2N.A.) for two point sources at a wavelength of $\lambda = 1.55\mu m$. However, the two lobes of this mode are in phase opposition (exactly π out of phase with regard to each other), and under these conditions, the diffraction-limited image (post OTF-filtering at the image plane) should show a dip at the center[66] (see Figure 4-18(a)). Such a pattern was not observed in the measurements as shown in Figure 4-16. It is concluded that, as expected from the symmetry of the field in the launching waveguide, the TM_1 mode was not excited in the multi-slotted waveguide. Higher order TM_2 and TM_3 mode profiles after shaping were also simulated for comparison in Figure 4-18.

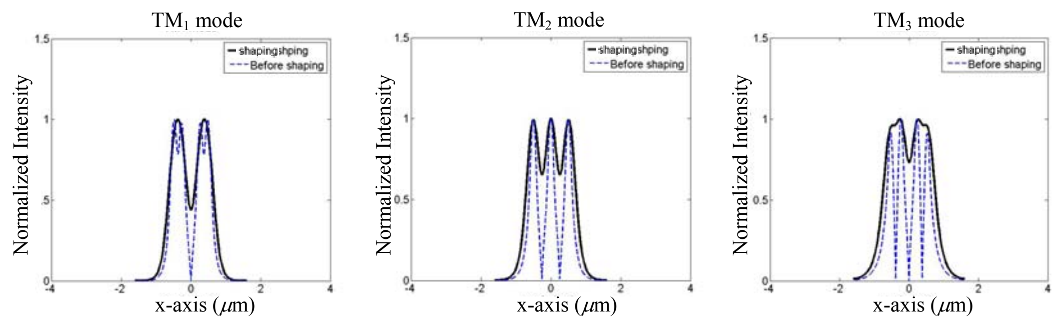

Figure 4-18. Simulation of (a) TM_1 (b) TM_2 and (3) TM_3 modes after mode shaping. It is seen that for the TM_1 mode, there is a dip at the center which was not found in the measurement. Dips also appear in the TM_2 and TM_3 modes. Therefore, the higher order mode was not being excited during the experiments.

4.3. Loss in the multi-slot waveguide

Loss measurements were performed on strip waveguides (without slots) and multi-slot waveguides. They were implemented by monitoring the output power on waveguides of different length. By measuring the output power, a total loss can be calculated thorugh

$$\alpha_{total} = \alpha_{coupling} + \alpha_{waveguide} \times L_i = 10\log_{10}\frac{I_i}{I_o} \tag{4-6}$$

where α_{total} is the total loss (*dB*), $\alpha_{coupling}$ is the coupling loss (*dB*), $\alpha_{waveguide}$ is the waveguide loss (*dB/cm*), L_i is the waveguide length (*cm*), I_0 is the input power (*W*) and I_i the detected power (*W*). Under similar coupling, the total loss difference between two waveguides of different length (L_1 and L_2) is,

$$\alpha^1_{total} - \alpha^2_{total} = \alpha_{coupling} + \alpha_{waveguide} \times L_1 - \alpha_{coupling} + \alpha_{waveguide} \times L_2 = 10\log_{10}\frac{I_1}{I_2}. \tag{4-7}$$

The waveguide loss was then calculated by,

$$\alpha_{waveguide} = \frac{\alpha_{total}^{1} - \alpha_{total}^{2}}{L_1 - L_2} = \frac{d\alpha_{total}}{dL} = \frac{10\log_{10}\frac{I_1}{I_2}}{L_1 - L_2} \tag{4-8}$$

The total loss of the strip waveguides (at $1.55\mu m$) (see Figure 4-19) was measured and plotted in Figure 4-20. From the linear best fit, the strip waveguide loss ($d\alpha_{total}/dL$) was calculated to be ~ -14.6*dB/cm* for the TE mode and ~ -13.4*dB/cm* for the TM mode.

Two chips with six multi-slot waveguides of different lengths (see Figure 4-21) were also fabricated for the loss measurement. The measured power is listed in table (4-1) and the loss was calculated to be ~ -80*dB/cm* for both the TE and TM modes.

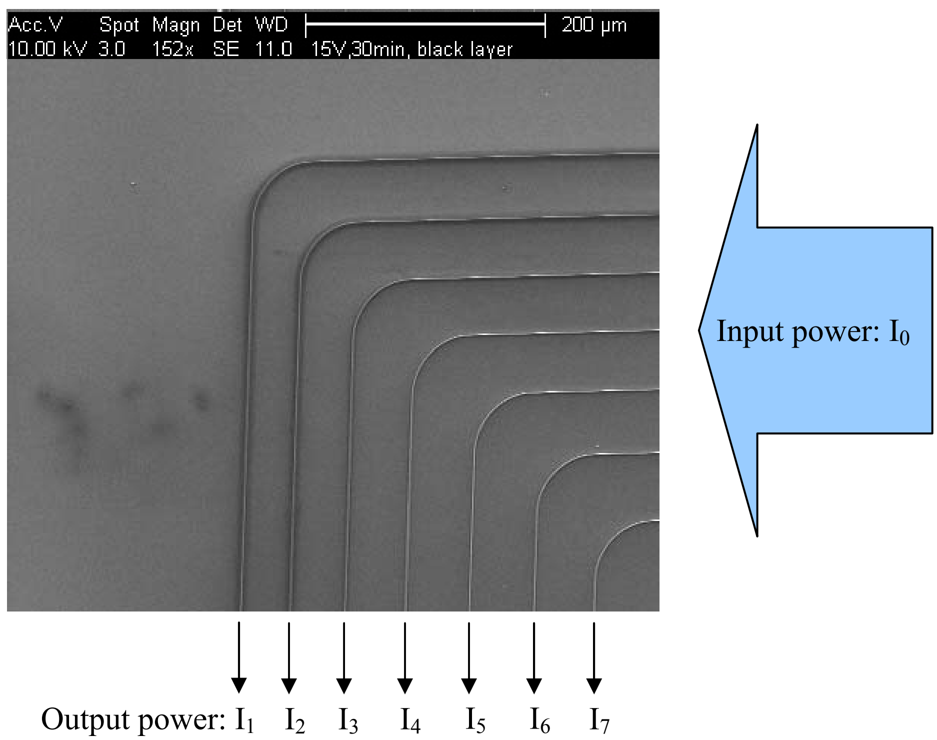

Figure 4-19. Scanning electron microscope (SEM) of strip waveguides used for loss measurement. By monitoring the output power at the end of the waveguide, the loss of the fabricated device can be extract.

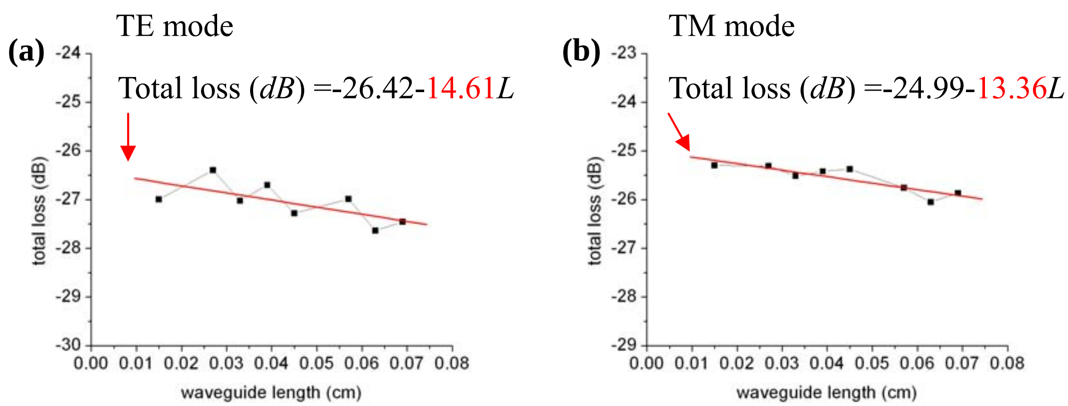

Figure 4-20. The measured total loss versus strip waveguide length for the (a) TE and (b) TM modes. The red curve is the best linear fit and it yields the waveguide loss. For the TE mode, the loss was -14.61*dB/cm*. For TM mode, the loss was -13.4*dB/cm*.

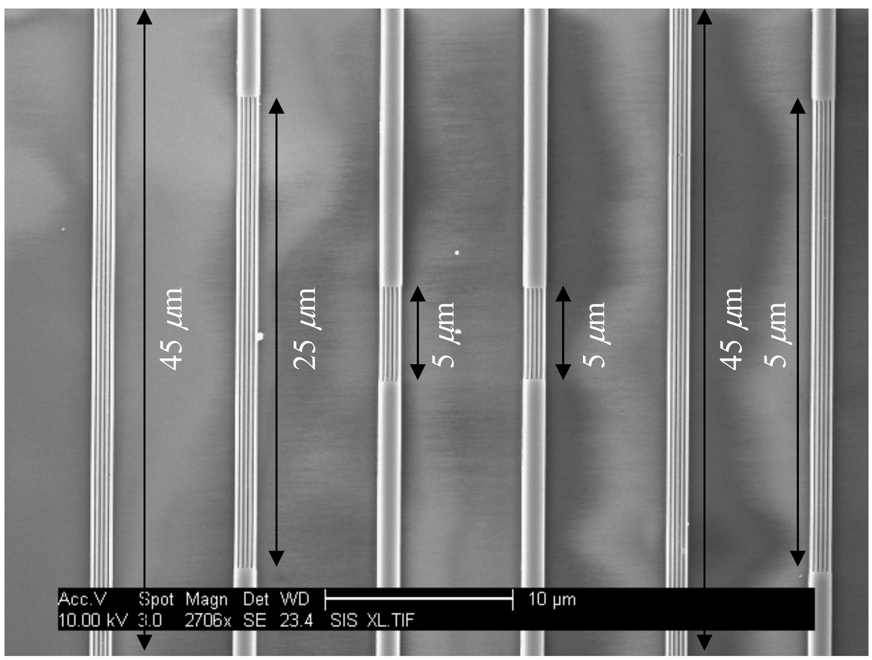

Figure 4-21. Scanning electron microscope (SEM) image of the multi-slot waveguides with different lengths. The length of these six waveguides are 45, 25, 5, 5, 45, 25 μm respectively, from left to right.

Table 4-1. Measured power of multi-slot waveguide with 10*mW* input.

		Device length (μm)	45	25	5	5	45	25
Measured power (μW)	TE mode	Chip 1			3.071	2.512	1.476	1.471
		Chip 2	2.545	2.561	3.307	3.871		2.573
	TM mode	Chip 1			6.179	5.871	5.468	5.518
		Chip 2	4.907	4.860	6.021	6.219		4.977

4.4. Conclusion

A large birefringence (the group index difference, Δn_g, between the TE and TM modes) was observed in multi-slot waveguide. The Δn_g of ~1.6 over more than 60 *nm* bandwidth at wavelengths of importance in telecommunications (λ= 1530 to1590 *nm*), was successfully measured through FSR analysis. Experimental results agreed very well with simulations. Such large birefringence could be utilized for compact chip-scale optical delay line applications. The DBP of multi-slot waveguides was estimated to be ~3000 for a with a 7.5 *cm* long device, about two orders of magnitude larger than current slow light based schemes.

Mode shaping tools were also designed for reducing polarization dependent coupling loss. Knife-edge scan techniques were performed to measure the mode profile of the TE and TM modes after shaping, and results confirmed that high spatial frequency modulations of the TE and TM modes were successfully filtered. The loss of multi-slot waveguides was measured to be ~-80*dB/cm* for both TE and TM modes.

This chapter, in part, have been published as "Giant birefringence in multi-slotted silicon nanophotonic waveguides" by S. H. Yang, M. L. Cooper, P. R. Bandaru and S. Mookherjea, Optics Express, Vol. 16, 8306 (2008).

Chapter 5: Summary and future work

In summary, the characteristics of silicon on insulator (SOI) based multi-slot waveguides have been studied. The optimal design of multi-slot waveguides was investigated for maximizing the birefringence (Δn_g) through EMT analysis and FDFD simulations and shows potential for optical delay line applications.

The multi-slot waveguides were fabricated using CMOS compatible processes for chip-scale integration. A large birefringence (Δn_g~1.6), over wavelengths of importance in telecommunications (λ= 1530~1590 *nm*), was successfully demonstrated through FSR analysis, using the Fabry-Perot resonator technique, and is the **largest value** ever reported (*nearly twice as large as previously achieved*). Experimental results showed good agreement with simulations. Such large birefringence could be utilized for compact, chip-scale optical delay line applications.

Mode shaping tools were designed for reducing polarization dependent coupling loss. Knife-edge scan techniques were performed and confirmed similar mode profiles for the TE and TM modes after profiling. High spatial frequency modulations of the TE and TM modes were successfully filtered.

The potential applications of the multi-slot waveguide in optical delay lines are promising. Figure 5-1 illustrates a proposed polarization sensitive, integrated multi-slot waveguide delay line which includes a polarization switch. Following the polarization switch is a multi-slot waveguide which can delay the input signal, depending on the signal's polarization state.

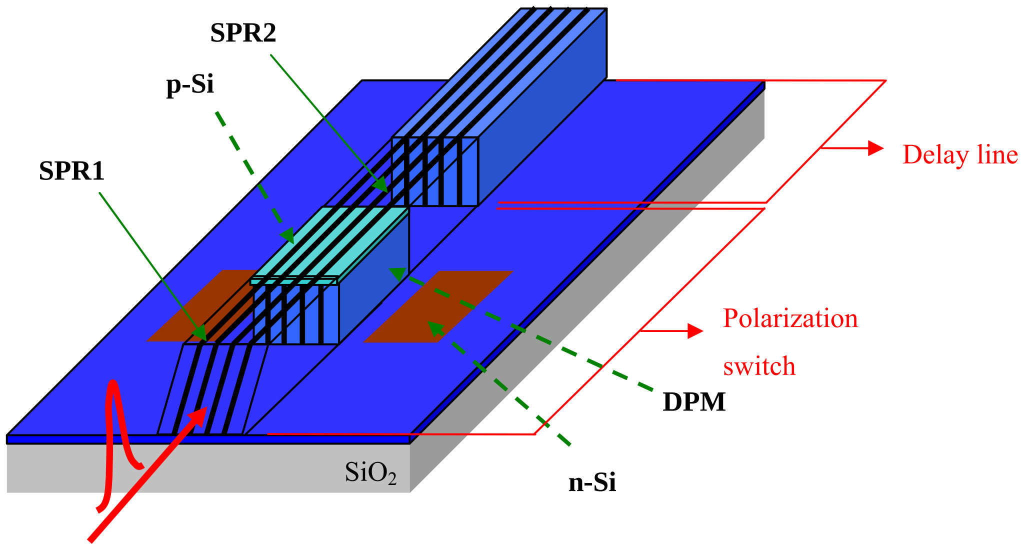

Figure 5-1. A schematic of an on-chip delay line system. It includes a polarization switch to set the polarization state of incident light followed by a multi-slot waveguide delay line.

5.1. Polarization switch

The polarization switch consists of a dynamic phase modulator (DPM) sandwiched by two static polarization rotators (SPR). The first SPR rotates the linearly polarized EM waves (TE or TM mode) clockwise by 45˚, followed by a DPM which is used to further rotate the modes by 90˚ or 0˚, using phase modulation to convert/preserve the incident polarization. The second SPR further rotates the polarization by 45˚ counterclockwise and nullifies the rotation of the first SPR. Therefore, the initial polarization will either rotated by 90˚ (which implies mode conversion, TM→TE or TE→TM), or 0˚ (where the output mode is unchanged from the input polarization, TM→TM or TE→TE).

5.1.1. Static polarization rotator 1

An SPR is fabricated through a form birefringent multi-layered structure orientated at 22.5° with respect to the normal of the substrate. In this multi-layer structure, the direction transverse to the layers is defined as the principal axis while the direction normal to the layers is the secondary axis, as shown in Figure 5-2. The propagating EM waves have different group indices ($n_g^{Principal}$ and $n_g^{Secondary}$) along these axes. (In SPR, the electric field of the TM/TE modes are oriented at 22.5° with respect to the principal/secondary axes.

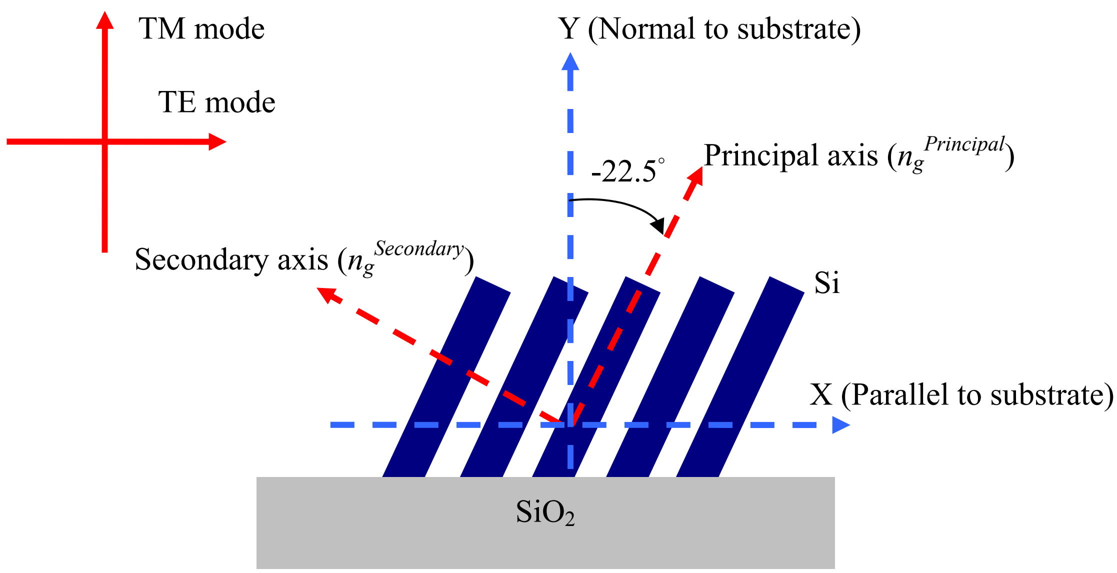

Figure 5-2. Schematic of the static polarization rotator (SPR) on an SOI platform. The layered structure is fabricated 22.5° with respect to the normal. The input light has different group indices when its electric field is aligned with principal or secondary axes. (The polarization is defined as TE if the electric field is parallel to the substrate and is defined as TM if the electrical field is normal to the substrate.)

When linearly polarized light (TM or TE) is coupled into the SPR, it can be analyzed as two linearly polarized EM waves, one oriented along the principal axis and another along the secondary axis. On propagation through the structure, these two components acquire a phase shift, θ, which depends on the length of the SPR (d) and is given by

$$\theta = \frac{2\pi \left| n_g^{principal} - n_g^{secondary} \right| d}{\lambda} \tag{5-1}$$

where $n_g^{principal}$ and $n_g^{secondary}$ are group indices of EM waves with electric fields aligned to the principal and secondary axes. Then, the length of the SPR to introduce π phase shift between the two components is

$$d = \frac{\lambda \pi}{2\pi \left| n_g^{principal} - n_g^{secondary} \right|} = \frac{\lambda}{2\Delta n_g^{SPR}} \tag{5-2}$$

The π phase shift rotates the electric field by 45° clockwise, as shown in Figure 5-3.

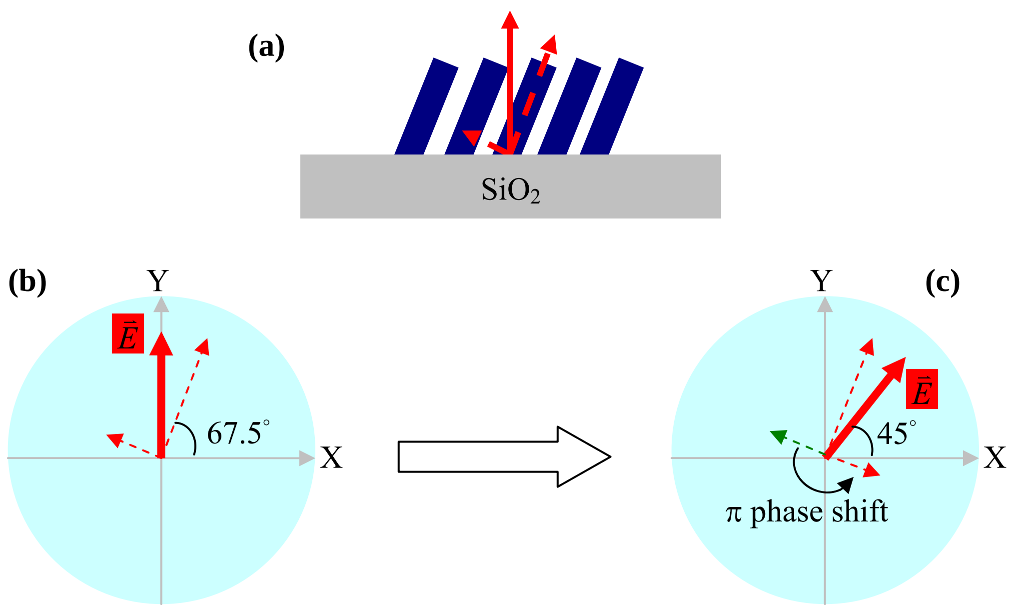

Figure 5-3. (a) Schematic of a SPR (b) The incident EM wave (TM mode, for example) is analyzed in two components aligned to the principal and secondary axes. (c) The SPR introduce a π phase shift between the two components, resulting in 45° rotation of the polarization.

5.1.2. Dynamic phase modulator

A dynamic phase modulator (DPM) can be fabricated using multi-slot waveguides incorporate a p-i-n junction, and is illustrated schematically in Figure 5-4(a). The p-i-n junction can be used for carrier injection to modulate the refractive index, and consequently, the group index difference and phase.

When a 45° oriented EM wave (after the first SPR, Figure 5-3(c)) is coupled into the DPM, it could be decomposed into two components orientated along the principal and secondary axes of the DPM. A phase shift is introduced between these two components. When the phase shift is modulated to be π, the incident polarization will be rotated by 90° (see Figure 5-4(b)) and will be refereed to as the “ON” state. When the phase shift is 2π, the incident polarization is unchanged and will be referred as the “OFF” state. (see Figure 5-4).

Using equation (5-1), at “ON” state, the length required for a π phase shift is $d_1 = \frac{\lambda}{2\Delta n_{g1}^{DPM}}$ and in the “OFF” state, the length for a 2π phase shift in the DPM is $d_2 = \frac{\lambda}{\Delta n_{g2}^{DPM}}$. Hence, an adequate length (d_{DPM}) can be designed through:

$$d_{DPM} = ld_1 = md_2 \qquad (5\text{-}3)$$

where l is an odd integer and m any integer.

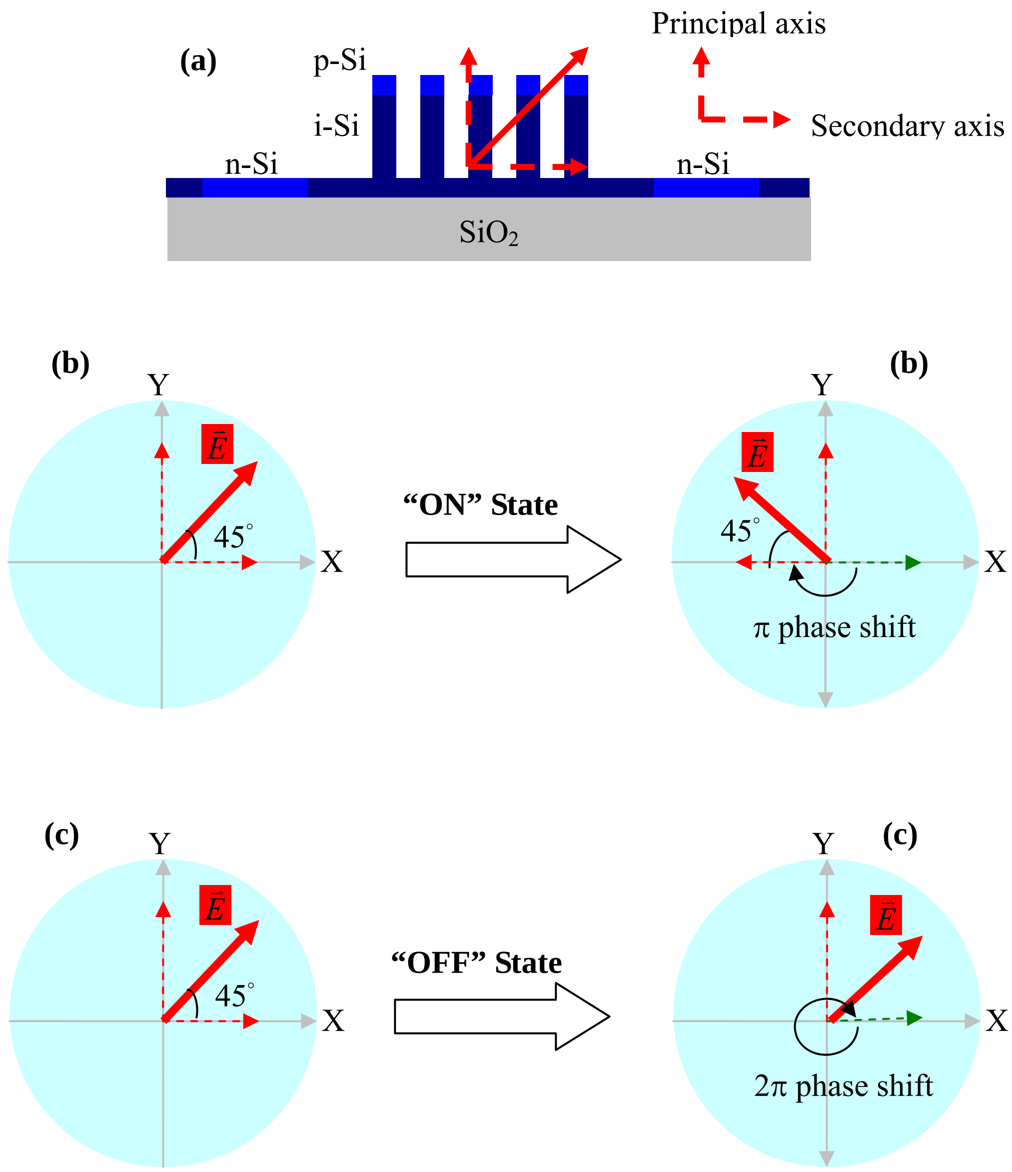

Figure 5-4. (a) Schematic of the DPM. The p-i-n junction is used to inject carriers into i-Si to modulate the effective refractive index, to modulate phase for phase modulation. (b) At "ON" state, the 45° linearly polarized light is decomposed into two components along the principal and secondary axes. A π phase shift is introduced into the two component and results in a 90° rotation of the polarization. (c) At "OFF" state, a 2π phase shift is introduced and no rotation of incident polarization is obtained

5.1.3. Static polarization rotator 2

A second SPR follows the DPM further rotates the incident polarization by 45°

counterclockwise to yield a TM or TE mode (Figure 5-5).

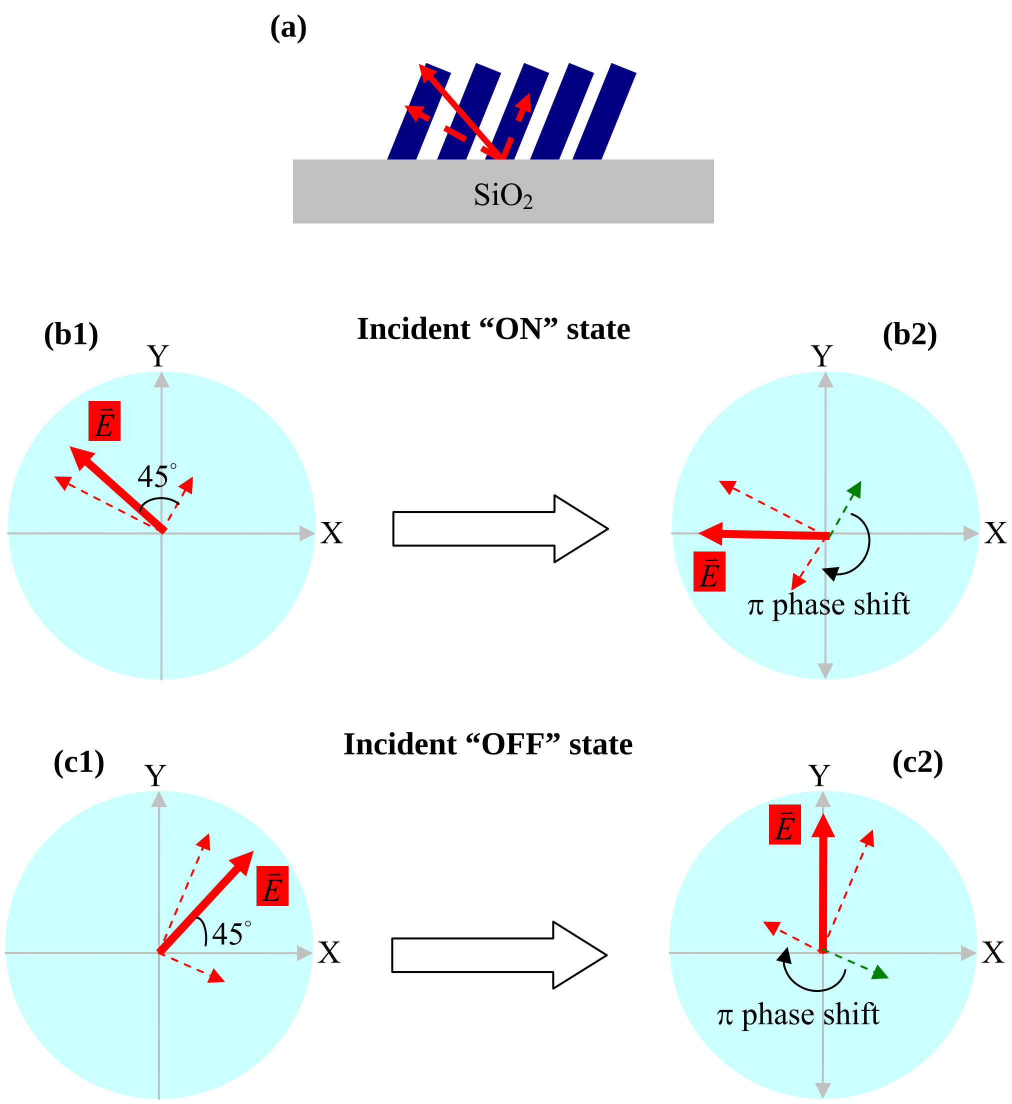

Figure 5-5. (a) Schematic of a SPR. (b) Incident "ON" state: Incident linearly polarized light is rotated by 45° and converted to a TE mode. (c) Incident "OFF" state: Incident linearly polarized light is rotated by 45° and converted to a TM mode.

Following the second SPR is a multi-slot waveguide with optimal/maximized birefringence. By controlling the polarization state in the polarization switch, the delay ($\Delta t = \frac{\Delta n_g L}{c}$) in the multi-slot waveguide can be controlled.

Appedix A. Characterization of the absorption properties of silicon

The optical properties of silicon relevant to waveguide operation are reviewed and characterized. While light propagates in silicon waveguide, bulk silicon absorption is also important. A large absorption loss degrades waveguide performance.

A.1. Absorption in Silicon

Silicon is a semiconductor material with an indirect bandgap[67] (as shown in Figure A-1). The transition of carriers from the valence band to the conduction band requires the presence of a photon and an absorbed/emitted phonon, with changes in energy and momentum. The absorption coefficient (α) can be written as[68]

$$\alpha = C\left(h\omega - E_g \pm E_p\right)^2 \qquad \text{(A-1)}$$

where C is a constant, E_g the bandgap energy (~1.1eV), E_p the phonon energy and $\hbar\omega$ the photon energy. When the photon energy is sub-bandgap, the absorption coefficient is small. By taking the square root of the absorption coefficient, equation (A-1) can be rewritten as

$$\sqrt{\alpha} = \sqrt{\mathrm{C}}\left(h\omega - E_g \pm E_p\right). \qquad \text{(A-2)}$$

It is seen that $\sqrt{\alpha}$ is linearly proportional to the photon energy. When plotting $\sqrt{\alpha}$ versus photon energy, the slope changes when the absorption process changes from phonon absorption ($+E_p$) to phonon emission ($-E_p$). This transition region in the plot is termed the “knee” as in Figure A-2.

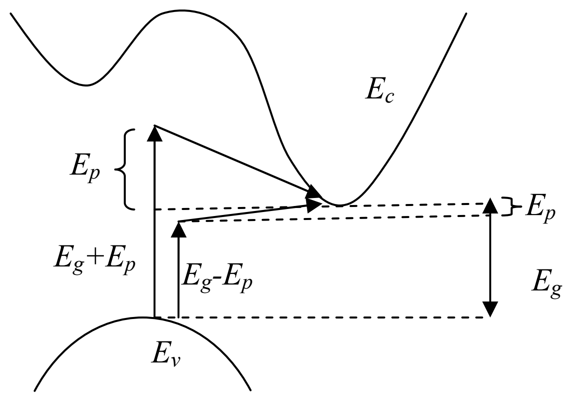

Figure A-1. Schematic illustration of the silicon band structure, with the transition of an electron due to phonon absorption/emission. E_c and E_v are energies of the conduction and valence bands. E_g is the bandgap energy.

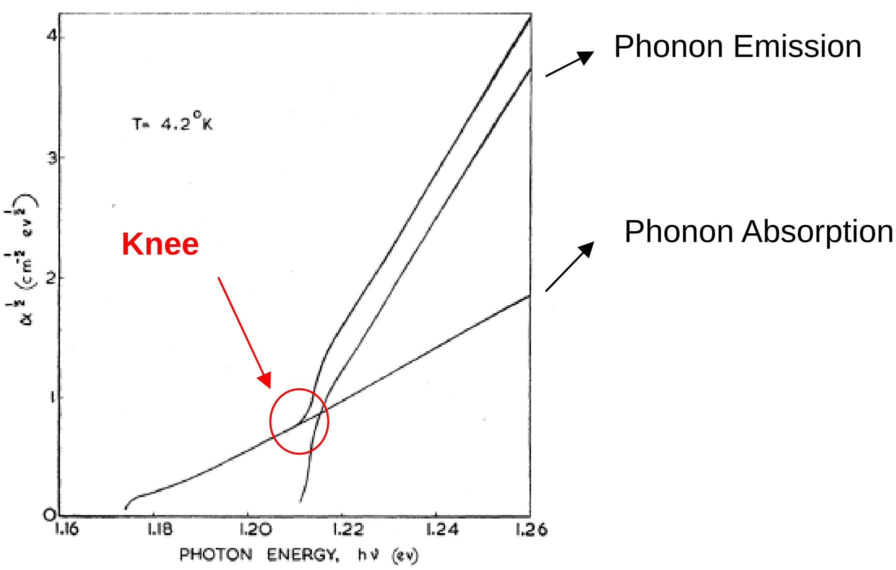

Figure A-2. A knee can be observed when the absorption mechanism changes from phonon absorption to phonon emission. (Figure courtesy: Macfarlane *et al*, Physical Review, 111, p.1245,1958, Fig.2)

Absorption coefficient is usually measured through monitoring the transmitted intensity (I_T) of light. For a given input power I_o, sample thickness d, and reflectivity R ($= \frac{(n_{sample} - n_{air})^2}{(n_{sample} + n_{air})^2}$, where n_{si}=3.48, n_{air}=1), the transmitted power ratio is given by[69]

$$I = \frac{I_t}{I_o} = \frac{(1-R)^2 \exp(-\alpha d)}{1 - R^2 \exp(-2\alpha d)}, \tag{A-3}$$

therefore, α is

$$\alpha = -\frac{\ln\left[-(1-R)^2 + \sqrt{(1-R)^4 + 4I^2R^2}\right] - \ln 2}{d} \tag{A-4}$$

A.2. Absorption coefficient measurement setup

A schematic of the absorption coefficient measurement setup is shown in Figure A-3. A halogen lamp serves as a broad band light source (500*nm*~2000*nm*). The resolution of the monochromator (Oriel Cornerstone 130: Melles Griot) is ~7.9*nm*. The light that exits the monochromator first passes through a collimating lens. Subsequently, the light is separated into two equal intensity beams using a non-polarizing beam splitter (BS1). One beam passes through the sample, while the other serves as a reference beam. These two beams are chopped, using an optical chopper at two different frequencies. These two beams then recombine at a second beam splitter (BS2) and are collected by a photo-detector. The signal from the photo-detector is then fed into two lock-in amplifiers which lock/synchronize the signal to the two different frequencies of the sample and reference beams. Figure A-4 shows the actual setup.

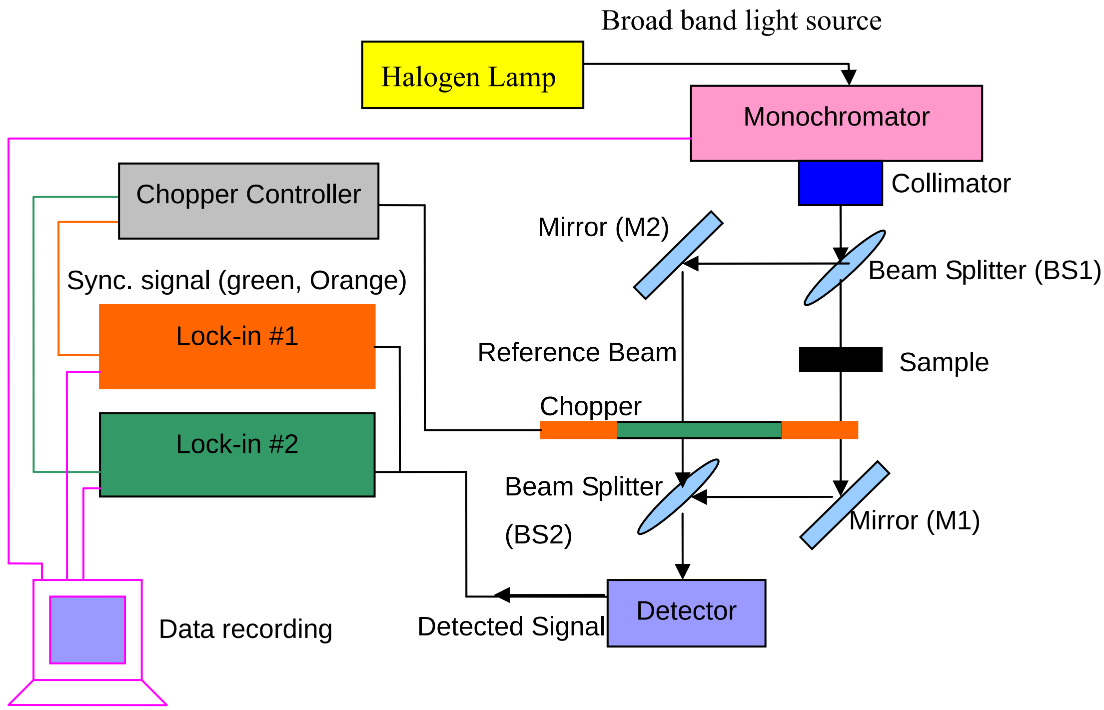

Figure A-3. Schematic of absorption coefficient measurement.

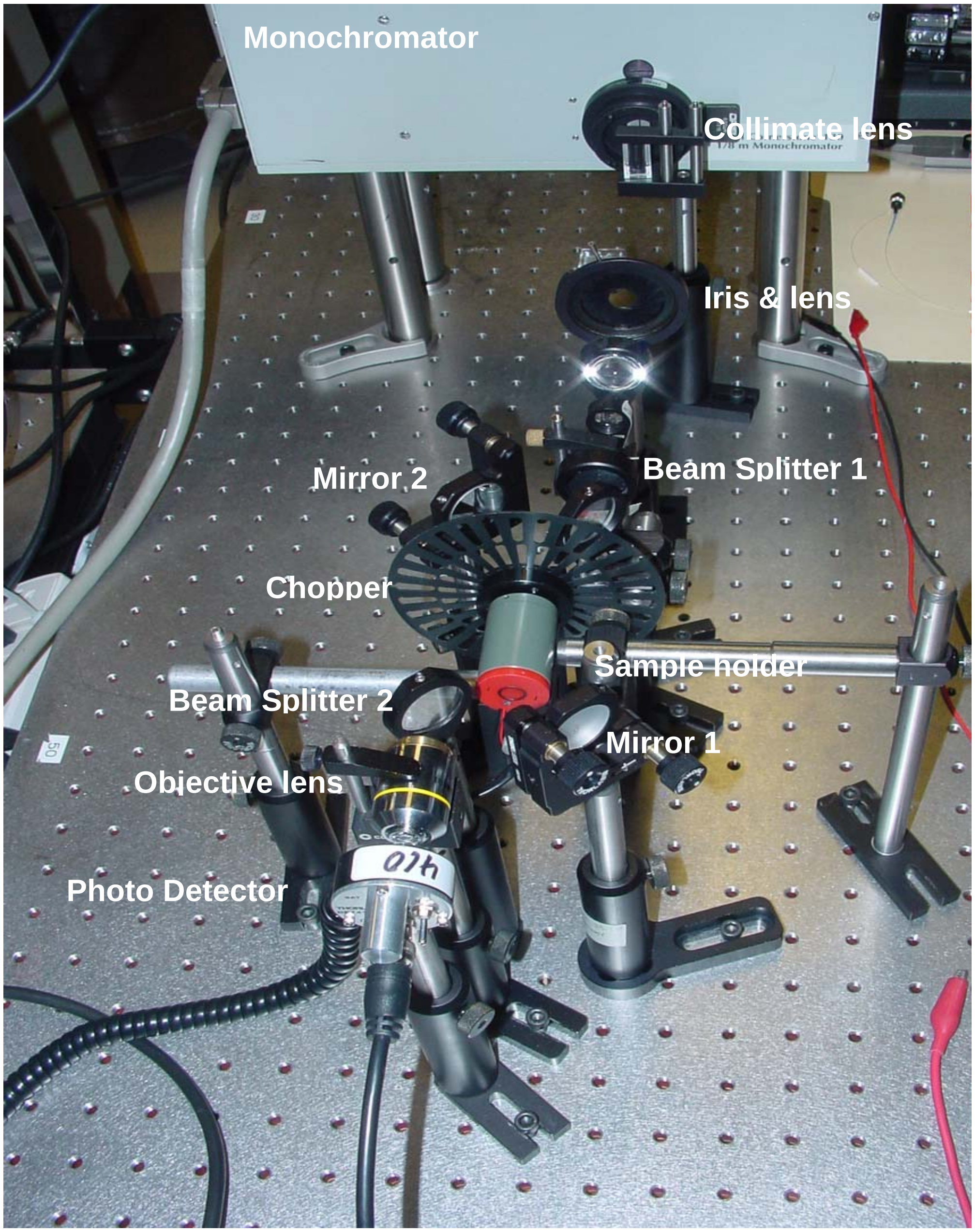

Figure A-4. The setup for the absorption spectra measurement.

In order to obtain the transmission ratio, data without the sample is taken first as a reference. The sample is then placed and the measurement repeated.

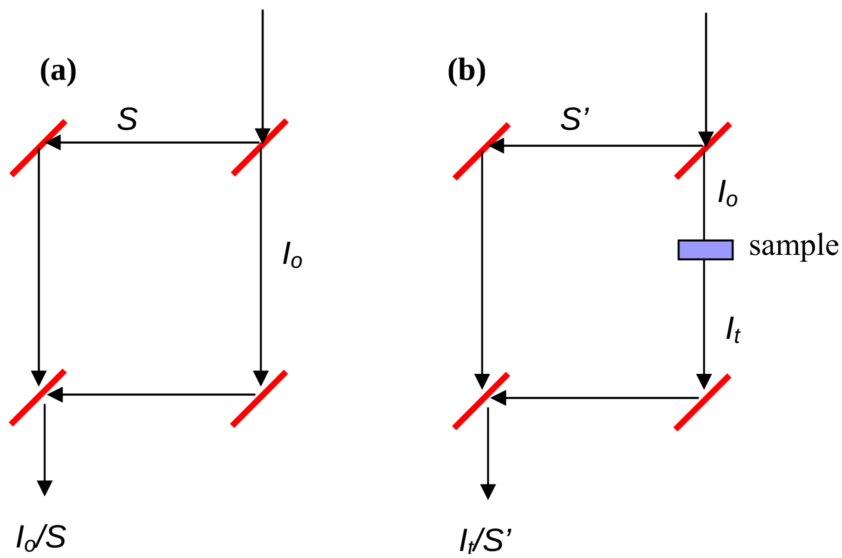

Figure A-5. Schematic of experimental setup (a) without (b) with the sample. Taking the ratio of two data sets, the transmission ratio can be calculated.

Recorded data with and without sample are $\frac{I_o}{S}$ and $\frac{I_t}{S'}$ respectively as shown in Figure A-5. By taking the ratio of the two measurements, the transmission ratio (I_t/I_o) can be obtained and the absorption coefficient is then calculated through equation (A-4).

A.2.1. Measurement results

The transmission spectrum of a lightly doped silicon sample (1*Ω-cm*) was measured. Using equation (A-4), the absorption spectrum was calculated and is shown in Figure A-6. When the photon energy is greater than the bandgap (region A), the absorption is strong and while when the photon energy is sub-bandgap (region B), the absorption is lower.

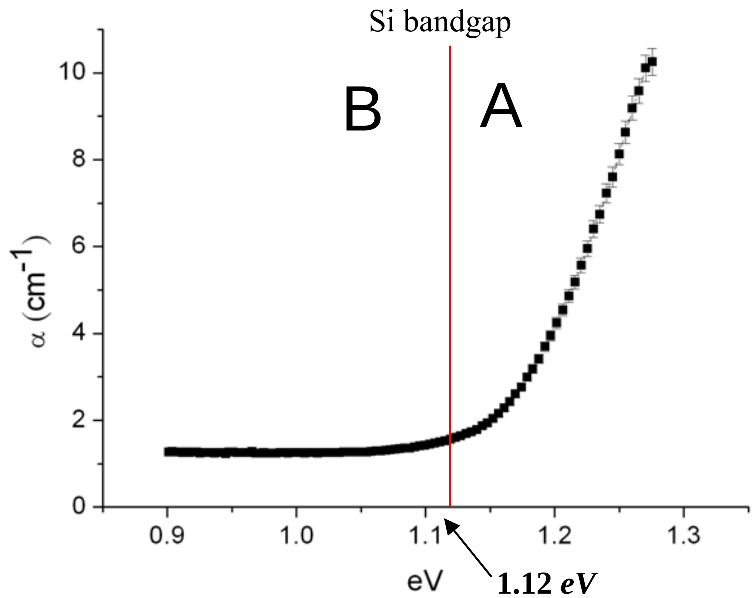

Figure A-6. Absorption spectrum of silicon sample.

The $\sqrt{\alpha}$ versus photon energy is plotted in Figure A-7. The $\sqrt{\alpha}$ varies linearly with photon energy and changes its slope when the absorption process changes from phonon absorption to emission as mentioned in section A.1. However, the knee was not well defined, possibly due to the resolution of the monochromator.

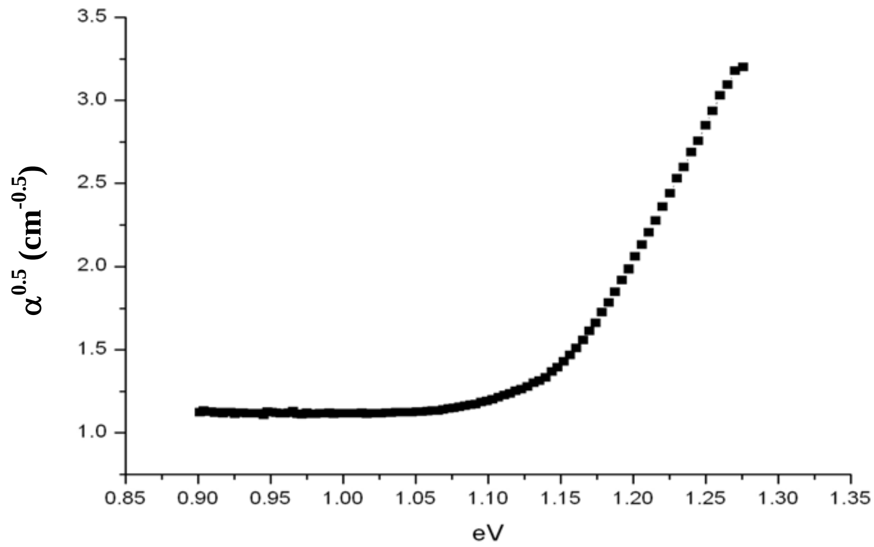

Figure A-7. The $\sqrt{\alpha}$ versus photon energy. In this curve, the "knee" is not well defined.

The $d\sqrt{\alpha}/d(eV)$ (slope) is plotted in Figure A-8. The slope is seen to have changes at 1.047 *eV*, 1.135 *eV* and 1.187 *eV*.

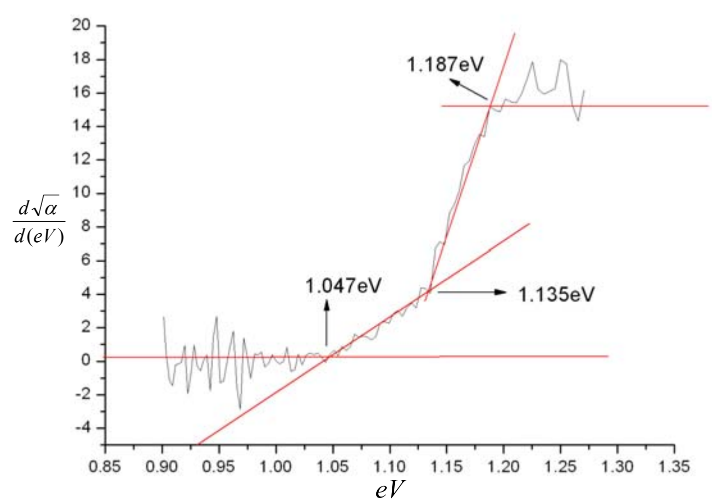

Figure A-8. The slope of square root of $d\sqrt{\alpha}/d(eV)$. Sudden change in slope indicates the involved phonon energy change due to interaction with phonon.

Accordingly, Figure A-8 was separated into four segments and fit individually (shown in figure A-9). The intersection of these best linear fit and the x-axis is called threshold energies. However, measured threshold energy did not agree with the literature and it was probably due to the doping of the silicon. In doped silicon, free carrier absorption of photons is involved and hence increases the α. When photon energy is lower than the bandgap, the absorption from free carrier absorption dominates. Therefore, the band to band transition is relatively weak and hence, phonon interaction is hard to observe. Table A-1 lists the knee values and threshold energies for comparison.

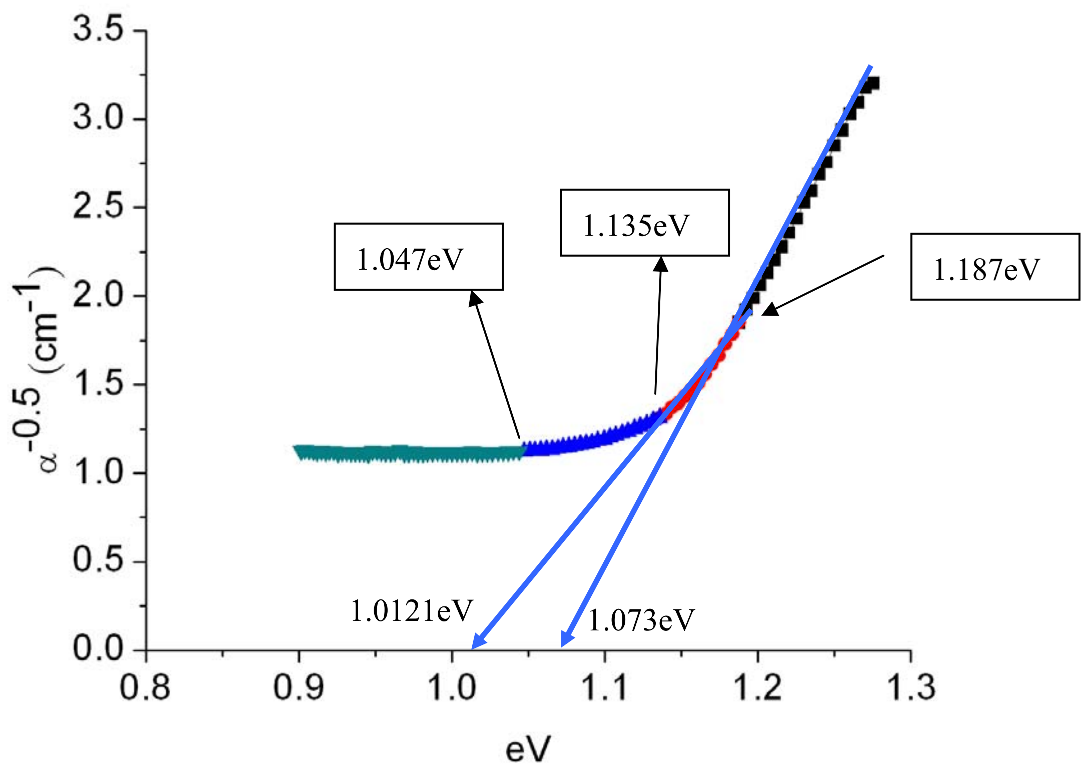

Figure A-9. Figure A-8 is separated into four segments according to the knee values. The threshold energies are shown in figure.

Table A-1. Comparison of the knee values with literature. Interacting phonon is also listed. The first knee was due to the phonon absorption. When photon energy was greater than bandgap energy, phonon was emitted which is represented by the second knee. When photon energy is even higher, the transition emits phonon with higher energy and is represented by third knee. Good agreement between reported knee values and measured results confirmed the accuracy of the equipment setup.

Interacting phonon[69, 70] (eV)	0.052	0.012	0.052
Phonon absorption/emission	absorption	emission	emission
Knee values[69] (eV)	1.051	1.135	1.169
Measured knee values (eV)	1.047	1.135	1.187

A.3. Absorption coefficient versus temperature and doping

As the temperature increases, the energy bandgap (E_g) decreases. The relation is given by,[68]

$$E_g(T) = E_g(0) - \frac{7.021\times10^{-4}T^2}{(1108+T)} \quad \text{(A-5)}$$

T is temperature in degrees *K*. The absorption then shifts to lower energy (red shift) when the temperature increases. The results of the measurement on silicon at different temperatures are shown in Figure A-10.

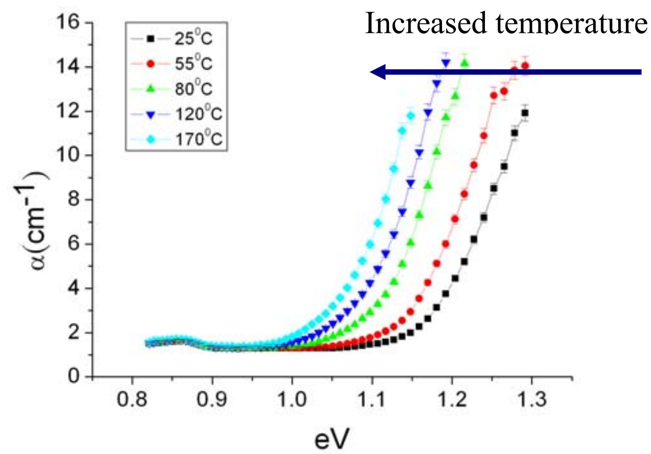

Figure A-10. The absorption spectra versus photon energy for Si at different temperatures. An increased temperature shifts absorption to lower energies.

When the doping level in silicon is increased, the α increases due to the free carrier absorption[71]. Therefore, low resistivity (highly doped) silicon is generally not preferred for waveguide fabrication. The absorption spectra for silicon of different resistivities are shown in Figure A-11. With resistivity below 0.005*Ω-cm*, the measured signal seems to be noise limited.

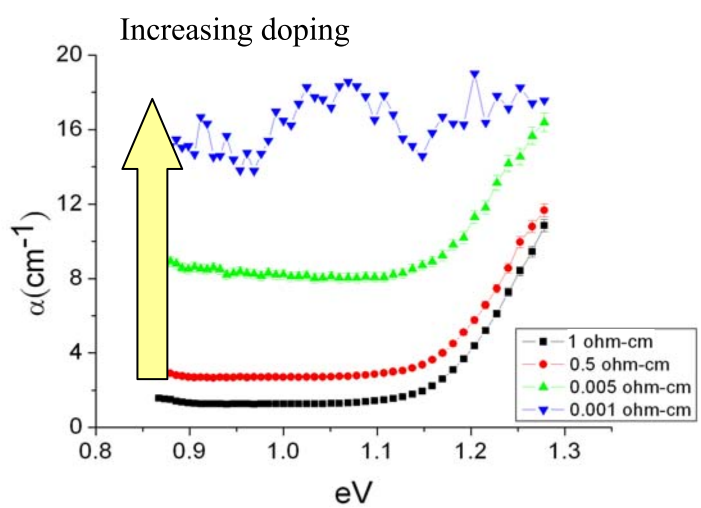

Figure A-11. The lower the resistance (higher doping level), the higher the absorption due to free carrier absorption.

A.4. Loss in silicon

While the absorption coefficient is measured, the loss to absorption can be expressed in *dB/cm* and is given by,

$$\alpha_{dB} = \frac{10\log\left(e^{-\alpha L}\right)}{L} \tag{A-6}$$

where L is the device length (*cm*). The measured absorption coefficient (α) is 1.1 cm^{-1} at 1.33μm (0.92*eV*), as seen in Figure A-6. Using equation (A-6), the absorption loss of a 1*cm* long waveguide made by 1*Ω-cm* silicon is calculated to be ~4.7*dB/cm*. It is large compare to the ~1 *dB/cm* loss (scattering loss due to side wall roughness) of currently fabricated low loss waveguides[72]. It is concluded that silicon with 1*Ω-cm* resistivity is not suitable for waveguide fabrication.

According to Figure A-11, it is observed that the absorption coefficient of silicon decreases with increasing resistivity. Therefore, in order to reduce the loss in waveguide, high resistivity (lower doping level) silicon is required. Low absorption coefficient of <0.1 cm^{-1} in silicon with resistivity about 10*Ω-cm* was reported[71] and the loss can be <0.4*dB/cm*, therefore, silicon with resistivity ~10*Ω-cm* is recommended.

A.5. Summary

The absorption properties of silicon were investigated by measuring the transmission ratio, using a Mach-Zehnder type setup. The absorption coefficient (α) under different temperatures and doping levels was measured. A shift of α to lower energies was observed with increasing temperatures while α decreased with reduced resistivity. For waveguide application, silicon with resistivity greater than 10*Ω-cm* is recommended.

Appedix B. RIE study using BCl_3 plasma

Reactive ion etching is very important fabrication process in semiconductor industry. Hence, further investigations on the mechanism of RIE of GaP is presented. While Si etching has been relatively well covered, and many references can be found. Therefore, GaP has been studied. The basic physical mechanisms are similar.

GaP is a promising material for optoelectronic devices in the visible range of electromagnetic radiation, due to its band gap of ~2.3 *eV* (~550 *nm*), and has been adapted for photo-detectors[73], light emitting diodes[74, 75], lasers[76], and even for photonic crystal[77]. For device processing and fabrication, especially at the micro- and nano-scales, dry etching techniques are preferred over wet etching processes due to the advantages of anisotropic etch characteristics and high selectivity. While dry etching on GaP has been previously reported[78], there has been no systematic study on the effects of process variables such as chamber pressure, power, and gas flow rate, which we address here. We study specifically the RIE processes based on BCl_3 plasmas, under various conditions, and the concomitant effects on the surface roughness and quality and understand the mechanism of RIE. BCl_3 gas has been chosen for its ability to provide a smoother surface than elemental Cl_2, as B is known to help[79] in surface oxide removal. While BCl_3 reacts with the GaP surface forming volatile chemical products, Ar is used as a carrier gas to stabilize the plasma and Ar ions help in the physical removal of material from the surface.

B.1. Experiment

n-doped GaP (from University Wafers Inc., Si Doped, $\rho \sim 0.05 \Omega\text{-}cm$) was used for the RIE experiments. Prior to etching, the sample was ultrasonically cleaned in trichloroethylene, acetone, isopropanol, and deionized water with a dry nitrogen blow in between each clean. Etch masks were fabricated by spinning on electron-beam resist (4 wt.% 495K PMMA dissolved in chlorobenzene) onto the GaP sample and subsequently electron-beam lithography was used to pattern rectangular and circular patterns, in the range of 0.1–10μm. Ni metal was deposited by electron beam evaporation in the patterned areas and the PMMA removed in acetone. The whole clean and e-beam process is just as discuss in previous section. It is a standard fabrication process. The Ni metal lines/mesas serve as etch masks and delineate the etch profiles. The etching was performed at room temperature in a Trion RIE/ICP etching system (with a base pressure of <1mTorr) equipped with a 13.56MHz RF source, under various conditions of BCl_3 and Ar pressure, flow rate, and RF power. The etch rate was determined by a surface profiler (Dektak 3030), which measures the step height, and the RMS surface roughness was probed by Atomic Force Microscopy (Nanoscope IIIA, from Digital Instruments). Photoluminescence (PL) spectroscopy was also performed, at room temperature, on the etched surfaces to diagnose the surface damage resulting from etching. A blue laser (from LaserGlow, $\lambda = 462$ *nm*) was incident on the GaP surfaces etched under various conditions, and the resulting luminescence dispersed through an Oriel Cornerstone 130 (1/8 m) monochromator, and measured through photo-detectors.

B.2. Results and discussion

Several parameters pertinent to the GaP etching, such as BCl_3 flow rate, chamber pressure, and RF power were investigated in order to determine the optimal conditions.

The dependence of the etching rate on the BCl_3 flow rate is shown in Fig. B-1a. An increasing flow rate corresponds to a decreased residence time for the reactive etching radicals, with the chamber pressure being maintained constant ~10*mTorr*. While the initial peak (in the range of 0–10 *sccm*) corresponds to a reaction rate limited regime where the reactive radicals (such as $(BCl_n)^-$(n=1, 2, 3) and Cl^- interacting with the GaP sample surface) can fully react with Ga[80]; beyond 10 *sccm*, the etch rate is relatively constant at ~850 *nm/min*. In the higher flow rate regime, the dominant etch mechanism appears to be physical sputtering. The linear variation of the etch rate with the RF power (Fig. B-1b), and the chamber pressure (Fig. B-1c), also support the above conclusion.

(a)

(b)

(c)

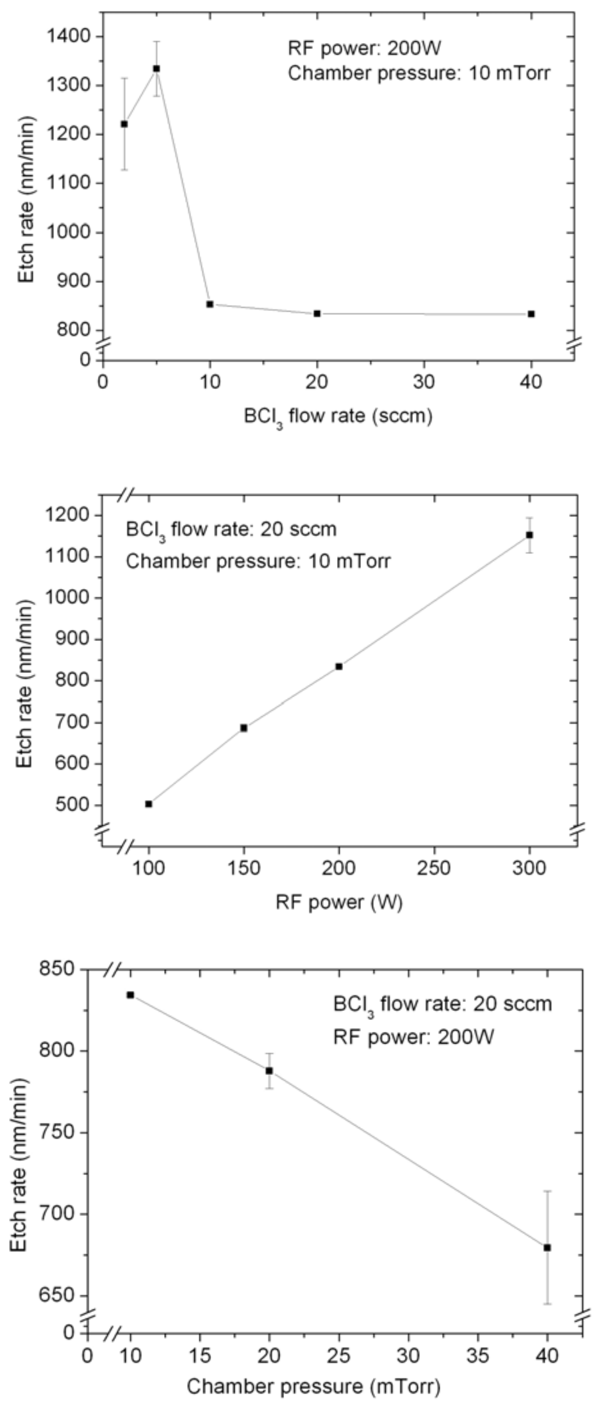

Figure B-1. A comparison of the etch rate of GaP as function of the (a) BCl_3 flow rate, (b) RF power, and (c) chamber pressure (six measurements on different samples were taken to determine the error).

It is remarkable that the etch rate could be increased to >1*μm/min*, at an RF power ~300*W*. However, such high powers result in considerable surface damage as was quantified through PL spectroscopy (Fig. B-4). On the other hand, increasing the chamber pressure reduces the mean free paths of the etching ions/radicals and lowers the physical sputtering, which decreases the etch rate. Similar flow rate dependencies were observed in the RIE of other compound semiconductors such as InGaN and GaN[80]. It is to be noted that, in comparison to a previous study[78] of GaP dry etching, using $SiCl_4$ based plasma processing, with an etch rate of ~75 *nm/min* (at 20 *mTorr*, 60 *W*), the etching rate in our work is approximately a factor of 5 higher (~500 *nm/min*, at 20 *mTorr*, 100 *W*).

To enhance the physical sputtering of GaP, Ar was added to the BCl_3 plasma but it was noticed that the etch rate was decreased (Fig. B-2a). This could be explained by positing that Ar has a dilution effect, causing a net reduction in the amount of reactive species reaching the surface. However, it was observed that the net roughness of the GaP surface increases with increased Ar flow rate, which might point to its physical influence (Fig. B-2b). Consequently, the use of Ar is not advocated for GaP etching where smooth surfaces are of paramount importance. Instead of argon, using carrier gases such as helium, neon, or even hydrogen could have less impact on surface smoothness[81].

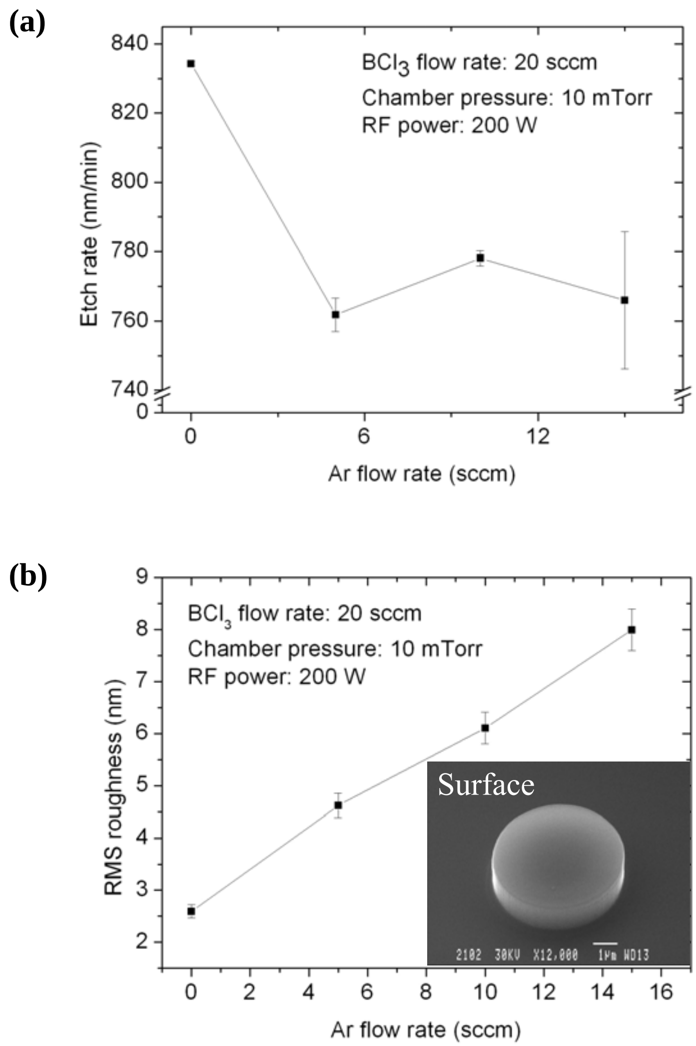

Figure B-2. The effects of Argon, as a carrier gas addition, on the GaP etch rate, as a function of the (a) flow rate, and (b) surface roughness (the insert show the circular etching profile of a GaP mesa, for the 10 *sccm* sample).

B.3. Etched surface characterization

Surface damage is a critical parameter for photonic device fabrication as it can cause light scattering and power loss. A detailed AFM characterization of the GaP surface etched under various conditions was performed. There is generally an increased roughness with various etching treatments (Fig. B-3b and c) compared to the un-etched sample (Fig. B-3a), with the most significant ffect arising from the use of Ar (Figs. B-2b and B-3c).

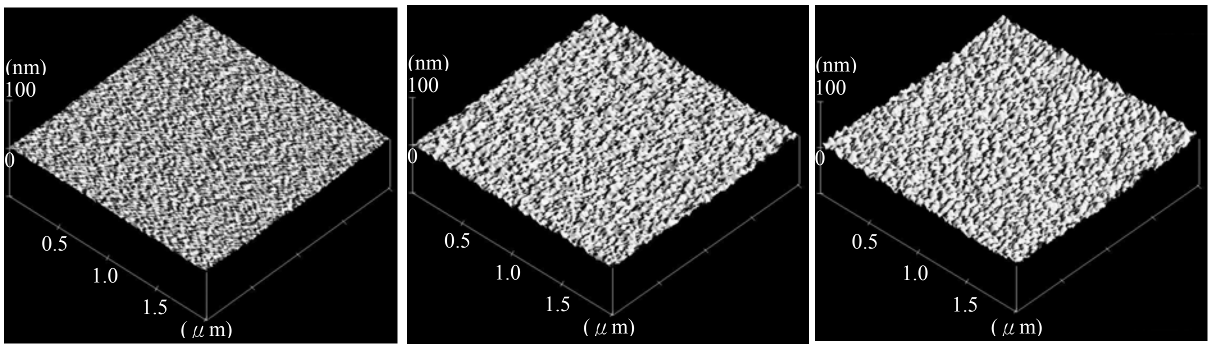

(a) **(b)** **(c)**

Figure B-3. Atomic force microscopy (AFM) images of the GaP surface topography. The Figures in the brackets indicate the RMS roughness: (a) Prior to etching (rms roughness: 1.3 *nm*), and GaP etched at 200*W*RF power, 20*mTorr* chamber pressure and (b) 20 *sccm* of BCl_3 (rms roughness: 2.4 *nm*), and (c) with additional 5 *sccm* of Ar gas (rms roughness: 4.5 *nm*).

We also think that subsequent wet etching chemical treatments, similar to those used for InP[82] and GaAs[83], of the surface might help to alleviate the surface roughness to <1 nm[84]. We specifically point to the use of α-hydroxy acids, that has been pioneered by one of the co-authors[82], for metal phosphide semiconductors, in conjunction with a $HCl:CH_3COOH:H_2O_2$ mixture[85] to be pertinent. Photoluminescence (PL) spectroscopy is often used as a sensitive, non-destructive, probe of the surface quality[86], and was used to study the concomitant effects of increased etch rate and RF power on radiative efficiency. It is to be noted, however, that in indirect bandgap semiconductors, such as GaP, non-radiative recombination tends to dominate the PL efficiency. The PL spectra of the bare and etched GaP under various RF powers are shown in Fig. B-4, where inverse relationship between the peak intensity and the RF power is observed. Additionally, while there is no peak shift from the unetched sample case (~2.23 *eV*), it is noted that the peak width decreases. Generally, a decrease in the PL intensity is correlated with poor interface properties and surface damage[87]. However, the rms surface roughness, as determined through AFM, was relatively constant (Fig. B-4 inset). The PL intensity decrease is then hypothesized to be either due to a change in the surface state density or changes in depletion thickness[84], brought about through increased RF power. In either case, the non-radiative surface recombination[88] is enhanced which leads to a quenching of the photoluminescence [89]. In the absence of a peak shift, our results seem to indicate a negative charging of the surface implying a reduced depletion width and narrower peak width. It is to be noted[67] that GaP has a surface energy level ~0.66±0.2 *eV*, which can be altered through surface treatment. If our proposed mechanism for the PL quenching is valid, then the effects of surface charging could be nullified by electrical means, and our study points to such possibilities. It would also be interesting to study the effect of surface adsorbates, in affecting charge transfer to/from the surface, to tune the PL intensity. For example, functional groups incorporating –OH and –OR, in conjunction with α-hydroxy acids can be used[82] to modify the surface potential by electron abstraction from the GaP surface. Further investigations involving Capacitance (*C*)–Voltage (*V*) measurements on the GaP are necessary to confirm these conclusions.

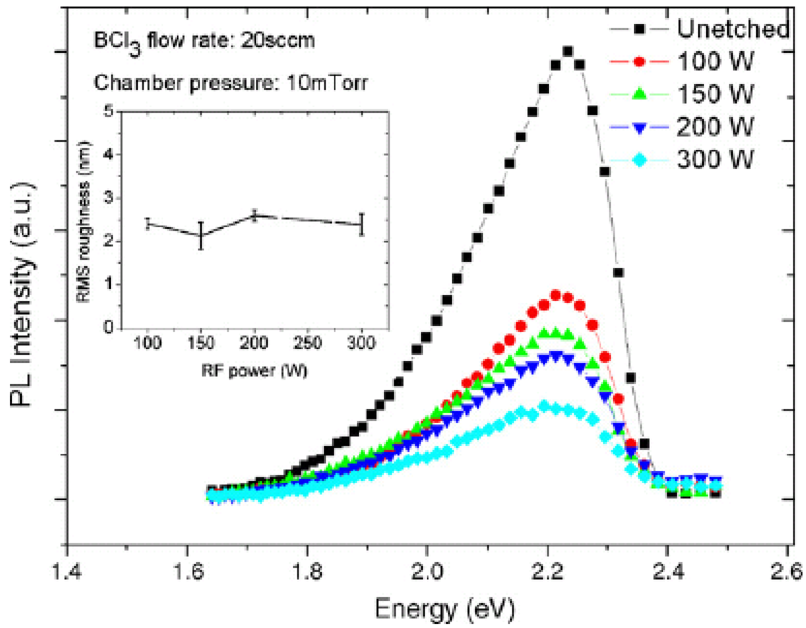

Figure B-4. A comparison of the photoluminescence (PL) spectra of GaP surface as a function of applied BCl_3 plasma RF power. The inset shows that the surface roughness is unchanged which points to charging of the GaP surface, and increased surface recombination as a source for the decreased PL intensity.

B.4. Summary

We have conducted a through investigation into the reactive ion etching (RIE) processes in GaP using BCl_3 based plasmas. The effects of flow rate, chamber pressure, and RF power on the etch rate has been studied. An increase in the RF power was shown to linearly increase the etch rate and physical sputtering of the surface (beyond a minimal BCl_3 flow rate). The use of Argon as a carrier gas leads to considerable surface roughening with a decreased etch rate and we consequently do not advocate the use of Ar, for BCl_3 plasma etching of GaP. AFM study has been used to correlate surface roughness with etching treatment. PL spectroscopy indicates that a change in the depletion region thickness, due to surface charging by negatively charged $(BCl_n)^-/Cl^-$ species is dominant and could account for the reduced PL intensities with etching.

This chapter, in full, has been published as “An experimental study of the reactive ion etching (RIE) of GaP using BCl_3 plasma processing” by S. H. Yang, P. R. Bandaru, Materials Science and Engineering B, Vol. 143, 27 (2007)

References

1. Semiconductor industry association, *International technology roadmap for semiconductors (ITRS)*. Interconnect chapter (semiconductor industry association, 2005). Available at http://www.itrs.net.

2. R. S. Tucker, P.-C. Ku and C. J. Chang-Hasnain, Slow-light optical buffers: capabilities and fundamental limitations. *Journal of Lightwave Technology*, 23, (12), 4046, **2005.**

3. R. Luijten, C. Minkenberg, R. Hemenway, M. Sauer and R. Grzybowski In *Viable opto-electronic HPC interconnect fabrics*, Proceeding of the ACM/IEEE SC05 supercomputer 2005 conference, 8-16, **2005**.

4. M. Notomi, K. Yamada, A. Shinya, J. Takahashi, C. Takahashi and I. Yokohama, Extremely large group velocity dispersion of line-defect waveguides in photonic crystals slabs. *Physical Review Letters*, 87, 253902, **2001.**

5. M. Notomi, A. Shinya, S. Mitsugi, E. Kuramochi and H. Ryu, Waveguides, resonators and their coupled elements in photonic crystal slabs. *Optics Express*, 12, 1551, **2004.**

6. T. Asano, K. Kiyota, D. Kumamoto, B. S. Song and S. Noda, Time-domain measurement of picosecond light-pulse propagation in a two-dimensional photonic crystal-slab waveguide. *Applied Physics Letters*, 84, 4690, **2004.**

7. Y. A. Vlasov, M. O'Boyle, H. F. Hamann and S. J. McNab, Active control of slowlight on a chip with photonic crystal waveguides. *Nature*, 438, 65, **2005.**

8. H. Gersen, T. J. Karle, R. J. P. Engelen, W. Bogaerts, J. P. Korterik, N. F. van Hulst, N. F., T. F. Krauss and L. Kuipers, Real-space observation of ultraslow light in photonic crystal waveguides. *Physical Review Letters*, 94, 073903, **2005.**

9. C. E. Finlayson, F. Cattaneo, N. M. B. Perney, J. J. Baumberg, M. C. Netti, M. E. Zoorob, M. D. B. Charlton and G. J. Parker, Slow light and chromatic temporal dispersion in photonic crystal waveguides using femtosecond time of flight. *Physical Review E*, 73, 016619, **2006.**

10. L. H. Frandsen, A. V. Lavrinenko, J. Fage-Pedersen and P. I. Borel, Photonic crystal waveguides with semislow light and tailored dispersion properties. *Optics Express*, 14, 9444, **2006.**

11. T. Baba and D. Mori, Slowlight engineering in photonic crystals. *Journal of Phyics D*, 40, 2659, **2007.**

12. M. D. Settle, R. J. P. Engelen, M. Salib, A. Michaeli, L. Kuipers and T. F. Krauss, Flatband slow light in photonic crystals featuring spatial pulse compression and terahertz bandwidth. *Optics Express*, 15, 219, **2007.**

13. F. Xia, L. Sekaric and Y. Vlasov, Ultracompact optical buffers on a silicon chip. *Nature Photonics*, 1, 65, **2007.**

14. D. Mori, S. Kubo, H. Sasaki and T. Baba, Experimental demonstration of wideband dispersion-compensated slow light by a chirped photonic crystal directional coupler. *Optics express*, 15, 5264, **2007.**

15. S. Kubo, D. Mori and T. Baba, Low-group-velocity and low-dispersion slow light in photonic crystal waveguides. *Optics Letters*, 32, 2981, **2007.**

16. D. A. B. Miller, Fundamental limit to linear one-dimensional slow light structures. *Physical Review Letters*, 99, 203903, **2007.**

17. T. Baba, Slow light in photonic crystals. *Nature Photonics*, 2, 465, **2008.**

18. Y. Okawachi, M. S. Bigelow, J. E. Sharping, Z. Zhu, A. Schweinsberg, D. J. Gauthier, R. W. Boyd and A. L. Gaeta, Tunable all-optical delays via brillouin slow light in an optical fiber. *Physical Review Letters*, 94, 153902, **2005.**

19. J. Sharping, Y. Okawachi and Gaeta., A., Wide bandwidth slow light using a Raman fiber amplifier. *Optics Express*, 13, (16), 6092, **2005.**

20. Y. Okawachi, J. E. Sharping, C. Xu and A. L. Gaeta, Large tunable optical delays via self-phase modulation and dispersion. *Optics Express*, 14, (25), 12022, **2006.**

21. S. Sarkar, Y. Guo and H. Wang, Tunable optical delay via carrier induced exciton dephasing in semiconductor quantum wells. *Optics express*, 14, (7), 2845, **2006.**

22. B. Pesala, Z. Chen, A. V. Uskov and C. Chang-Hasnain, Experimental demonstration of slow and superluminal light in semiconductor optical amplifiers. *Optics Express*, 14, (26), 12968, **2006.**

23. F. G. Sedgwick, B. Pesala, J.-Y. Lin, W. S. Ko, X. Zhao and C. J. Chang-Hasnain, Thz-bandwidth tunable slow light in semiconductor optical amplifiers. *Optics Express*, 15, (2), 747, **2007.**

24. A. V. Uskov and C. Chang-Hasnain, Slow and superluminal light in semiconductor for optical amplifiers. *Electronics Letters*, 41, (16), 55, **2005.**

25. X. Letartre, C. Seassal, C. Grillet, P. Rojo-Romeo and P. Viktorovitch, Group velocity and propagation losses measurement in a single-line photonic-crystal waveguide on InP membranes. *Applied Physics Letters*, 79, (15), 2312, **2001.**

26. M. Notomi, K. Yamada, A. Shinya, J. Takahashi, C. Takahashi and I, Y., Extremely lare group-velocity dispersion of line-defect waveguides in photonic crystal slabs. *Physical Review Letters*, 87, (25), 253902, **2001.**

27. T. Baba and D. Mori, Slow light engineering in photonics crystals. *Journal of Physics D*, 40, 2659, **2007.**

28. S. Fan, M. F. Yanik, M. L. Povinelli and S. Sandhu, Dynamic photonic crystals. *Optics and Photonics News*, 18, 41, **2004.**

29. A. Yariv, Universal relations for coupling of optical power between microresonators and dielectric waveguides. *Electronics Letters*, 36, (4), 321, **2000.**

30. R. M. Camacho, M. V. Pack and J. C. Howell, Wide-bandwidth, tunable, multiple-pulse-width optical delays using slow light in cesium vapor. *Physical Review Letters*, 98, 153601, **2007.**

31. R. M. Camacho, C. J. Broadbent, I. Ali-Khan and J. C. Howell, All-optical delay of images using slow light. *Physical Review Letters*, 98, 043902, **2007.**

32. E. Parra and J. R. Lowell, Toward application of slow light technology. *Optics and Photonics News*, 18, (11), 40, **2007.**

33. G. T. Reed, G. Z. Mashanovich, W. R. Headley, S. P. Chan, B. D. Timotijevic and F. Y. Gardes, Silicon photonics: are smaller devices always better? *Japanese Journal of Applied Physics*, 45, (8B), 6609, **2006.**

34. E. Dulkeith, F. Xia, L. Schares, W. M. J. Green and Vlasov, Y. A., Group index and group velocity dispersion in silicon-on-insulator photonic wires. *Optics Express*, 14, (9), 3853, **2006.**

35. Q. Xu, V. R. Almeida, R. Panepucci and M. Lipson, Experimental demonstration of guiding and confining light in nanometer-size low-refractive-index material. *Optics Letters*, 29, 1626, **2004.**

36. V. R. Almeida, Q. Xu, C. A. Barrios and M. Lipson, Guiding and confining light in void nanostructure. *Optics Letters*, 29, 1209, **2004.**

37. N. N. Feng, J. Michel and L. C. Kimerling, Optical field concentration in low-index waveguides. *Journal of Quantum Electronics*, 42, 885, **2006.**

38. H. G. Yoo, Y. Fu, D. Riley, J. H. Shin and P. M. Fauchet, Birefringence and optical power confinement in horizontal multi-slot waveguides made of Si and SiO_2. *Optics Express*, 16, (12), 8623, **2008.**

39. S. M. Rytov, Electromagnetic properties of a finely stratified medium. *Soviet Physical Jetp*, 2, (3), 466, **1956.**

40. C. Gu and P. Yeh, Form birefringence of layered media and volume gratings. *Journal of Optical Society America B*, 12, (6), 1094, **1995.**

41. C. Gu and P. Yeh, Form birefringence dispersion in periodic layered media. *Optics Letters*, 21, (7), 504, **1996.**

42. D. C. Flanders, Submicrometer periodicity gratings as artificial anisotropic dielectrics. *Applied Physics Letters*, 42, (6), 492, **1983.**

43. L. Pang, M. Nezhad, U. Levy, C.-H. Tsai and Y. Fainman, Form-birefringence structure fabrication in GaAs by use of SU-8 as a dry-etching mask. *Applied Optics*, 44, (12), 2377, **2005.**

44. A. Yariv, Coupled-mode theory for guided-wave optics. *Journal of Quantum Electronics*, QE-9, (9), 919, **1973.**

45. Ziel, J. P. v. d., Phase-matched harmonic generation in a laminar structure with wave propagation in the plane of the layers. *Applied Physics Letters*, 26, (2), 60, **1974.**

46. C. W. Haggans and L. Li, Effective-medium theory of zeroth-order lamellar gratings in conical mountings. *Journal of Optical Society America A*, 10, (10), 2217, **1993.**

47. I. Richter, P.-C. Sun, F. Xu and Y. Fainman, Design considerations of form birefringent microstructures. *Applied Optics*, 34, (14), 2421, **1995.**

48. D. L. Brundrett, E. N. Glytsis and T. K. Gaylord, Homogeneous layer models for high-spatial-frequency dielectric surface-relief gratings: conical diffraction and antireflection designs. *Applied Optics*, 33, (13), 2695, **1994.**

49. A. Fiore, V. Berger, E. Rosencher, P. Bravetti and Nagle, J., Phase matching using an isotropic nonlinear optical material. *Nature*, 391, 463, **1998.**

50. N. Kunzner, D. Kovalev, J. Diener, E. Gross, V. Y. Timoshenko, G. Polisski and Koch, F., Giant birefringence in anisotropically nanostructured silicon. *Optics Letters*, 26, (16), 1265, **2001.**

51. O. L. Muskens, M. T. Borgstrom, E. P. A. M. Bakkers and J. G. Rivas, Giant optical birefingnece in ensembles of semiconductor nanowires. *Applied Physics Letters*, 89, 233117, **2006.**

52. E. Kapon, J. Katz and A. Uariv, Supermode analysis of phase-locked arrays of semiconductor. *Optics Letters*, 10, (4), 125, **1984.**

53. P. Yeh, *Optical waves in layered media*. John Wiley & Sons: New Jersey, **2005**.

54. G. Lenz and J. Salzman, Eigenmodes of multiwaveguide structures. *Journal of Lightwave Technology*, 8, (12), **1990.**

55. T. Fujisawa and M. Koshiba, Polarization-independent optical directional coupler based on slot waveguides. *Optics Letters*, 31, 56, **2006.**

56. C.-Y. Chao, Simple and effective calculation of modal properties of bent slot

waveguides. *Journal of Optical Society America B*, 24, 2373, **2007.**

57. A. Sakai, G. Hara and T. Baba, Propagation characteristics of ultrahigh-Δ optical waveguide on silicon-on-insulator substrate. *The Japanese Society of Applied Physics*, 40, 383, **2001.**

58. E. A. Dobisz, S. L. Brandow, R. Bass and Mitterender, J., Effects of molecular properties on nanolithography in polymethyl methacrylate. *Journal of Vacuum Science Technology B*, 18, (1), 107, **2000.**

59. S. Yasin, D. G. Hasko and H. Ahmed, Fabrication of <5nm width lines in poly(methylmethacrylate) resist using a water:isopropyl alcohol developer and ultrasonically-assisted development. *Applied Physics Letters*, 78, (18), 2760, **2001.**

60. M. J. Madou, *Fundamentals of Microfabrication*. 2nd ed.; CRC Press: **2002**.

61. M. J. Rooks, E. Kratschmer, R. Viswanathan, J. Katine, R. E. Fontana and S. A. MacDonald, Low stress development of poly(methylmethacrylate) for high aspect ratio structures. *Journal of Vacuum Science Technology B*, 20, (6), 2937, **2002.**

62. D. G. Hasko, S. Yasin and A. Mumtaz, Influence of developer and development conditions on the behavior of high molecular weight electron beam resists. *Journal of Vacuum Science Technology B*, 18, (6), 3441, **2000.**

63. R. J. P. Engelen, Y. Sugimoto, Y. Watanabe, J. P. Korterik, N. Ikeda, N. F. van Hulst, K. Asakawa and L. Kuipers, The effect of higher-order dispersion on slow light propagation in photonic crystal waveguides. *Optics Express*, 14, 1658, **2006.**

64. R. Sun, P. Dong, N. N. Feng, C. Y. Hong, J. Michel, M. Lipson and L. Kimerling, Horizontal single and multiple slot waveguides: optical transmission at λ=1550nm. *Optics Express*, 15, 17967, **2007.**

65. A. H. Firester, M. E. Heller and P. Sheng, Knife-edge scanning measurements of subwavelength focused light beams. *Applied Optics*, 16, (7), 1971, **1977.**

66. J. W. Goodman, *Introduction to Fourier optics*. McGraw-Hill: New York, **1988**.

67. S. M. Sze, *Physics of Semiconductor Devices*. John Wiley: New York, 1981.

68. J. I. Pankove, *Optical processes in semiconductors*. Dover Publications, Inc: New York, **1971**.

69. M. Saritas and H. D. McKell, Absorption coefficient of Si in the wavelength region between 0.80-1.16 um. *Journal of Applied Physics*, 61, (10), 4923, **1987.**

70. G. G. Macfrlane, T. P. McLean, J. E. Quarrington and V. Roberts, Fine structure in the absorption-edge spectrum of Si. *Physical Review*, 111, (5), 1245, **1958.**

71. M. Balkanski, A. Aziza and E. Amzallag, Infrared absorption in heavily doped n-type Si. *Physica Status Solidi*, 31, 323, **1969.**

72. M. Gnan, S. Thoms, D. S. Macintyre, R. M. De La Rue and M. Sorel, Fabrication of low-loss photonics wires in silicon-on-insulator using hydrogen silsesquioxane electron-beam resist. *Electronics Letters*, 44, (2), 115, **2008.**

73. T. V. Blank, Y. A. Goldberg and Konstantinov, O. V., The ultraviolet radiation detectors based on wide-bandgap Schottky barrier structures. *Nuclear Instruments and Methods in Physics Research Section A*, (1-2), 60, **2002.**

74. P. Litovchenko, D. Bisello, A. Litovchenko, S. Kanevskyj, V. Opilat, M. Pinkovska, V. Tartachnyk, R. Rando, P. Giubilato and V. Khomenkov, Some features of current–voltage characteristics of irradiated GaP light diodes. *Nuclear Instruments and Methods in Physics Research Section A*, 552, (1-2), 93-97, **2005.**

75. F. Hatami, W. T. Masselink, V. Lordi and J. S. Harris, Green Emission from InP-GaP Quantum-Dot Light-Emitting Diodes. *Photonics Technology Letters*, 18, (7), 895-897, **2006.**

76. J. Tatebayashi, N. Nuntawong, Y. C. Xin, P. S. Wong, S. H. Huang, C. P. Hains, L. F. Lester and D. L. Huffaker, Ground-State Lasing of stacked InAs/GaAs quantum dots with GaP strain-compensation layers grown by metal organic chemical vapor deposition. *Applied Physics Letters*, 88, 221107-1 221107-3, **2006.**

77. G. M. Gajiev, V. G. Golubev, D. A. Kurdyukov, A. V. Medvedev, A. B. Pevtsov, A. V. Sel'kin and V. V. Travnikov, Bragg reflection spectroscopy of opal-like photonic crystals. *Physical Review B*, 72, 205115-1 205115-9, **2005.**

78. J. H. Epple, C. Sanchez, T. Chung, K. Y. Cheng and K. C. Hsieh, Dry etching of GaP with emphasis on selective etching over AlGaP. *Vacuum Science Technology B*, 20, (6), 2252-2255, **2002.**

79. S. W. Pang and K. K. Ko, Comparison between etching in Cl_2 and BCl_3 for compound demiconductors using a multipolar electron cyclotron resonance source. *Journal of Vacuum Science & Technology B*, 10, (6), 2703-2707, **1992.**

80. H. F. Hong, C. K. Chao, J. I. Chyi and Y. C. Tzeng, Reactive ion etching of GaN/InGaN using BCl_3 plasma. *Materials Chemistry and Physics*, 77, 411-415, **2002.**

81. M. Ohring, *Materials Science of Thin Films Deposition and Structure*. 2nd ed.; Academic Press: **2002**.

82. P. R. Bandaru and E. Yablonovitch, Semiconductor Surface-Molecule Interactions. *Journal of the Electrochemical Society*, 149, G599, **2002.**

83. E. Yablonovitch, C. J. Sandroff, R. Bhat and T. Gmitter, Nearly ideal electronic properties of sulfide coated GaAs surfaces. *Applied Physics Letters*, 51, 439, **1987.**

84. H. Morta and S. Adachi, Properties of GaP(001) surfaces chemically treated in NH_4OH solution. *Journal of Applied Physics*, 100, 054904, **2006.**

85. T. Berdinskikh, H. E. Ruda, X. Y. Mei and M. Buchanan, A kinetic study of structured surface relief patterning of GaP (1 1 1) *Journal of Electronic Materials*, 27, (3), 114-121, **1998.**

86. T.H. Gfroerer, *Photoluminescence in analysis of surfaces and interfaces*. John Wiley & Sons Ltd.: Chichester, 2000; p 9209.

87. D. Basak, T. Nakanishi and S. Sakai, Reactive ion etching of GaN using BCl_3, BCl_3/Ar and BCl_3/N_2 gas plasmas. *Solid-State Electronics*, 44, 725-728, **2000.**

88. R. S. Muller and T. I. Kamins, *Device Electronics for Integrated Circuits*. John Wiley: New York, **1986**.

89. R. R. Chang, R. Iyer, R. and D. L. Lile, Surface characterization of InP using photoluminescence. *Journal of Applied Physics*, 61, (5), 1995-2004, **1986.**